Thèse présentée pour obtenir le grade de

Docteur de l'Université de Strasbourg

Discipline: Chimie

par Yulia Sergeeva

Complexes ADN/polycation en solution et aux interfaces en tant que vecteurs de transfection non viraux de pointe

Date de soutenance prévue le 25 juin 2013

Membres du jury:

Directeur de Thèse: M. Gero Decher, Professeur, Strasbourg, France

Rapporteur Interne: M. Vincent Ball, Professeur, Strasbourg, France

Rapporteur Externe: Mme. Karine Anselme, Directeur de recherche, Mulhouse, France

Rapporteur Externe: M. Jean-François Berret, Professeur, Paris, France

Complexes ADN/polycation en solution et aux interfaces en tant que vecteurs de transfection non viraux de pointe

Résumé de Thèse en Français (Summary of the Thesis in French)

La thérapie génique offre de nouvelles possibilités pour le traitement des maladies humaines graves telles que les maladies cardio-vasculaires, neurologiques et cancéreuses, la cicatrisation, les troubles inhérents, etc.... Le concept de cette approche repose sur la délivrance systématique d'acides nucléiques dans les cellules des patients et l'expression consécutive de protéines thérapeutiques (ADN) ou de gène dormant (siARN).

En général, les méthodes de transfert de gènes peuvent être regroupés en deux catégories principales: les méthodes de transfert de gènes virales et non virales. Bien que de nos jours l'approche la plus efficace pour le transfert d'ADN dans les différentes lignées cellulaires est basée sur la délivrance de gènes viraux, son application dans la médecine clinique est limitée en raison des effets secondaires possibles comme la mutagenèse ou la réponse inflammatoire.

Alternativement une approche non virale implique la formation de complexes ADN/macromolécules (dénommés polyplexes) par des interactions électrostatiques entre les groupes phosphates chargés négativement de l'ADN et les groupes chargés positivement des macromolécules telles que des polymères, des lipides ou des dendrimères. Même si une recherche intensive a été menée, l'efficacité de transfection de ces polyplexes reste faible.

Parmi les agents synthétiques de transfection existants, le jetPEI™ (poly(éthylène imine) linéaire, 22 kDa) est l'un des transporteurs les plus efficaces à l'heure actuelle. Les propriétés uniques de ce polymère telles que la densité élevée de charges positives, la biocompatibilité et le soi-disant effet "éponge à protons", lui permettent de complexer l'ADN sous la forme de petites particules chargées positivement, de protéger l'ADN contre la dégradation dans

l'environnement cellulaire, de faciliter la libération endosomale et donc la réussie de la transcription. En dépit de leur efficacité supérieure, les vecteurs à base de PEI sont associés à une cytotoxicité élevée, en particulier pour les lignées cellulaires primaires.

Ce travail a été effectué dans le cadre d'un projet national à haut risque (Ship-In) dédié au développement de méthodes pour la reprogrammation de lignées cellulaires humaines afin d'induire des cellules pluripotentes. Les tâches de notre équipe ont été réalisées en collaboration avec le groupe du Professeur Stéphane Viville (IGBMC) et la société Polyplus Transfection™.

L'un des objectifs de ce travail a consisté à établir un protocole pour la transfection efficace d'une lignée cellulaire humaine primaire et à augmenter le rendement de transfection pour l'application d'un tel vecteur à base PEI pour un traitement médical.

L'efficacité de transfection des différents vecteurs non viraux a été testée sur la lignée cellulaire CPRE2 (fibroblastes dermiques humains primaires adultes).

Bien qu'au cours de ce travail des études approfondies ont été menées pour développer des vecteurs de pointe pour une transfection à long terme via une surface en testant divers films multicouches contenant de l'ADN et des agents de transfection comme le jetPEI™, le dendrimère poly(amido amine) (6$^{\text{ème}}$ génération), le chitosane, le collagène et le Chlorure de poly(méthacryloxyéthyltriméthyl ammonium), l'efficacité de transfection de ces systèmes s'est montrée très faible. Par conséquent, il a été décidé de focaliser nos efforts sur le développement d'un protocole robuste et reproductible pour la transfection efficace de la lignée cellulaire CPRE2 en solution.

A cet effet, les polyplexes à base de jetPEI™ ont été formés dans une solution à 0,15 M en NaCl avec de l'ADN plasmidique codant pour la protéine fluorescente verte (GFP). Les expériences ont été réalisées à une concentration constante de solution de jetPEI™ et la concentration de l'ADN a été variée en fonction du rapport azote sur phosphate N/P. Comme contrôle positif, la transfection du jetPEI™ dans des conditions standard a été

appliquée. L'efficacité de transfection est exprimée comme le pourcentage de cellules fluorescentes sur la population totale de cellules 48h après addition des polyplexes à la culture cellulaire.

Chose étonnante, les meilleurs résultats ont été obtenus pour la transfection avec des polyplexes préparés à N/P = 7,5. Une diminution de la concentration d'ADN conduit à des niveaux plus faibles de transfection alors que la viabilité des cellules augmente lentement.

Le traitement des cellules avec des polyplexes à N/P = 5 a conduit à une diminution de la viabilité des cellules par rapport à des cellules non traitées. La diminution de la dose d'ADN n'a pas eu d'effet dramatique sur la viabilité cellulaire. Dans les conditions d'efficacité de transfection maximale, la viabilité cellulaire était de 80%. La viabilité des cellules après la transfection avec des polyplexes formés à N/P de 10, 15 et 30 était respectivement de 82%, 84% et 78%.

Pour identifier les paramètres influençant les taux de transfection, la taille des polyplexes a été analysée par diffusion dynamique de la lumière (DLS). Les données ont été obtenues avec des échantillons fraîchement préparés dans du NaCl 0,15 M à 25 °C. Les résultats ont montré que la diminution de la concentration d'ADN conduit à la formation de particules plus petites. Les caractéristiques des complexes déterminées par DLS sont présentées dans le tableau 1.

Rapport N/P	v(DNA), nmol	Diamètre estimé, nm (distribution en nombre)	Potentiel zeta (ζ) mV
5	3	777±15	34±4
7.5	2	575±61	36±4
10	1.5	472±63	31±2
30	0.5	220±12	27±6

Tableau 1. Taille et potentiel zêta (ζ) des complexes à base de PEI préparés à différents rapports N/P et à 0,15 M NaCl (moyenne ± SD).

Les micrographes de microscopie électronique à transmission ont révélé que les polyplexes présentent une structure sphérique et homogène. La taille des particules semble être beaucoup plus faible que celle mesurée par DLS. Ceci peut être dû à des différences dans le protocole qui sont discutées dans le texte principal. Le diamètre des polyplexes à N/P = 5 est compris entre 200 à 300 nm tandis que les polyplexes formés à N/P = 7,5 et 10 varie de 100 à 200 nm.
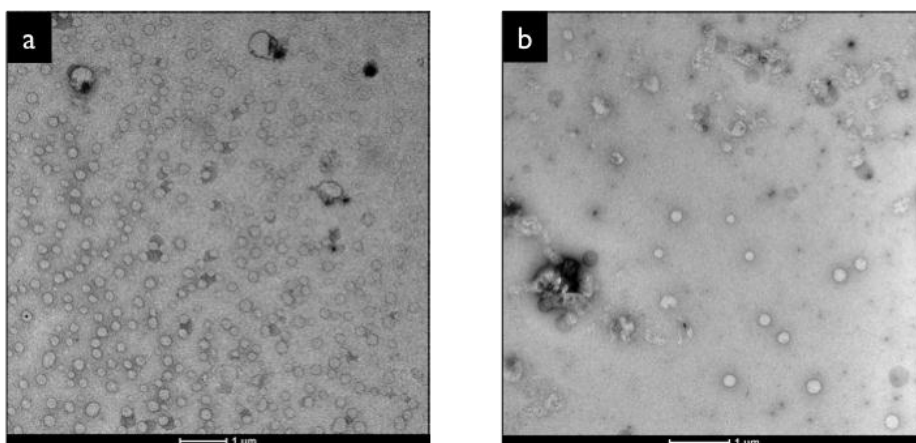

Figure 1. *Micrographes TEM des polyplexes formés avec un rapport N/P de 5 (a) et de 7,5 (b).*

Interaction des cellules primaires avec substrats fonctionnalisés par LbL

Comme la transfection via une surface nécessite la culture de cellules sur des films LbL contenant un agent de transfection et de l'ADN, l'étude du comportement des cellules sur des films LbL est donc d'une importance primordiale.

L'assemblage couche-par-couche est une approche facile et robuste pour la construction à façon de films multifonctionnels sur presque n'importe quelle surface avec un contrôle à l'échelle nanométrique de la composition du film. De plus, les propriétés des films telles que l'épaisseur, la charge de surface, la topologie et la mouillabilité peuvent être modifiées et optimisées en fonction des défis spécifiques. Du fait de sa simplicité et du nombre important des molécules

pouvant être incorporées dans un film, l'assemblage LbL est largement utilisé pour des applications en science des matérieux et dans les sciences de la vie, et en particuliers dans la conception de surfaces destinées à l'adhésion et la croissance cellulaire. Il est connu que le comportement, les fonctions et la viabilité des cellules sont définis par les interactions cellules-matériau qui peuvent être contrôlés par la chimie de surface, la topologie de surface et les propriétés physiques du matériau. La méthode couche-par-couche est l'exemple rare où ces trois paramètres peuvent être contrôlés indépendamment.

Dans cette étude, nous nous sommes focalisés sur l'influence de la composition chimique des films en investiguant les propriétés physiques telles que la stabilité et la mouillabilité des films multicouches sur la survie et la prolifération des cellules. Les polyélectrolytes suivants ont été utilisés pour l'assemblage LbL: la poly(éthylène imine) (PEI) ramifiée, l'hydrochlorure de poly(allylamine) (PAH), le chlorure de poly(diallyldiméthylammonium) (PDDA), le chitosane (Chit), le sulfate de dextran (DexS), l'alginate de sodium (Alg), l'hexamétaphosphate de sodium (PSP) et le poly(styrènesulfonate) de sodium (PSS). L'assemblage des multicouches a été suivi par ellipsométrie et microbalance à cristal de quartz avec mesure de dissipation (QCM-D).

Les films multicouches étudiés ont été assemblés par des interactions électrostatiques entre des polyélectrolytes de charges opposées. Toutefois, il est connu que les polycations libres peuvent induire des effets cytotoxiques via des interactions avec la membrane cellulaire ou des protéines de la matrice extracellulaire. Par conséquent, il est essentiel d'étudier la stabilité des systèmes LbL préparés dans le milieu de culture cellulaire dans les conditions physiologiques. Dans ce travail, la stabilité des films LbL a été analysée par QCM-D puisque cette technique permet de suivre simultanément *in situ* et en temps réel les changements structurels et de la masse á la surface du cristal. Les résultats obtenus ont révélé que le milieu de croissance cellulaire interagit étroitement avec les multicouches induisant l'adsorption rapide des composants du milieu ou change les propriétés physiques des multicouches. L'incubation

des couches pendant 96h n'a pas conduit à des changements dramatiques dans les courbes de fréquence et de dissipation suggérant que les films LbL étudiés garde leur composition dans des conditions physiologiques.

Pour l'analyse de l'effet des films LbL sur la survie/prolifération des cellules, des cellules CPRE2 ont été ensemencées sur des multicouches dans un milieu de croissance cellulaire. La population cellulaire a été comptée toutes les 24h et le quatrième jour, la viabilité des cellules a été analysée par cytométrie en flux.

Nos résultats ont montré que les cellules prolifèrent sur les couches contenant du PAH pendant 5 jours. Les meilleurs résultats ont été obtenus avec le film PEI(PSS/PAH)$_5$ où la population cellulaire était proche de celle obtenue pour des cellules ensemencées sur une couche de gélatine. Cependant, les films PEI(DexS/PAH)$_5$ et PEI(Alg/PAH)$_5$ ont donné un nombre de cellules plus faible que sur du verre non modifié. La viabilité cellulaire après 4 jours était de 87%, 80% et 70% pour PEI(PSS/PAH)$_5$, PEI(DexS/PAH)$_5$ and PEI(Alg/PAH)$_5$ respectivement.

L'exposition des cellules aux multicouches contenant du PDDA a conduit à une faible adhésion cellulaire induit par un changement de la morphologie des cellules. Comme le montre la Figure 2, les cellules ne se propagent pas et montre une morphologie ronde. En outre, il a été constaté que les multicouches avec du chitosane entravent la croissance des cellules.
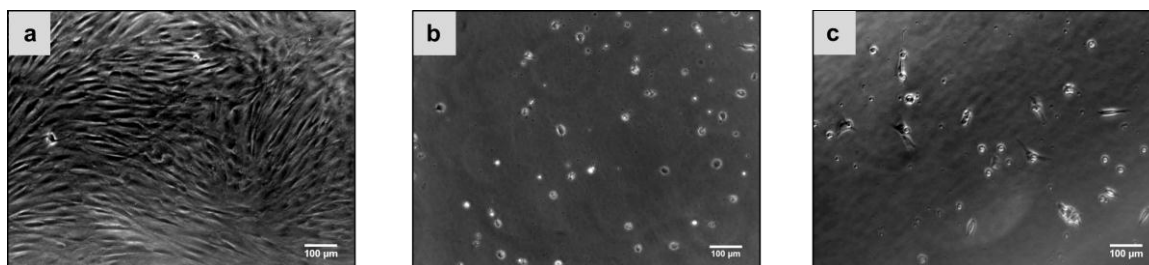

Figure 2. *Micrographes de cellules CPRE2 ensemencées sur different revêtements LbL 96h après ensemencement des cellules: a) PEI(PSS/PAH)$_5$ b) PEI(PSS/PDDA)$_5$ c) PEI(PSS/CH)$_5$.*

Après 24h, les cellules sont collectées et réensemencées sur une plaque recouverte de gélatine. Les données obtenues ont révélé que les cellules recueillies après l'incubation avec du PEI(Alg/CH)$_5$, PEI(Alg/PDDA)$_5$, PEI(PSS/CH)$_5$ et PEI(DexS/CH)$_5$ ont été en mesure de se fixer et de proliférer. En revanche, les cellules collectées après l'incubation avec du PEI(PSS/PDDA)$_5$ n'étaient pas en mesure d'adhérer à la surface de la gélatine après réensemencement.

Pour mettre en évidence les raisons d'un tel comportement cellulaire préférentiel, les films multicouches ont été caractérisés par microscopie à force atomique et angle de contact avec de l'eau. Il a été constaté que les propriétés topologiques et de mouillage du revêtement ont radicalement changé après le contact avec le milieu de croissance cellulaire. Cependant, nos résultats mettent en évidence la faible influence de la topographie des multicouches étudiés sur le comportement cellulaire.

Systèmes LbL	Angle de contact (degré)	Angle de contact après incubation avec le milieu de croissance cellulaire, (degré)
PEI(PSS/PAH)$_5$	42±2	47±1
PEI(PSS/PDDA)$_5$	31±1	45±1
PEI(DexS/PAH)$_5$	30±2	61±1
PEI(PSS/CH)$_5$	29±1	52±1
PEI(Alg/PAH)$_5$	27±1	61±2
PEI(Alg/PDDA)$_5$	16±2	56±5
PEI(Alg/CH)$_5$	9±1	28±5
PEI(DexS/PDDA)$_5$	8±1	18±5
PEI(DexS/CH)$_5$	6±1	69±5

Tableau 2. *Angles de contact des films LbL natifs et après incubation avec un milieu de culture cellulaire pendant 1h à 37 °C.*

En outre, nos résultats ont montré que, pour certains systèmes, le comportement des cellules sur des films LbL pourrait être contrôlée non seulement par les propriétés de la couche la plus externe mais aussi par les propriétés de couche localisée dans le film (Figure 4). Cet effet a eu tendance à augmenter dans les expériences effectuées avec un milieu sans sérum.
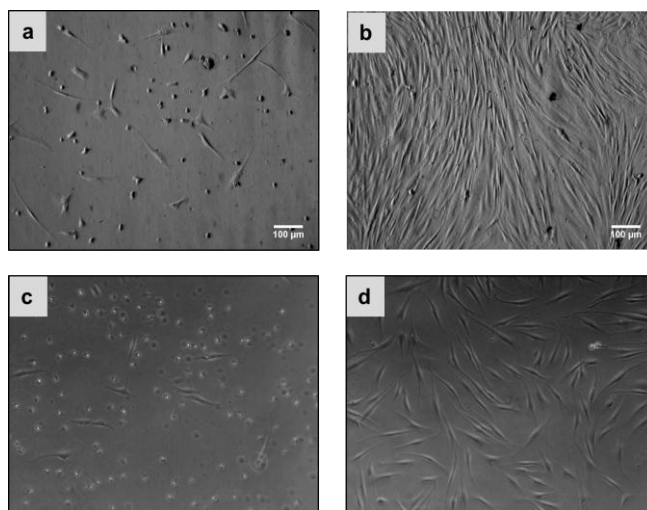

Figure 3. *Micrographes de cellules CPRE2 ensemencées sur des films LbL PEI(PSP/PAH)$_5$ (a et c) and PEI(PSP/PAH)$_5$/PSP (b et d) dans un milieu contenant du sérum (a et b) et dans milieu sans sérum (c et d).*

Le développement de méthodes pour suivre la transfection *in-situ* et pour détecter l'apparition de la cytotoxicité pourrait conduire à de nouvelles perspectives dans le domaine du transfert de gènes, qui est aujourd'hui principalement explorés par une approche par "essai-erreur". Nous avons pour la première fois commencé à utiliser des microbalances à cristal de quartz avec mesure de dissipation (QCM-D) pour le suivi in situ de la transfection via des mouvements du cytosquelette (collaboration avec le groupe du Prof Sofia Svedhem, Chalmers University of Technology, Suède).

Acknowledgments

I would like to thank Professor Gero Decher for giving me an opportunity to work in his group and being supportive and attentive to me. Especially I appreciate that he gave me the opportunity and the freedom to do some discretionary work.

I would like to express my deepest gratitude to for Dr. Karine Anselme, Professor Jean-François Berret and Professor Vincent Ball for having accepted to act as referees for my thesis work.

I would like to express my gratitude to Professor Stéphane Viville, Dr. Philippe Tropel, Dr. Neuberg, Dr. Weill, Dr. Erbacher and Laura Jung for an excellent and fruitful collaboration over the course of the "Ship-In" project.

I would like to sincerely thank Professor Bengt Kasemo, Professor Sofia Svedhem and Dr. Angelika Kunze for working together with me, for their guidance, help and support within our fruitful collaboration.

I am extremely grateful to Dr. Olivier Felix for enormous help and support during my research and preparation of this manuscript.

I would like to thank all my inspiring and talented colleagues, friends, fellows and relatives. There are many people who, in many ways, contributed to this work. I appreciate their help, and their contribution is a very important part of this thesis.

Most important, I would like to thank my family: my parents and husband for all their patience and understanding, for support and motivation. I could not have done it without you.

Table of Content

List of abbreviations

AFM	Atomic force microscopy
Alg	Alginic acid sodium salt
BSA	Bovine serum albumin
CH	Chitosan
DexS	Dextran sulfate
DLS	Dynamic light scattering
dsDNA	Double stranded DNA
pDNA	Plasmid DNA
EDL	Electrical double layer
ECM	Extracellular matrix
FACS	Fluorescence-activated cell sorting
FBS	Fetal bovine serum
FTIR	Fourier transform infrared spectroscopy
GAG	Glycosaminoglycan
GFP	Green fluorescent protein
HA	Hyaluronic acid
HEP	Heparin
hIPS	Human induced pluripotent stem cells
HSA	Human serum albumin
IgG	Immunoglobulin G
LbL	Layer-by-Layer
OWLS	Optical waveguide lightmode spectroscopy
PAA	Poly(acrylic acid)
PAH	Poly(allylamine hydrochloride)
PEC	Polyelectrolyte complex
PEG	Poly(ethylene glycol)
PEI	Poly(ethylenimine)
lPEI	Linear poly(ethylenimine)
PDDA	Poly(diallyldimethylammonium chloride)

PGA	Poly(glutamic acid)
PLGA	Poly(L-glutamic acid)
PLL	Poly(L-lysine)
PMAA	Poly(methacrylic acid)
PSS	Poly(sodium 4-styrenesulfonate)
PSP	Sodium hexamethaphosphate
QCM-D	Quartz crystal microbalance with enhanced dissipation
RGD	Arginine-glycine-aspartate sequence motif within fibronectin
RMS roughness	Root mean square roughness
siRNA	Short interfering RNA
SAMS	Self-assembled monolayers
TEM	Transmission electron microscopy

1. Introduction

1.1. Polyelectrolyte complexes (PEC)

The interactions between polyelectrolytes of opposite charges in aqueous medium lead to the formation of interpolyelectrolyte complexes. The process of complex formation is governed by the characteristics of individual polyelectrolyte components (properties of ionic sites, position of ionic sites, charge density, rigidity of macromolecular chains…) and the chemical environment (solvent, ionic strength, pH and temperature) (*1-6*). Polyelectrolyte complexes form in the bulk solution and at interface. The latter phenomenon leads to formation of polyelectrolyte thin films called "polyelectrolyte multilayers" and is discussed in the section 1.2.

1.1.1. Thermodynamics of complex formation

Macro-ions in aqueous solutions are surrounded by a electrical double layer (EDL) consisting of the small counter ions and co-ions. Since the average distance between the positive and negative ions is smaller than that between ions of the same charge, the ions involved in EDL are characterized by lower energy and limited translational freedom (lower entropy).

The interactions of two oppositely charged polyelectrolytes lead to the destruction of EDL of the macromolecules, and to the subsequent release of counter ions in the solution (Figure 1). The release of small counterions associated with the increase in entropy controls the shift of thermodynamical equilibrium towards the formation of the complexes. Although the decrease in the configurational and the translational entropy of complexed polyelectrolyte chains opposes complex formation, its contribution is small compared to the entropy of the counter ions release and thus the complexation is usually considered to be driven entropically (*1, 6, 7*).
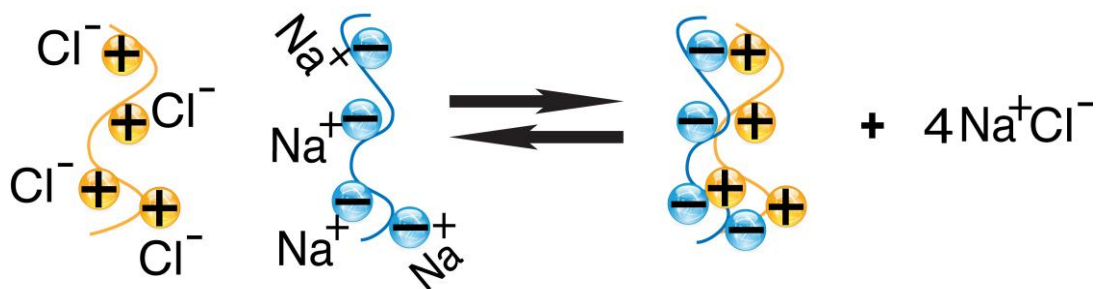
Figure 1. *Formation of polyelectrolyte complex (PEC) as a result of interactions of two oppositely charged polyelectrolytes (1).*

The dissociation of the complexes can be influenced by the ionic strength. Increase of the ionic strength leads to the screening of the electrostatic interaction between polyelectrolytes and therefore decreases the number of interpolyelectrolyte bonds within the PEC. However, at certain salt concentration the screening of electrostatic interaction may improve the complex stability. High salt concentration leads to the increase in complex dimensions and to reorganization of the complex (*6-8*).

1.1.2. Characteristics of polyelectrolyte complex formation

Since the composition and the properties of polyelectrolyte complexes depend on the degree of polyelectrolyte dissociation, they can be divided into four subclasses: the complexes containing a) strong polyacid - strong polybase, b) strong polyacid – weak polybase, c) weak polyacid – strong polybase and d) weak polyacid – weak polybase.

The properties of strong polyacid - strong polybase polyelectrolyte complexes were studied by Michaels *et al.* (*9*). It was demonstrated that mixing of poly(sodium 4-styrenesulfonate) (PSS) with poly(4-vinylbenzyl-

trimethylammonium chloride) results in the formation of equimolar complexes. The complex composition was independent of the solution pH and polyelectrolyte concentrations.

The composition of the complexes and the complex formation process depends on the position of charged groups in the polyelectrolyte chain (Figure 2).
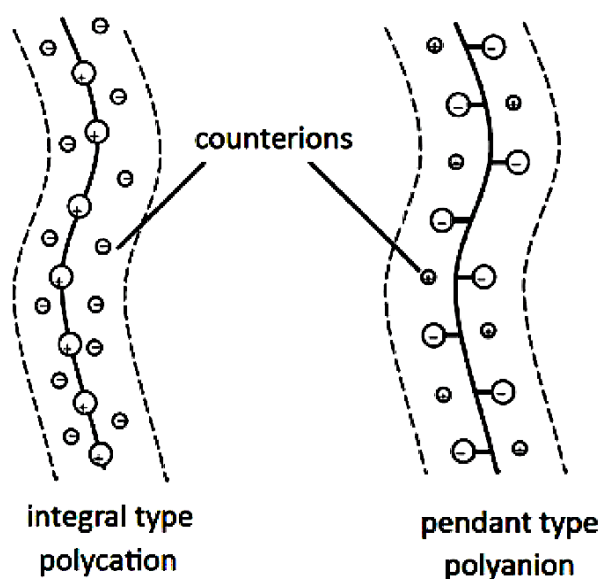
Figure 2. *The integral and pendant types of polyelectrolytes.*

The complex formation and the properties of the complexes made of PSS and the series of integral or pendant types of polycations were studied by Tsuchida and co-workers (*10*). It was demonstrated that the use of pendant type of polycation leads to the formation of equimolar complexes independently of the order of mixing.

The addition of polyanion to a solution of polycation of integral type at the mixing ratio φ = 1 yielded the formation of equimolar complexes. However, further increase in the polyanion concentration led to the redissolution of the

complex at φ equal to 1/3. Moreover, the complexes solubility depends on the order of mixing. The addition of polycation to the polyanion resulted in the formation of water soluble complex at ratio 1/3, whereas equimolar water insoluble complexes were obtained at mixing ratio 1. Authors concluded that using pendant type of polycation after the formation of equimolar complex in excess of polyanion the cationic sides in the complexes are not accessible for further interactions with polyanion. In the integral type of polycation with cationic groups being slightly hindered, the polyanion chains are able to interact with the cationic groups of polycation to form soluble complexes.

The composition of complexes formed by weak polyelectrolytes is governed by their dissociation state (α) (*2, 6*). The conversion in the complex reaction (θ) defined as a ratio between actual number of interpolyeletrolyte salt bonds and their maximum number may be conveniently controlled by altering pH. The shift in free energy of complex formation (ΔG$_{cs}$) due to the pH changes of the reaction mixture is given as (*2*):
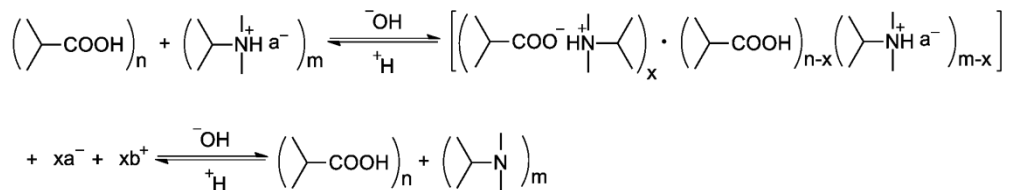
$$\Delta pH(\theta, \alpha) = \frac{\Delta G(\alpha) - \Delta G(\theta)}{2.3RT} = \frac{\Delta G_{cs}(\theta, \alpha)}{2.3RT}$$

Tsuchida et al. suggested that the degree of dissociation of weak polyelectrolyte is affected by the presence of oppositely charged polyelectrolyte (*8*). It was demonstrated that the *pK$_a$* of the poly(methacrylic acid) (PMAA) decreases in the presence of various polycations. Polycarboxylic acid in the complex undergoes reversible structural changes with respect to the solution pH. In the lower pH region it may take randomly coiled conformations and exhibit a looped shape due to the chains flexibility and weak electrostatic repulsions. At higher pH values the strong electrostatic repulsions between

ionized carboxylic groups favor the increase in the rigidity of the chain backbones and the extended conformation of the polycarboxylic acid chains (Figure 3).
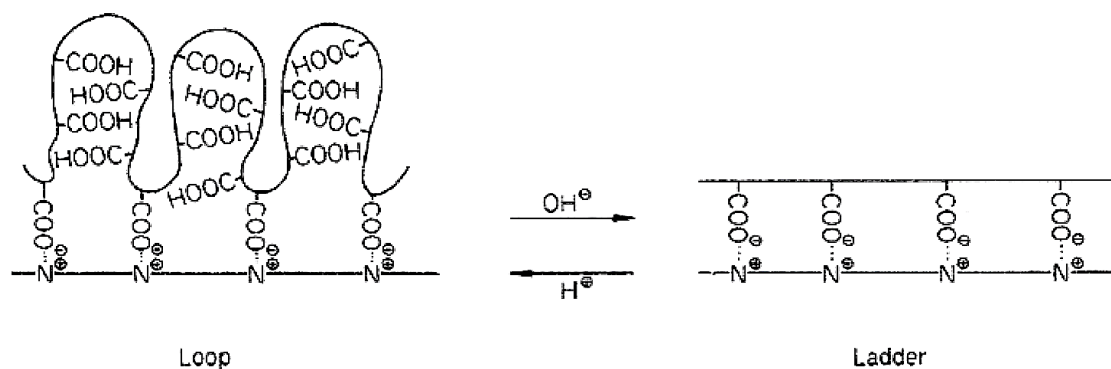
Figure 3. *Reversible structural changes of PMAA with respect to the solution pH (8).*

Nakajima et al. reported that the rigidity of polyelectrolyte chains affects the complex composition (*11*). The studies on the complexes made of the polysaccharide chains revealed that the complexes prepared with more rigid polymer chains deviated from expected stoichiometry.

The formation of the complexes may favor the conformational changes of the macromolecular chains. The conformational transitions of poly(*L*-lysine) (PLL) in the complex with respect to the configuration (tacticity) of PMMA molecules were studied (*12*). It was described that iso-PMAA increases the number of the α-helical PLL chains in the complexes, whereas PMAA with lower stereo-regularity favor the helix-destructing effects.

A new approach to control the flocculation process and therefore the parameters of forming complexes was demonstrated by Schneider and Decher in 2008 (*13*). The reported flocculation system was based on three components: trisodium citrate, poly(allylamine) and negatively charged citrate-stabilized gold nanoparticles.

Hybrid nanoparticle-filled aggregates or nanobags were formed after the injection of poly(allylamine) solution in the mixture of gold nanoparticles and trisodium citrate. It was established that nanobags parameters such as size, morphology and loading capacity can be easily controlled by tuning stoichiometric balance between the total number of positive and negative charges and the concentration of poly(allylamine) or citrate (Figure 4).
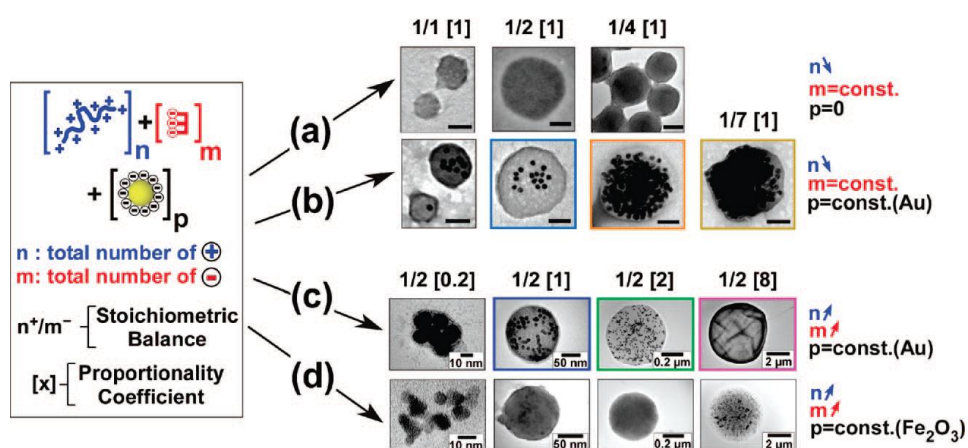
Figure 4. *Transmission electron micrographs of individual flocs formed through the flocculation of a three component system: poly(allylamine hydrochloride) , blue, a total of n positive charges; e.g., n+), trisodium citrate (red, a total of m negative charges; e.g., m-) and either gold (Au) or iron oxide (Fe$_2$O$_3$) citrate-stabilized nanoparticles (p) const; 1.2 nM in nanoparticles).*

1.2. Layer-by-Layer assembly

Since its introduction in 1991, the Layer-by-Layer (LbL) deposition technique became a versatile method for the construction of nanostructured coatings, in general, for surface functionalization and engineering of multifunctional films (*14, 15*).

Layer-by-Layer buildup is based on intermolecular interactions, e.g. electrostatic interactions, hydrogen bonding, charge transfer, covalent bonding, hydrophobic interactions…, and subsequent formation of complexes between the macromolecules on the surface of the substrate (*15*).

Generally, LbL films are prepared under mild conditions and are assembled with no restriction to the size, shape or material used as a template (*14, 15*).

Due to its versatility, LbL assembly is attractive for engineering of the advanced biomaterials. Nanoparticles, clay platelets, enzymes, polypeptides, nucleic acids, proteins, polysaccharides, viruses, living cells can be incorporated into the film towards such purpose (Figure 5).
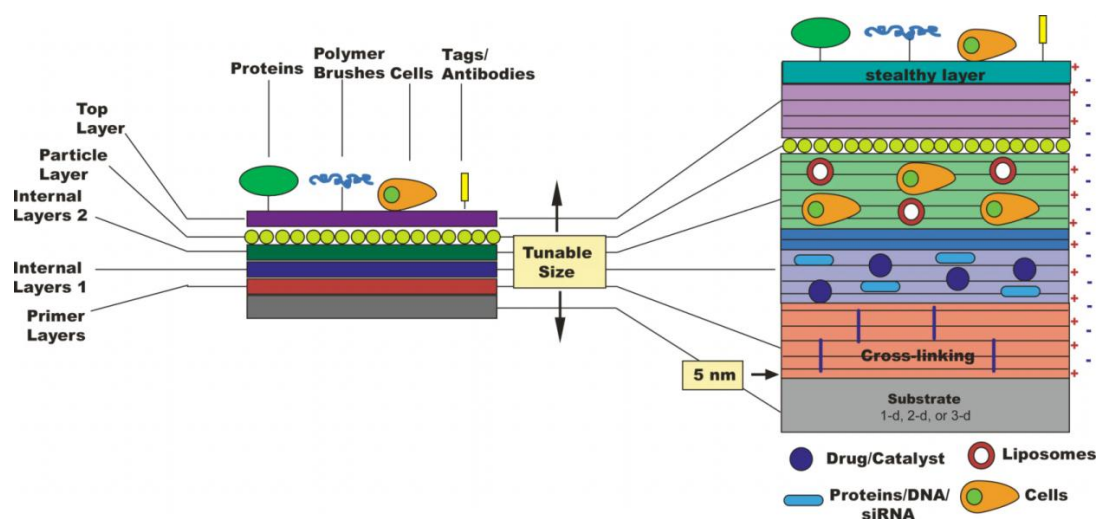
Figure 5. *Illustration of multifunctionality of LbL films (17).*

LbL assembly is an ideal tool to control the sustain release of bioactive molecules or drugs by varying their location in the film. Moreover, the concentrations of the film components can be controlled by the number of the corresponding layers. The LbL coatings are used for the creation of artificial photosynthesis membranes, bioreactors, biosensors, superhydrophobic surfaces and superstrong materals as well as for the improvement of biocompatibility of medical implants and for the design of the materials intended to control cellular adhesion and proliferation (*15-18*).

1.2.1. Layer-by-Layer formation

One of the important features of LbL assembly is its simplicity (*14, 19*).

As shown in Figure 6, the buildup of multilayers starts by bringing the substrate carrying a net charge in the contact with solutions of oppositely charged polyelectrolytes. The deposition of the polyelectrolyte layer normally leads to the overcompensation of the original surface charge (*20*). The alternation of the charge after each layer deposition allows to adsorb a polyelectrolyte of opposite charge and therefore to continue the film build up process (Figure 7).

After the substrate is rinsed to remove un-adsorbed or weakly adsorbed polymer chains, a polyelectrolyte carrying an opposite charge to the first layer is deposited. The rinsing of the substrate completes the formation of the first layer pair. Subsequently, additional layers can be deposited in the same manner yielding a multilayer film of desirable thickness and properties.
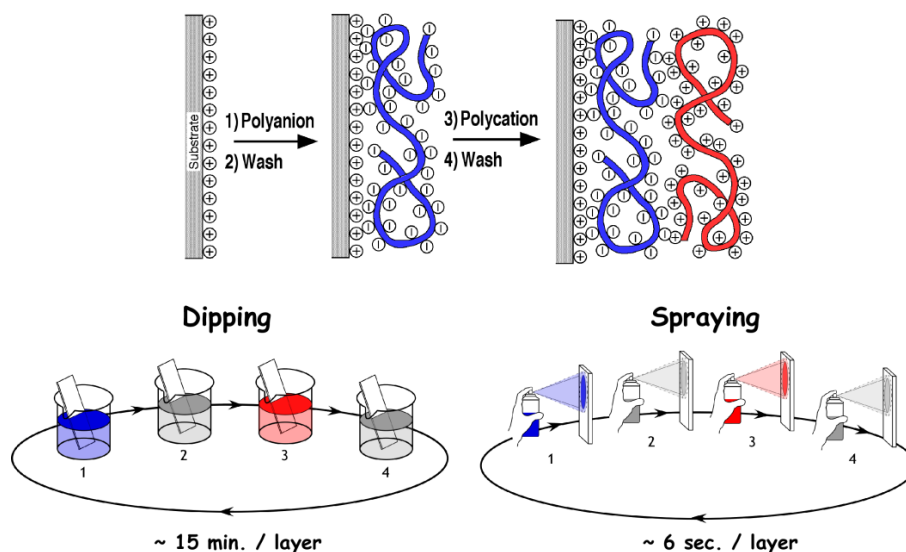
Figure 6. *A simplified schematics of LbL deposition process (14).*

LbL films can be assembled via dipping, spray-assisted assembly and spin-assisted assembly (*15*). The two latter methods have the advantage to reduce the deposition time of the layers and the volume of the solutions used for LbL build-up on large substrates. The time for the deposition of a single layer is about 15 min for dipping and about 10 sec for spray-assisted assembly.
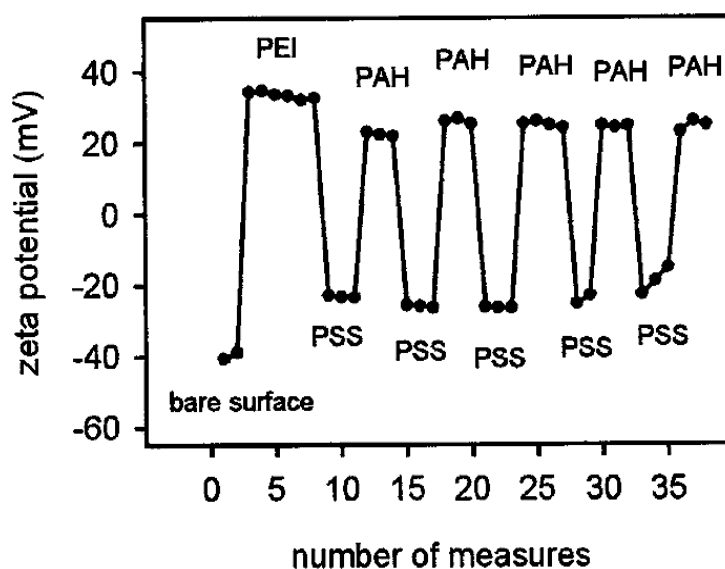
Figure 7. *Evolution of the ζ-potential during the buildup of a PEI(PSS/PAH)$_5$ multilayer film (20).*

The comparison of the layers deposited via dipping and spray-assisted assembly revealed that the sprayed films are thinner and smoother than the dipped ones (*21*). Therefore, changing the method of LbL assembly is another tool for tuning the properties of multilayer films.

1.2.2. The structure of polyelectrolyte multilayer films

Often, the inner structure of LbL films represent a framework subdivided onto three zones (*20*) (Figure 8).

Zone I (precursor zone) consists of one or a few polyelectrolyte layers close to the substrate. The properties of these layers are defined by the characteristics of substrate surface e.g. charge density, substrate roughness, contact angle etc.
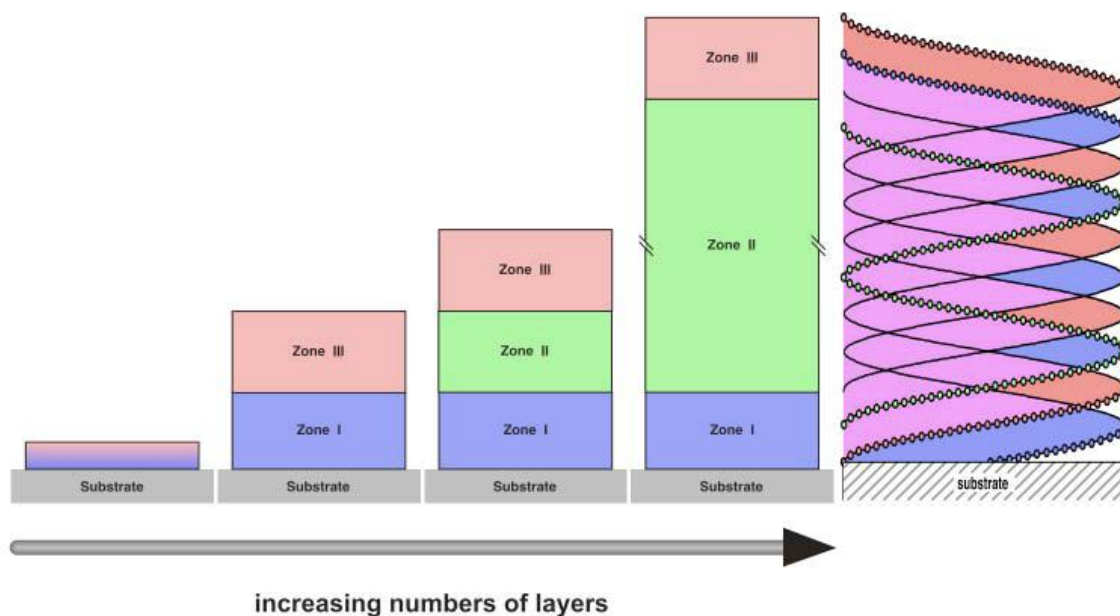
Figure 8. *Schematic of the multilayer inner structure by the model of the three zones (20).*

The zone III (outer zone) is formed by one or few layers close to the surface of the film. The properties of this zone are defined by the properties of solutions or

the air. The external part of this zone consists of polyelectrolyte loops "dangling" from the film network into the solution.

The zone II (core zone) or "bulk film" frequently contains 1:1 stoichiometric polyelectrolyte complex. The zones I and III are formed during the first step in the deposition process. After these zones finalize their composition and thickness, the zone II forms and increases in thickness during the assembly process.

While zone I and zone III possess a small gradient of charge excess, the zone II is assumed to be electrostatically neutral due to the charge compensation of two oppositely charged polyelectrolytes. The borders between zones I and II and zones II and III are smooth. The thicknesses of the zones are defined by the substrate nature, the chemical structure of deposited polyion pair and conditions of the deposition process.

1.2.3. LbL growth regimes

There are two growth regimes for multilayered films. The LbL film is said to exhibit linear growth if its thickness and the amount of polyelectrolytes deposited on the surface of the substrate increases linearly with the layer pair number. The film possesses a somewhat fuzzy layered structure (Figure 8) as described above (see 1.2.2), and each polyelectrolyte layer forms an interpenetrating network with the closest neighbors.

Another growth regime, referred to as exponential, occurs, while it is possible for at least one of the components of the film to diffuse in and out of the film matrix at each layer deposition step.

One of the first examples of exponentially growing films was demonstrated by Elbert and co-workers. The film based on PLL and alginate (Alg) was constructed as a non-adhesive barrier for the cells on the top of the gelatin layer. At the physiologic pH the thickness of the dry film measured by

ellipsometry grown exponentially during the deposition of each polyelectrolyte layer (*22*).

Later, Picart et al. investigated the exponential growth of a multilayer film contained PLL and hyaluronic acid (HA) by optical waveguide lightmode spectroscopy, streaming potential measurements, atomic force microscopy and quartz crystal microbalances (QCM) (*23*). It was shown that $(PLL/HA)_n$ film build up proceeds via two different regimes. First regime corresponds to the formation and growth of isolated islands and islets on the top of the substrates, while the second stage of the films formation represents the coalescence of the islands to a homogeneous flat film. The authors suggested that the exponential growth of the film occurs due to the diffusion of free polyelectrolyte chains in and out the film, while the film is in contact with corresponding polyelectrolyte solution. The diffusion of PLL molecules during the deposition process was further confirmed by confocal laser scanning microscopy with fluorescently labeled PLL and HA molecules (*24*).

Based on these observations, the model of exponential growth regime was described by Lavalle et al. in 2002 (*25*). It was suggested that the films assembled with poly(glutamic acid) (PGA) and poly(*L*-lysine) contain two kinds of PLL chains: the first type of the chains strongly interacts with oppositely charged PGA and forms the multilayer network, whereas the second type of PLL macromolecules weakly binds to the film and thereby exhibits a certain mobility. Upon the formation of new PGA layer, the PGA macromolecules strongly interact with the PLL chains forming the top layer of the film (Figure 9). The mobile PLL chains then start to slowly diffuse out of film network, reach the film/solution interface, where they react with PGA chains from the solution forming PLL/PGA complexes. Further, these complexes interact with each other and form large entities. After most of the mobile PLL chains reach film surface, PGA chains diffuse into the film that leads to the surface charge overcompensation. While most of the free PGA chains diffuse out of the film after rinsing with buffer solution, the weakly bound PGA chains remain within the film. This process repeats during the deposition of the following PLL layer.

Exponential growth switches over to the linear regime after a certain number of deposition steps even if the diffusion of the polyelectrolyte still takes place. The switch from exponential to linear growth is thought to be due to the fact that polymer cannot reach the bottom of the film during the deposition time for this specific layer.
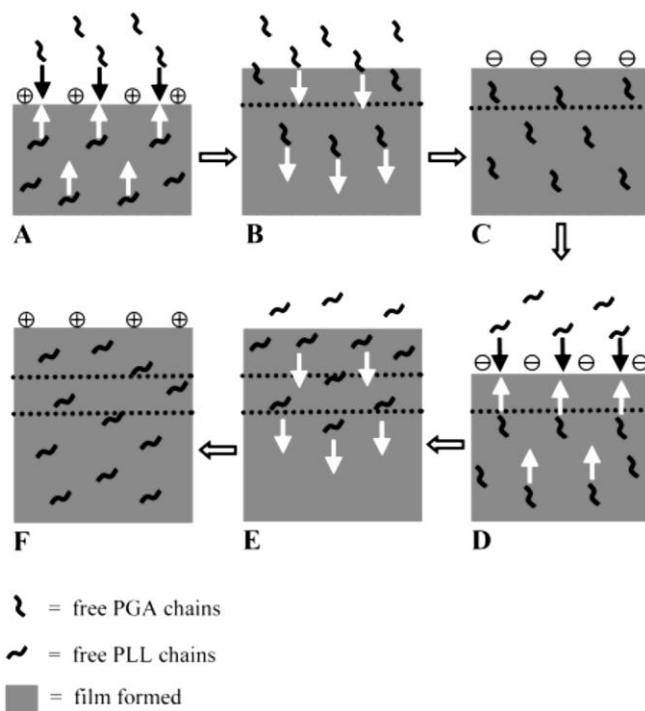
Figure 9. *Schematic model of exponential growth regime of (PGA/PLL)$_n$ film (25).*

1.3. Biological applications of PEC

1.3.1. LbL films as substrates for cell adhesion

Layer-by-Layer films were extensively exploited for the development of the substrates intended to control cell attachment and growth.

It was demonstrated that the cell adhesion can be manipulated by tuning the conditions of multilayer buildup, chemical composition, topology and rigidity of the films.

Richert et al. demonstrated that the cell adhesion properties of the multilayer films based on PLL and poly(*L*-glutamic acid) (PLGA) were defined by the pH of polyelectrolyte solutions used for film assembly. The films assembled at pH=4.4 possessed cell adhesive properties, while the architectures built at pH=10.4 prohibited cell attachment. It was suggested that the properties of multilayer coating are governed by their secondary structures and the differences in the film swelling properties (*26*).

Mendelsohn and co-workers reported that the assembly of (PAA/PAH) layers at pH=6.5 supports cell growth, whereas the preparation of the films under acidic conditions (pH=2) results in the formation of bioinert coating (*27*). The drastic difference of the cell behavior was associated with the changes in the PAA charge density within the film (Figure 3). Highly ionically linked films attracted cells, while the weakly ionically linked multilayers tend to swell in physiological conditions developing highly hydrated surfaces, which resist fibroblasts attachment (Figure 10).
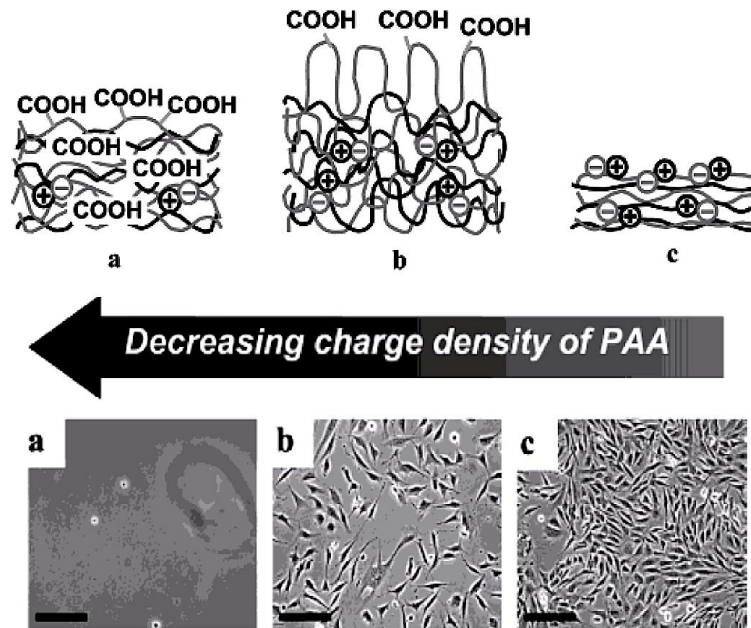
Figure 10. *Schematics of the film structures and phase contrast micrographs of murine NR6WT fibroblasts seeded onto (a) a (PAH/PAA)$_{20}$ film prepared from the solutions of PAH and PAA at pH=2.0 (b) a (PAH/PAA)$_{20}$ film prepared from the solutions of PAH and PAA at pH=7.5 and 3.5, respectively (c) a (PAH/PAA)$_{50}$ film prepared from the solutions of PAH and PAA at pH=6.5 (27).*

It was also demonstrated that the layers prepared at pH=6.5 and then treated at pH=2 possess cytophobic properties. Moreover, subsequent treatment of the same substrate at pH=6.5 led to the regeneration of the cytophilic properties of the film (*28*).

Other important parameters, which contribute to the cell-substrate interactions, are surface rigidity and topology.

Richert et al. demonstrated that the increase in the rigidity of the (PLL/HA)$_n$ films by their chemical crosslinking improves the smooth muscle cell adhesion properties of LbL films. The crosslinking not only turns the layers cytophilic but also improves their resistance to enzymatic degradation (*29*).

In 2009 Moussallem and co-workers demonstrated that the phenotype of

smooth muscle cells can be controlled by the flexibility of the films (*30*). Since the (PAH/PAA)$_n$ films were prepared at different pH of polyelectrolyte building solutions and therefore differed in their thickness, the thermal crosslinking of the multilayers yielded the formation of coatings of various rigidity and charge. The films prepared at pH 7.4 (solution of PAH)/4.6 (solution of PAA) were thicker and more flexible compared to films prepared at pH=7.4 for both polyelectrolyte solutions. It was found that cells phenotype was modulated with respect to the LbL mechanical properties (Figure 11).
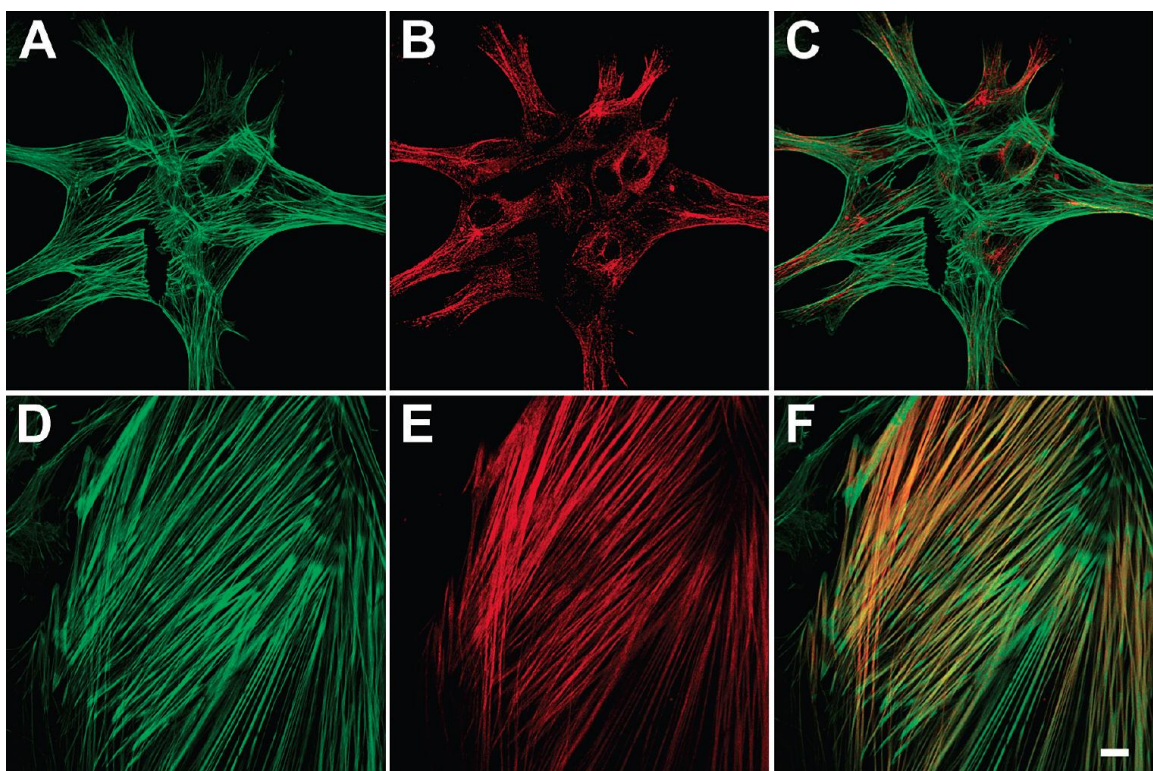
Figure 11. *Localization of total actin and smooth muscle R-actin in A7r5 cells cultured on native and cross-linked (PAA/PAH) films. Cells were grown on native (A-C) and cross-linked (D-F) (PAH/PAA)$_4$/PAH-coated coverslips. Actin filaments are stained with Phalloidin-Alexa 488 (green) and smooth muscle R-actin is labeled with a specific anti-R-actin antibody and Alexa 546-secondary antibody (B and E). Overlaid dual-labeled images (C and F); scale bar 10 µm (30).*

Boudou et al. studied the correlation between the mechano-chemical properties of native and crosslinked (PLL/HA)$_n$, (CH/HA)$_n$ and (PAH/PGA)$_n$ and the adhesion of skeletal muscle cells and NIH 3T3 fibroblasts. It was demonstrated that independently of the film composition and the presence of serum proteins, the cells better adhered, spread and proliferated faster on the crosslinked films forming stiffer surfaces (*31*).

The properties of LbL architecture can be altered by the incorporation of adhesive proteins into the films. Kirchhof et al. compared osteoblasts MG-63 cell adhesion onto the substrates coated with (CH/HEP)$_n$ multilayers with or without terminal layer of plasma fibronectin (*32*). The highest cell population was achieved on the LbL-coated substrates terminated with fibronectin, due to the presence of cell binding motifs such as RGD on the film surfaces. Moreover, the cell population was found to be higher on the coating with chitosan layer under that of fibronectin compared to the architecture with the layer of heparin preceded fibronectin layer.

Another possibility to improve cell adhesion properties of the LbL films is the post-functionalization of the terminating layer with bioactive molecules. One of the examples of such approach was demonstrated by Kinnane and co-workers (*33*). The authors reported the preparation of the anti-fouling poly(ethylene glycol) (PEG) films covalently assembled via Cu(I)-catalyzed cycloaddition of alkaline and the azide groups incorporated into PEG polymer chains and carboxylic groups in RGD. The prepared films were further modified by grafting the RGD sequence via click reaction with the free azide groups in the PEG. While the monkey kidney epithelial cells were poorly interacting with the native architectures, the cell adhesion and proliferation were enhanced on the substrates functionalized with RGD.

In another work, the effects of polyelectrolytes PAH and PAA in the solution or embedded into the film on the cell metabolism, proliferation and survival were studied. The experiments were carried out with rat aortic smooth muscle cells and osteosarcoma cells. It was shown that the solution of positively charged

PAH was much more toxic to both cell types compared to that of negatively charge PAA and caused necrotic cell death. By contrast, the low concentration PAA solutions were well tolerated by the cells, whereas at higher concentrations PAA induce the increase in cell metabolism (*34*). The incorporation of the polyelectrolytes into the films reduces their cytotoxic and cytostimulatory effects. It was observed that, regardless the thickness, the PAH-terminated films caused lower cell proliferation compared to those with the PAA outmost layer. Moreover, the thicker (PAA/PAH)$_n$ films yielded lower cell density than the thinner ones. The authors concluded that the electrostatic interactions between film components reduce their availability for cellular uptake or for the interaction with the cell membrane.

Layer-by-Layer assembly is successfully applied for the improvement of biocompatibility and antimicrobial properties of the implantable substrates (*35*). Kerdjoudj and co-workers described the preparation of cryopreserved vessels modified with LbL film with improved mechanical properties (*36*). The use of cryopreserved arteries for vascular tissue engineering meets certain limitations since the cryopreservation induces structural changes of the vessels, which generate the alteration in the biomechanical properties of the implanted vessels. Moreover, the cryopreservation provokes the loss of endothelial cells, leading to the direct interaction of blood components with extracellular matrix. These undesirable interactions induce thrombosis and/or restenosis after implantation. To improve the endothelial cell adhesion onto the vessel, the luminal surface of cryopreserved umbilical arteries was covered by (PAH/PSS)$_3$/PAH films. The multilayer coating improves the mechanical properties of the defrosted vessels allowing to decrease the maturation time of vascular grafts. It was demonstrated that coated implants enhance cell adhesion and spreading (Figure 12). By contrast with the uncoated arteries, the cells seeded onto the multilayer-coated vessels exhibit flat and elongated morphology, keep their phenotype and form sub-confluent monolayer compared to the uncoated arteries. LbL-coated vessels maintain their functionality being

similar to that of fresh arteries and therefore present novel biocompatible grafts with improved biomechanical and anti-thrombogenic properties.
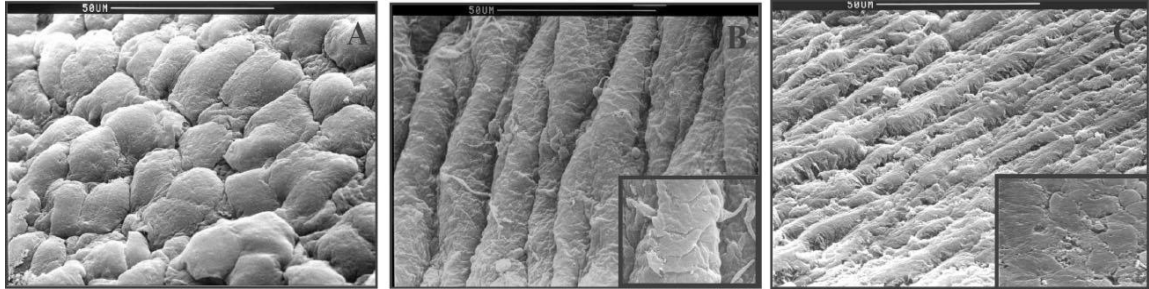
Figure 12. *Scanning electron micrographs of untreated (A), covered with LbL film (B) cryopreserved umbilical arteries with endothelial cells and fresh umbilical arteries (C) (36).*

Recently, Davila and colleagues presented a new type of mechanotransductive film, where the layers made of RGD-grafted polyelectrolytes were assembled under the nonadhesive layers bearing phosphocholine (*37*). This LbL film supported cell adhesion upon the stretching by rendering RGD-ligands accessible to the cells and inducing cell adhesion through specific interactions. The effect was found partially reversible upon the relaxation due to the film restructuring that led to the only a partial remasking of RGD peptides.

1.3.2. Gene delivery systems

The primary challenge of gene therapy is a development of a safe and efficient method to deliver exogenous genetic material to the target cells and induce the production of the therapeutic proteins correcting or modulating damaged cellular functions. The transfer of the exogenous nucleic acids – transfection – is one of the stages in gene therapy process (*38-41*).

Due to their properties such as large size, negative charge and hydrophilicity, nucleic acids (DNA or siRNA) cannot easily cross the cellular membrane and

need to be incorporated into a system – vector – that facilitates cell binding and internalization and protects genes from degradation. Depending on the nature of the vector, the methods of gene therapy can be divided on viral and non-viral approaches.

Currently, viruses are the most efficient particles for injecting DNA into the target cells. However, the broad use of viruses that were genetically gutted of their genetic material and replaced with therapeutic genes (*42*) is limited due to the possible side-effects such as immunogenicity and oncogenic effects via random transgenic insertion of viral genetic material into the host chromosome followed by disruption of normal gene expression (*43*).

Methods of non-viral gene delivery present a promising alternative to viral vectors and include two main groups: physical and chemical methods.

Physical methods employ physical force that induces the defects in the cell membrane giving an opportunity to nucleic acids enter the cell, and include gene gun (mechanical forces), electroporation (electric forces), hydrodynamic (hydrodynamic forces) and ultrasound-facilitated gene transfer methods as the main gene delivery techniques (*39, 44*).

1.3.2.1. Polycation/DNA complexes for gene delivery

A common approach for delivering nucleic acid by chemical methods includes the formation of interpolyelectrolyte complexes (polyplexes) through electrostatic interactions between negatively charged phosphate groups of nucleic acid and positively charged groups of macromolecules (*45, 46*).

The general requirements for synthetic delivery system include 1) the ability of a macromolecule to effectively condense nucleic acid to particles with a size appropriate for cellular uptake 2) the enhancement of the complex binding capacity to the cell surface by masking DNA negative charge 3) protection of

DNA from degradation in extra- and intracellular environment and 4) delivery of genetic material to the site of action.

Currently, most of the non-viral delivery systems bear amine-based positively charged groups and include various polymers, dendrimers, lipids and peptides (*47-50*). The composition of the polyplexes is characterized by N/P ratio - the molar ratio between polycation groups containing nitrogen and negatively charged phosphate groups of DNA.

The transfection efficiency of the non-viral vectors is defined by many factors such as type of cell line, chemistry of nanoparticles, surface charge, size, stability of the aggregates, their solubility in the cell culture conditions and ability of the polycation to protect the nucleic acid from degradation into the cell environment (*47-49*).

1.3.2.2. Formation of polycation/DNA complexes

The mechanism of the complex formation is similar to that described for the synthetic polyions (see section 1.1.2). The mixing of aqueous solutions of nucleic acid and polycation leads to the formation of soluble PECs via cooperative interactions between electrostatically complementary chains.

In general, the molecular mass and the contour length of polycations are much lower than those of recombinant DNA molecules and therefore the polycations can be considered as "a guest" and DNA as "a host" (*45, 46*)

At low N/P ratios, while the concentration of DNA is higher than that of polycation, the water-soluble negatively charged nonstoichiometric complexes form. The charge of the complex increases with the content of polycation. At certain critical polycation concentration the two types of PECs form: nonstoichiometric complexes that stay in the solution and stoichiometric complexes formed in the excess of polycation macromolecules that either

precipitate or aggregate. The fraction of stoichiometric complexes increases with polycation concentration.

At N/P 1, while the molar concentrations of DNA and polycation are equal, all chains of nucleic acid are involved in the formation of stoichiometric complexes (*46*).

Sedimentation studies showed that DNA incorporated into PEC possesses a more compact structure. The investigation of DNA condensation process with poly(L-lysine) covalently coupled to glycoprotein asialoorosomucoid was performed by Golan and co-workers (*51*). It was demonstrated that depending on the composition of the polyplexes (N/P ratio), the complexes exhibited either toroid or short rod shape with thickness similar to that of chromatin fibers.

1.3.2.3. Poly(ethylenimine)

Poly(ethylenimine) (PEI) is considered as one of the most effective synthetic gene transfer agents (*52*).

Depending on the synthesis, linear or branched PEI is obtained. Both derivatives can be used as transfection agents. Synthesis of branched PEI is performed via cationic polymerization, while the linear form is obtained as a product of ring-opening polymerization and subsequent hydrolysis (Figure 13) (*49, 52, 53*).
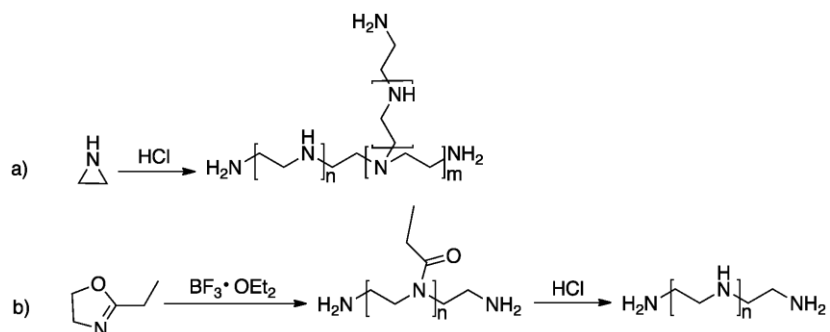
Figure 13. *Synthesis of branched (a) and linear (b) PEI.*

Since each monomer unit contains an amino group, PEI possesses a high charge density that allows to condense DNA into the small particles. The size of the particles is strongly dependent on the complex formation conditions and is discussed later.

Poly(ethylenimine) demonstrated high transfection efficiency due to enhanced endosomal release via the so-called "proton sponge" effect. At physiological pH only 20% of the amine groups in PEI are protonated, while at pH=5 their concentration increases up to 45%. During intracellular traffiking PEI inhibits the nuclease activity due to its buffering capacity and induces the accumulation of protons within the endosome coupled to an influx of chloride anions. The presence of PEI alters the osmolarity of the endosome resulting in osmotic swelling. The protonation of PEI enhances charge repulsion of polymer chains and therefore induces swelling of polymer network. Both of these effects lead to the rupture of the vesicle and to the release of the carrier into the cytoplasm (*54*).

For efficient binding to the cell surface, the polyplexes are prepared in excess of PEI and therefore possess a net positive charge (*53*). However, it was demonstrated that at high N/P ratios the particles induce undesirable toxic effects due to the vector aggregation on the cell surface followed by cell membrane rupture (*55, 56*).

The degree of branching influences gene transfection efficiency and cytotoxicity. Although branched PEI is more effective in the DNA condensation and exhibits high transfection ability, linear PEI shows better efficiency in multiple *in vivo* studies (*57, 58*).

Molecular weight of PEI is another important parameter influencing polyplex formation, transfection capacity and toxicity. It was demonstrated that the efficiency and the toxicity of polyplexes increases with PEI molecular weight. The optimal molecular weight was found to be between 5 and 25 kDa (*53*).

1.3.2.4. Transfection mechanism

After DNA/polycation complex is added to the cell culture, the first barrier it has to overcome is to pass through cellular plasma membrane (Figure 14). As stated above, the passive diffusion is not possible, but since polyplexes are positively charged they can bind to the cell membrane through ionic interactions with proteoglycans – membrane-associated core proteins that bear sulfated or carboxylated glycosaminoglycans (GAGs): chondroitin sulfate, dermatan sulfate, keratan sulfate, heparan sulfate and hyaluronan. GAGs are highly negatively charged. The content of GAGs depends on the cell type and is associated with transfection efficiency (*59-61*).
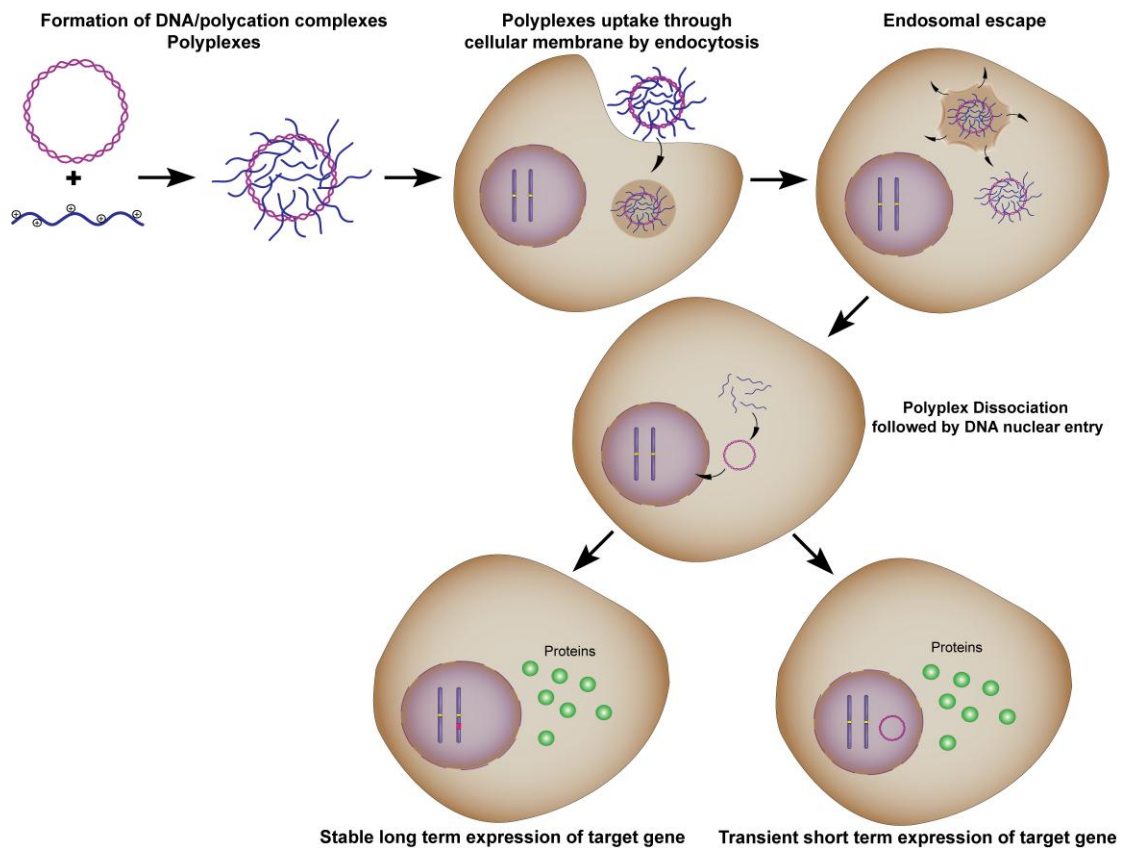
Figure 14. *Schematics of transfection mechanism.*

Endocytotic uptake of the polyplexes proceeds via multiple mechanisms: clathrin- mediated endocytosis, caveolae-mediated endocytosis, macropinocytosis, phagocytosis and clathrin- and caveolae – independent endocytosis (*62*). The pathway of uptake depends on cell line, polyplex properties and the polyplex formation conditions and can be controlled by chemical modification of vector with targeting ligands or cell penetrating peptides (*62-64*).

The second important stage is the escape of polyplexes from endosomes to avoid their enzymatic degradation within the lysosomes. Incorporation of DNA molecules into the polyplexes mediates its accessibility to nucleases in the cytosol. It was demonstrated that the restriction of DNA embedded into a complex consisted of two stages: 1) fast cleavage of the DNA fragments not covered with polycation chains and 2) slow restriction of DNA in the polyplexes. Since the chains of polycation are not strongly attached to those of DNA, they migrate from one DNA molecule to another opening the sites for cleavage. Thus, the kinetics of second phase depend on the migration ability of polycation molecules (*45, 65*). After nuclear entry occurring through nuclear pores or during mitosis (*66, 67*), gene expression should take place. Stable, long-term expression is achieved through insertion of gene into host genome whereas transient short-term expression occurs from transgene retention within the nucleus.

1.3.3. Layer-by-Layer assembly as a platform for surface-mediated transfection

The first report by Lvov and co-authors in 1993 of the DNA incorporation into the multilayer films demonstrated the possibility to apply the LbL assembly in the field of the gene delivery (*68*). The surface-mediated transfection provides several advantages compared to the bulk transfection methods such as spatial and temporal control over the DNA loading in the films as well as the possibility to incorporate different types DNA at different film levels.

In this part, several examples of efficient DNA delivery by LbL films are presented.

One of the approaches for the promoting the surface-mediated transfection is based on applying hydrolytically degradable cationic polymers for the film construction.

In 2005 Jewell et al. reported the use of DNA-containing multilayer films that gradually release DNA in physiological conditions. The film was built up using pDNA coding green fluorescent protein and Polymer 1 (Figure 15) on the quartz slides precoated with (PEI/PSS)$_n$ precursor layers (*69*). Polymer 1 is positively charged at pH=5 and belongs to the class of hydrolytically degradable (at neutral pH) synthetic polymers, (poly(β-amino ester)s. After the incubation of COS-7 cells with the LbL-coated samples during 48h, the majority of transfected cells were located directly under the LbL-coated substrate, which therefore provides the spatial control over the DNA delivery (Figure 15). It was suggested that the film released the condensed pDNA and therefore enhanced the transfection efficiency. Later study confirmed the presence of small aggregates from 100-600 nm in PBS used to incubate (Polymer1/DNA)$_n$ film (*70*).
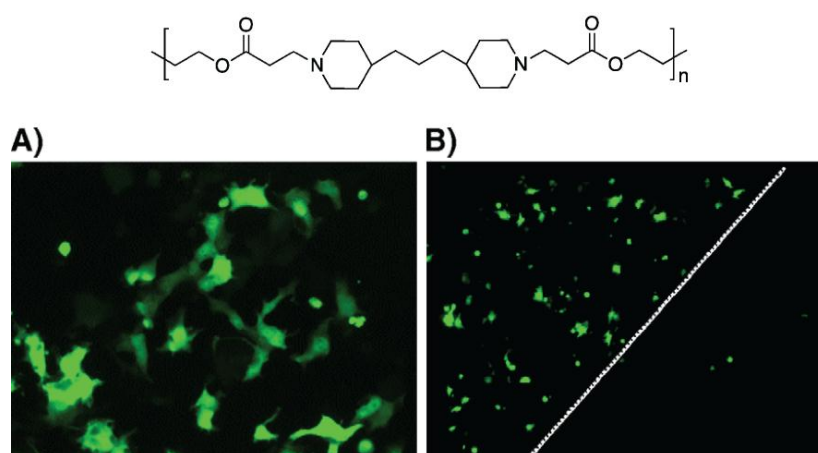
Figure 15. *Structure of Polymer 1 and fluorescent microscopy images of transfected COS-7 cells located under the film-coated substrate (A) and on the edge of a film-coated slide (indicated by white dotted line) (69).*

Recently, it was demonstrated that these films can be used to deliver pDNA across the skin (*71*). The insertion of the micrometer-scale needles (~750 μm long) coated with (Polymer1/fluorescently labeled DNA) film into the porcine cadaver skin over 2-h period allowed the deposition of the DNA along the needle track to the depth of 500-600 μm (Figure 16).
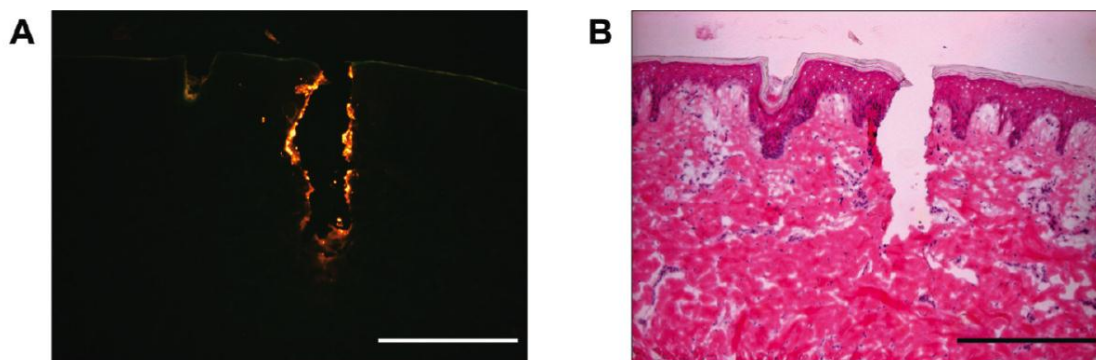
Figure 16. *Representative fluorescence microscopy images (A) and companion histology images (B) of porcine cadaver skin after insertion and removal the microneedles coated with polymer 1/fluorescently labeled DNA). Scale bars 400 μm (71).*

The LbL assembly allows to construct the films that release DNA under particular conditions.

It was shown that the application of the reduction potential to the (Polymer1/DNA)$_n$-coated electrode generated a rapid release of DNA over the periods of 1 to 2 min (*72*). The applied potential provokes the increase in the solution pH near the electrode surface resulting in the hydrolytic polymer degradation. DNA released under these conditions remained active and promoted the gene expression in COS-7 cells.

Chen and co-authors applied the cationic poly(amidoamine) polymer (Figure 17) containing di-sulfide bonds for the construction of LbL film containing DNA (*73*). While stable in PBS buffer, this film disassembled in the presence of reducing agent dithiothreitol (DDT). The rates of film erosion correlated with the

concentration of DDT. The highest film disassembly rate (30 min) was achieved in the 10 mM DDT solution, whereas the reduced DDT concentration (1 mM) generated the film erosion during 9 days.
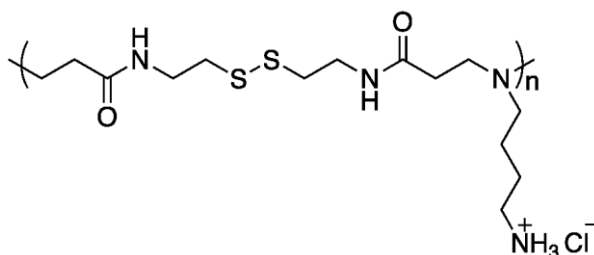
Figure 17. *Structure of cationic poly(amidoamine) polymer used in (73).*

Blacklock and colleagues applied the reducible hyperbranched poly(amino amine) (Figure 18) and DNA encoding the secreted alkaline phosphate (SEAP) and GFP for film construction on the flexible stainless steel substrate (*74*). The release of pDNA was thought to proceed via the contact with reducing environment of plasma membrane. *In vivo* this film showed higher transfection efficiency compared to that of lPEI/DNA-based polyplexes. The *in vivo* efficiency of the films was evaluated by implanting the coated substrate and measuring the SEAP level in the blood circulation of rats. The higher blood level of SEAP was registered on the day 5 after the implantation followed by sharp SEAP level decline due to the formation of collagen fibrous capsules near the substrate that created a barrier for sufficient distribution of SEAP in the blood. Later, it was reported that the transfection activity of this kind of film depends on the film rigidity and roughness and can be controlled by the salt concentration of polymer solution used for LbL assembly (*75*). The transfection efficiency was found significantly higher for the cells grown on the rigid film.
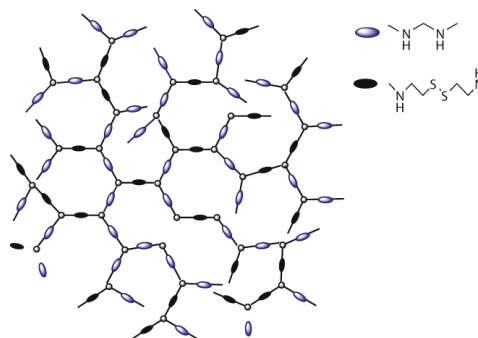
Figure 18. *Structure of the reducible hyperbranched poly(amino amine) used in (74).*

1.4. Quartz crystal microbalance/Cell studies

The variety of cellular functions and properties that depend on the cytoskeleton rearrangements such as adhesion, spreading, mitosis, apoptosis…are often studied by the methods of flow cytometry or microscopy (*76*). Both methods require the additional steps of the cell labeling or staining, which limit their application for *in situ* characterization of the cell properties.

Quartz crystal microbalance is a technology applied for studying the changes in mass and viscoelastic properties near the surface of the sensor via the changes of the resonance frequency and energy dissipation of oscillating quartz crystal (see section 2.4, Materials and Methods). It is therefore commonly used for monitoring the formation and the properties of the thin films of polymers, proteins, lipids, DNA…at the surface of the sensor (*77*).

Aside from the information about the deposition of the thin films, quartz crystal microbalance with enhanced dissipation (QCM-D) is capable of providing the *in situ* characterization of living cells. Since cytoskeleton framework determines the cell mechanical properties, it is therefore possible to follow its rearrangements by measuring the changes in the QCM-D sensor frequency and energy dissipation.

In this section, several examples of the application of QCM-D for characterization of living cell properties are described.

One of the pioneering works of studying the cell adhesion on the surface of QCM-D sensor was performed by Fredriksson and co-workers (*78*). These studies were carried out using either the native gold polystyrene-coated QCM-D sensor (hydrophobic surface) or those treated by ozone under UV irradiation (hydrophilic surface). The experiments were performed in the serum-free medium with two cell lines: Monkey kidney epithelial cells and Chinese hamster ovary epithelial cells. It was shown that the cell adhesion resulted in the decrease in the resonance frequency corresponding to deposition of the effective mass on the electrode surface, while the energy dissipation increased due to the viscoelastic energy losses. The authors demonstrated that the QCM-D response strongly depends on the cell type adhered on the same type surface and on the type of the surface under otherwise identical experimental conditions.

Later, Nimeri and collegues demonstrated that the QCM-D technique can be used to monitor the specific cell adhesion onto the sensors surfaces covered with immunoglobulin G (IgG), human serum albumin (HSA) or fibrinogen (*79*). Although the attachment of neutrophils onto the sensors surface resulted in the frequency decrease and increase in the energy dissipation, the shape and the magnitude of the QCM-D response were particular for each protein-covered surface. The better cell spreading onto the surface coated with IgG generates higher decrease in the resonance frequency compared to the frequency shift for cells exposed to the HSA- or fibrinogen-coated surface.

Lord and co-workers demonstrated that QCM-D is capable of detecting the differences in the cell adhesion, which are not detectable by fluorescence microscopy (*80*). In this work, the adhesion of NIH3T3 fibroblasts to tantalum or oxidized polystyrene covered QCM-D sensors coated with serum proteins such as bovine serum albumin (BSA), human fibronectin or newborn calf serum proteins was studied in the serum-free medium over the period of either 2 or 4h. The QCM-D responses detected for the cells seeded at non-adhesive albumin covered surface were similar for both kinds of sensors. The fluorescence microscopy studies of the cells adhered to the sensor surfaces covered with

fibronectin or newborn calf serum proteins revealed similar compact and spread cellular morphology. By contrast, the QCM-D responses for each surface remained different indicating that the process of cell adhesion and spreading proceed via extracellular matrix (ECM) remodeling and different membrane activities depending on the protein coating and the underlying substrate.

Saravia and Toca-Herrera studied the adhesion process of human hepatoma cell line onto the surface covered with poly(ethylenimine) or PEI(PSS/PAH)$_2$/PSS layers by QCM-D and optical microscopy (*81*). It was shown that the sensors coated with positively charged PEI supported cell attachment and spreading resulting in higher frequency shift.

The QCM-D technique can be used for the monitoring of cell signaling processes. Chen and co-workers studied the short-term responses of human carcinoma cells to epidermal growth factor via changes in viscoelastic properties of a cell layer on the QCM-D sensors due to the cytoskeleton reorganization (*82*). It was demonstrated that the stiffening of the EGF-treated cells due to the activation of high-affinity epidermal growth factor receptors (EGFR) generates rapid decrease in the dissipation signal, while the increase in the frequency is affected by calcium influx and is defined by the signaling of low-affinity EGFR.

Fatisson et al. extended the application of QCM-D technique by using it for *in situ* detection of cytoskeleton changes in primary endothelial cells treated with two cytomorphic agents, namely, Triton-X 100, acting as a membrane disrupter and leading to the cell lysis, and bacterial lipopolysaccharide which induces the cell rounding (*83*). It was shown that the cell response to the different cytomorphic agent produces characteristic QCM-D signals with the shape and intensity defined by the different interaction of the agents with cells. The intensity of the induced changes of QCM-D signals correlated with the concentration of the injected substance.

QCM-D sensors were applied for studying the microtubule network dynamics. Marx and co-workers studied the QCM-D responses of endothelial cells upon

the exposure to the different microtubule binding drugs, namely, taxol and nocozole (*84*). At low concentration nocozole *in vitro* and *in vivo* depress microtubule dynamic instability and disassembles the network at high concentrations in the variety of eukaryotic cells. Taxol is an antitumor drug used to treat various cancers, and it causes microtubules hyperstabilization and bundling. It was shown that the QCM-D response for taxol was quite different from that for nocozole. Whereas the injection of Nocozole to the confluent layer of endothelial cells produces an immediate significant decrease in the frequency corresponding to the rounded but attached cells, the incubation of the cells with taxol resulted in slow increase in the frequency 4h after injection. It was stated that after 4h the cells undergo taxol-mediated apoptosis, which resulted in a slow increase in the frequency.

The potential application of QCM-D as a diagnostic tool for detecting target cells in the patient blood samples was discussed (*85*). The integrated QCM-D immunoarray consisted of four kinds of leukemic lineage-associated probes to explore the differentiated leukocyte antigens for immunophenotyping of acute leukemia. The detection of target cells *in situ* was performed by monitoring the changes in the frequency shift after the injection of whole blood samples. It was shown that the frequency decrease was significally larger for granulocyte-positive samples compared to the control tests (normal blood samples). The improvement of the selectivity of the immunoassay array was achieved by deposition of protein-conjugated gold nanoparticles (*86*) or magnetic nanoparticles (*87*).

Recently, Tymchenko and co-workers studied *in situ* cell attachment and spreading by QCM-D combined with light microscopy that facilitated the interpretation of QCM-D signals at different stages of the experiment (*88*). It was observed that after cell seeding (Figure 19, A) the attachment and spreading (Figure 19, B and C, respectively) of NIH3T3 fibroblasts or human dermal fibroblasts onto collagen- and fibronectin -coated sensors yielded slight positive frequency shift and pronounced immediate increase in energy dissipation. After the spreading, the cells were exposed to cytochalasin D, a

cytoskeleton perturbing non-toxic agent that induces reversible changes in viscoelastic properties of the cell layer. The cell rounding upon the interaction with cytochalasin D was observed by light microscope accompanied by the large positive shift in the energy dissipation for both cell lines. It was demonstrated that the changes in the QCM-D signals were reversible as the cytochalasin D was removed from the QCM-D chamber.
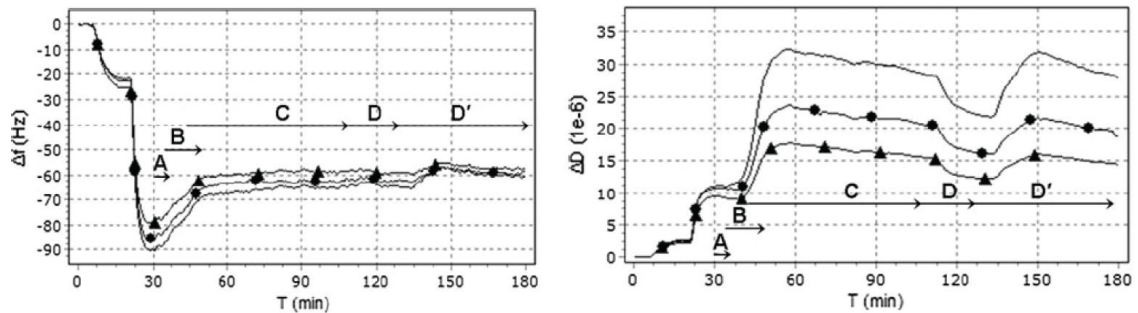
Figure 19. *QCM-D frequency and dissipation signals for 3T3 cells. (A) cell seeding, (B) cell attachment and (C) cell spreading. The phases were assigned by light microscopy. (D) the exposure of cells to cytochalasin D and (D`) cell recovery after rinsing with medium (88).*

2. Materials and Methods

2.1. Materials

Branched poly(ethylenimine) (Lupasol WF, M_w ~ 25 000 g/mol) was purchased from BASF (Ludwigshafen, Germany). Poly(allylamine hydrochloride) (M_w ~ 15 000 g/mol), poly(diallyldimethylammonium chloride) (M_w ~ 100 000 - 200 000, 20% water solution), chitosan (low molecular weight, 75-85% deacetylated), dextran sulfate sodium salt from *Leuconostoc spp.* (M_w ~ 6 500 - 10 000), alginic acid sodium salt from *brown algae* (medium viscosity), poly(sodium 4-styrenesulfonate) (M_w ~70 000 g/mol), poly(*L*-lysine) hydrobromide (M_n ~ 15 000 - 30 000 g/mol), poly(*L*-ornithine) hydrobromide (M_n ~ 30 000-70 000 g/mol), poly(*L*-glutamic acid) sodium salt (30 000 - 70 000 g/mol), sodium hexametaphosphate and sodium chloride (≥99.5% pure, suitable for cell culture) were purchased from Sigma-Aldrich (Saint-Quentin Fallavier, France). Acetic acid (100%, ROTIPURAN®) was purchased from Carl Roth Gmbh (Karlsruhe, Germany).

Linear poly(ethylenimine) (jetPEI™, M_r 22 000 g/mol) was kindly provided by Polyplus Transfection™ (Illkirch-Graffenstaden, France). Plasmid DNA (gWiz GFP) was obtained from Aldevron (Fargo, ND).

Water used for the preparation of all solutions was purified with a Milli-Q water purification system (Millipore, Molsheim, France).

Silicon wafers were purchased from WaferNet Inc. (San-José, USA), quartz slides were bought from Thuet B (Blodelsheim, France), glass slides (diameter 20 mm) were purchased from Marienfeld-Superior (Lauda-Königshofen, Germany) and the QCM-D sensors were provided by Q-Sense AB (Göteborg, Sweden).

2. 2. Methods

2.2.1. Dynamic light scattering (*89*)

Dynamic light scattering (DLS) is a technique used to determine a size, shape and size distribution of nanoparticles in suspension.

Upon the interaction of molecules or nanoparticles with the light, the electromagnetic waves are scattered by these particles. If the light is scattered in all directions homogeneously, this process is called "elastic scattering".

Since in solution particles take part in a Brownian motion, the random changes in their positions induce the fluctuations of the electric field of the scattered light. The DLS method allows to determine the self-diffusion coefficient and the hydrodynamic radius of particles from the characteristic fluctuations of the scattered light intensity.

The information about the particle motion and the positions of the particles during the time is included in self-correlation function G_s:

$$G_s(\vec{r},\tau) = \left\langle N(\vec{0},t)N(\vec{r},t+\tau) \right\rangle$$

where *N* is the number of scattering particles in the scattering volume defined as an intersection of incident light beam and optical aperture.

Since the scattering volume depends on scattering angle θ, the detected intensity of scattered light in the DLS experiment is normalized to a constant scattering volume by $sin\theta$.

The self-correlation function expresses the probability of finding a given number of particles at the position defined by $\vec{r}$ at time $t + \tau$, if the same particles were

located at starting point defined by $\vec{0}$ at the moment *t.* The average is taken over the whole scattering volume and measuring time.
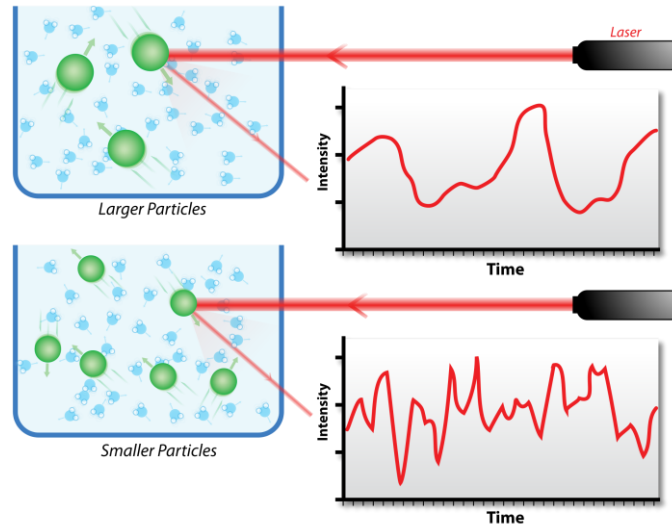
Figure 20. *Different shapes of self-correlation function for the samples containing large particles (top) and small particles (bottom) (90).*

For random motion the correlation function depends only on mean square displacement $\langle \Delta R(\tau)^2 \rangle$ as follow:

$$G_s(\vec{r},\tau) = \left[\frac{2}{3} \pi \langle \Delta R(\tau)^2 \rangle \right] \bullet \exp\left(-\frac{3r(\tau)^2}{2\langle \Delta R(\tau)^2 \rangle} \right)$$

For Brownian motion the mean square displacement of the scattering particle is proportional to self-diffusion coefficient D_s:

$$\langle \Delta R(\tau)^2 \rangle = 6 D_s \tau$$

Finally, the size of scattering particle can be found via the Stockes-Einstein equation, which describes describing the relation between the self-diffusion coefficient and the hydrodynamic radius (RH) of the particles if the solvent viscosity (η) and the temperature (T) of sample are known:

$$D_s = \frac{kT}{6\pi\eta R_H}$$

2.2.1.1. Experimental setup (91)

In this work the size distribution of polyplexes was measured by Zetasizer Nano ZS ZEN3600 instrument (Malvern Instrument, Ltd, UK) equipped with the 633 nm laser. The instrument allows to detect the particles with the size in the range from 0.6 nm to 6 µm.

After the laser light passed through the sample, the intensity of the scattered light is measured by the detector aligned at a scattering angle of 173° to the sample. The focus position of the laser beam within the sample is controlled by the software and can be changed by moveable lenses. For optimal detection of scattered light, the intensity of the sample illumination is controlled by an attenuator. The position of the attenuator is automatically read by the software during the measurements. The detected signal is transferred to the digital correlator, which measures the degree of similarity between two signals of scattering intensity over the period of time.

The information from the correlator is then transmitted to the computer and analyzed by the software to retrieve the size of the particles and the particle size distribution.

The diameter of the particles measured by DLS corresponds to the diameter of a sphere that has the same diffusion coefficient as the particle. The size

distribution is obtained by fitting a multiple exponential to the correlation function using the non-negative least squares algorithm.

The DLS particle analysis resulted in three types of distributions:

- The number distribution characterizes number of particles in the different size bins;
- The volume distribution shows the total volume of the particles in the different size bins
- The intensity distribution defines the intensity of the light scattered by the particles in the different size bins

In this work, the particle sizes were retrieved from the intensity distribution since these values are retrieved directly from the self-correlation function data.

2.2.2. ζ-potential (*92*)

The ζ-potential is one of the important characteristics of the colloidal particles in an electrolyte solution, since it allows to predict the interactions of the particles in the suspension.

2.2.2.1. Electrical double layer (EDL)

In the solid-liquid colloidal system, the charged particle placed in the contact with polar liquid induces a charge redistribution of ions in the surrounding interfacial region. The rearrangement of the ions results in the increase of the counter ions concentration near the particle surface and in the subsequent formation of the EDL. The EDL consists of solvent molecules and counter ions bound by strong Coulomb interactions to the particle surface and forming the so-called Stern layer (Figure 20).

The external part of the EDL contains ions involved in Brownian motion and presents the diffuse part of the EDL. In the diffusive layer there are two populations of the ions: the one that form a stable entity with the particle and move with the particle surface, the other one consists of ions and solvent molecules which do not travel with the particle and take part in Brownian motion (Figure 21). The imaginary boundary between these two populations is called the surface of hydrodynamic shear or slipping plane. Electric potential at this plane is called electrokinetic potential or zeta potential (ζ-potential).

The charge density ψ of the diffusive layer is described by Poisson–Boltzmann equation:

$$\nabla^2 \Psi = -\frac{e}{\varepsilon \varepsilon_0} \sum_j Z_j n_{nj} \exp\left(-\frac{eZ_j \Psi}{kT}\right)$$

Here e is the elementary charge, ε is the relative dielectric permittivity of the liquid, ε_0 is the electrical permittivity in vacuum, T is a temperature in kelvins, k is the Boltzmann constant, Z_j and n_{nj} are the number of charges and the bulk number concentration, respectively, of ion j.
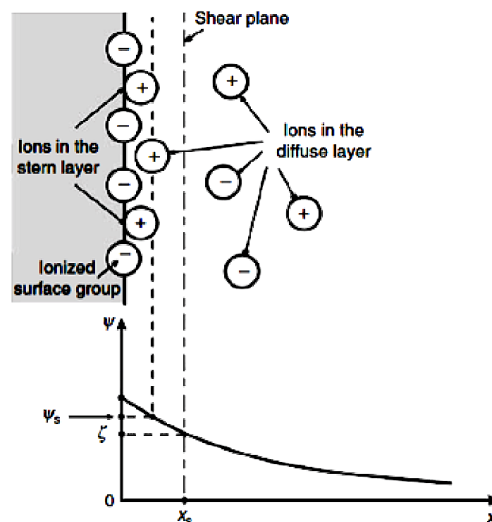
Figure 21. S*chematics of the electrical double layer structure.*

2.2.2.2. Electrophoretic mobility

Under the external electric field, the colloidal charged particles suspended in the electrolyte solution migrate to the surface of oppositely charged electrode.

For the spherical particles moving at constant velocity, the electrophoretic mobility µEL is defined by the Henry equation:

$$\mu_{EL} = \frac{2}{3} \bullet \frac{\varepsilon_0 \zeta}{\eta} \bullet f\left(k^{-1}R\right)$$

It is determined by the dielectric constant of the electrolyte solution, ζ-potential, viscosity of the medium η and the correlation function $f(k^{-1}R)$. The Henri function depends on the particle radius R and the Debye screening length, k^{-1}.
In colloidal suspension the Debye screening length is defined by the absolute temperature (T), dielectric constant ( ) and ionic strength of the electrolyte (I):

$$k = \sqrt{\frac{\varepsilon_r \varepsilon_0 k_b T}{2 N_A e^2 I}}$$

where N_A is the Avogadro number, k_b is the Boltzmann constant, ε_0 is the vacuum permittivity and e is the elementary charge.

Thus, a low concentration of the ions in suspension results in an extended electrical double layer, while higher ionic strength of the suspension leads to the reduced thickness of EDL.
Electrophoretic determinations of ζ-potential are most commonly made in aqueous media and of moderate electrolyte concentration. In this case $f(k^{-1}R)$ is 1.5, and this is referred to as the Smoluchowski approximation. The mobility and ζ-potential are proportional that fit the Smoluchowski model, i.e. particles

larger than about 0.2 microns dispersed in electrolytes containing more that 10^{-3} molar salt.

2.2.2.3. Experimental setup

The electrophoretic mobility of polyplexes was measured in a cell equipped with electrodes. When the potential is applied across the cell, the particles move to the oppositely charged electrode and their velocity is measured by the Laser Doppler Velocimetry method.

In this technique the initial laser beam is splitted by a cube beamsplitter, while a right-angle prism is used to obtain two parallel beams.
The probing beam passes through the cell with the sample, and the particles flowing through the illuminated area of the sample scatter the light. The receiving optics collects the light scattered at an angle 17° to the incident light beam, the reference beam and transfers it to the detector. The difference in the frequencies of incident and scattered light – Doppler shift – is retrieved by the digital signal processor.

The Doppler shift fd is defined as:

$$f_d = \frac{1}{2\pi}\left(\overline{k}_s - \overline{k}_i\right) \times \overline{V}$$

where $\overline{k}_s$ and $\overline{k}_i$ are the wave vectors of incident and scattred light, respectively, and $\overline{V}$ is the velocity vector of the particle.

It depends on the particle velocity V, the wavelength of the laser beam (λ) and the angle at which the scattered light is collected (α).The direction of particle motion is defined by β, the angle between the velocity vector and the bisector of ABC (Figure 22).

Thus,

$$f_d = \frac{2V}{\lambda}\cos\beta \bullet \sin\alpha$$
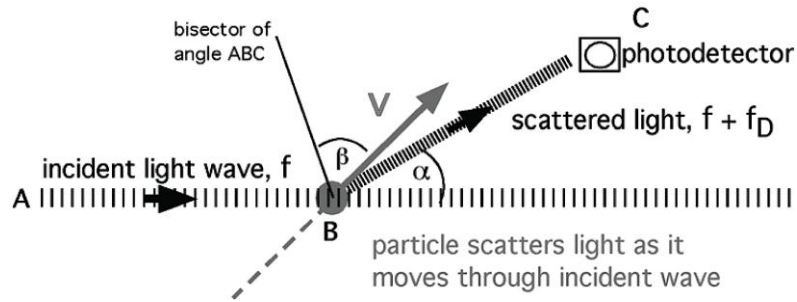
Figure 22. *Doppler shift imposed on light scattered from a moving particle (93).*

2.2.3. Ellipsometry (*94*)

Ellipsometry is an optical technique applied for the investigation of the thin films by measuring the changes in the polarization state of light when it is reflected from the surface of the sample.

2.2.3.1. Elliptically polarized light

The light is called elliptically polarized if the electric field vector of the wave draws an ellipse in any plane perpendicular to the direction of propagation. This ellipse is characterized by two ellipsometric angles ψ and Δ as shown in Figure 23.
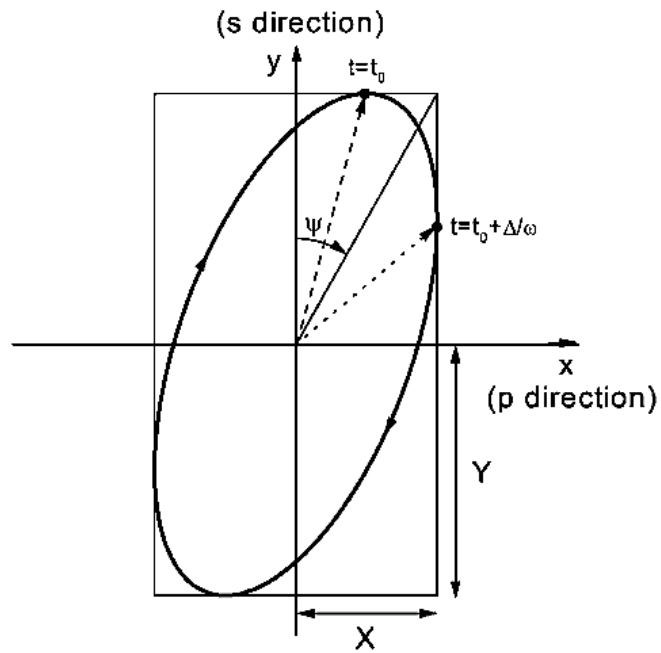
Figure 23. *The ellipse of polarization and its parameters.*

The angle *ψ* characterizes the ratio between the amplitudes of *s*-polarized (*E*-field polarized perpendicular to the plane of incidence *z* and *p*-polarized (*E*-field polarized parallel to the plane of incidence *z* of the reflected light:

$$\tan \Psi_{xy} = \frac{X}{Y}, \qquad \Psi \in \left(0, \frac{\pi}{2} \right)$$

The phase shift Δ is defined as an angle between the maximum values of X and Y components of the electric field vector reached at t=t0 and t=t0+Δ/ω respectively:

$$\Delta = \delta_x - \delta_y, \qquad \Delta \in \left(-\pi, \pi \right)$$

Two real parameters needed to characterize elliptic polarization of the light wave can be joined in the single complex value χ:

$$\chi_{xy} = \chi_r - i\chi_i = \frac{X \bullet \exp(-i\delta_y)}{Y \bullet \exp(-i\delta_x)} = \frac{1}{\tan\Psi_{xy}} \bullet \exp(i\Delta_{xy})$$

where χ_r and χ_i are the values of real and imaginary parts of the complex number χ.

For the monochromatic plane wave travelling along the positive direction of z-axis of the Cartesian right-handed coordinate system, the components of the electric vector along x and y are given:

$$E_x(t) = X \bullet \cos(-\omega t + \delta_x)$$
$$E_y(t) = Y \bullet \cos(-\omega t + \delta_y)$$

The polarization of such wave is described by the Jones vector with complex components:

$$\begin{bmatrix} E_x \\ E_y \end{bmatrix} = \begin{bmatrix} X \times \exp(i\delta_x) \\ Y \times \exp(i\delta_y) \end{bmatrix}$$

2.2.3.2. Ellipsometry measurements

Upon the interaction with the interface between two media with complex refractive indices N_1 and N_2, the incident monochromatic linearly polarized light is transformed to elliptically polarized light, which can be reflected from the interface at the angle φ_1 and/or transmitted by the interface at the angle φ_2, as shown in Figure 23.

The ellipsometry measurements allow to determine the ratio between reflection coefficients of s-polarized and p-polarized components of the electric field vector of the reflected light:

$$\frac{r_p}{r_s} = e^{i\Delta}\tan\Psi$$
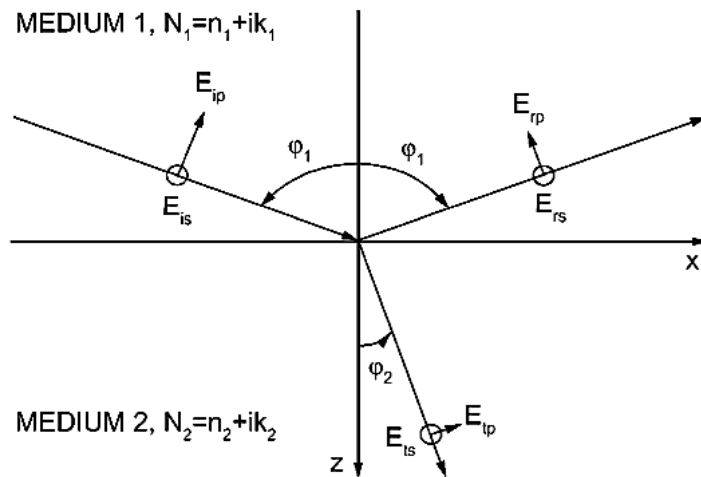
Figure 24. *The interaction of incident monochromatic electromagnetic wave with a planar interface. The components of the electric field vectors of incident, reflected and transmetted light are assigned as E_i, E_r and E_t, respectively.*

The reflection coefficients are related to the refractive indices and the angles of the incident and refracted rays by Fresnel equations:

$$r_s = \frac{N_1 \times \cos\varphi_1 - N_2 \times \cos\varphi_2}{N_1 \times \cos\varphi_1 + N_2 \times \cos\varphi_2}$$

$$r_p = \frac{N_2 \times \cos\varphi_1 - N_1 \times \cos\varphi_2}{N_2 \times \cos\varphi_1 + N_1 \times \cos\varphi_2}$$

Since the φ_2 is related with φ_1 by Snell–Descartes law, the reflection coefficients are defined only by φ_1, N_1 and N_2.

2.3.3. Substrate–film–air system

If a homogeneous layer of the thickness d_1 and refractive complex index N_1 is placed between two semi-infinite media: the ambient air (refractive index n_a) and the substrate (refractive complex index N_0), then the reflection coefficient is given as:

$$r = \frac{r_{12} + r_{10} \bullet \exp(2i\theta)}{1 + r_{21} \bullet r_{10} \bullet \exp(2i\theta)}$$

Here θ is the phase shift of multiple reflected wave passing through the boundaries 0-1 and 1-2 (Figure 25).

Figure 25. *Reflection and transmission of the incident wave of light in substrate–film–air system.*

The phase shift is related to the film thickness, its complex refractive index and the refraction angle:

$$\theta = \frac{2\pi}{\lambda} \bullet d_1 \bullet N_1 \bullet \sqrt{1 - \left(\frac{n_a \bullet \sin\varphi}{N_1}\right)^2}$$

2.2.3.4. Experimental setup

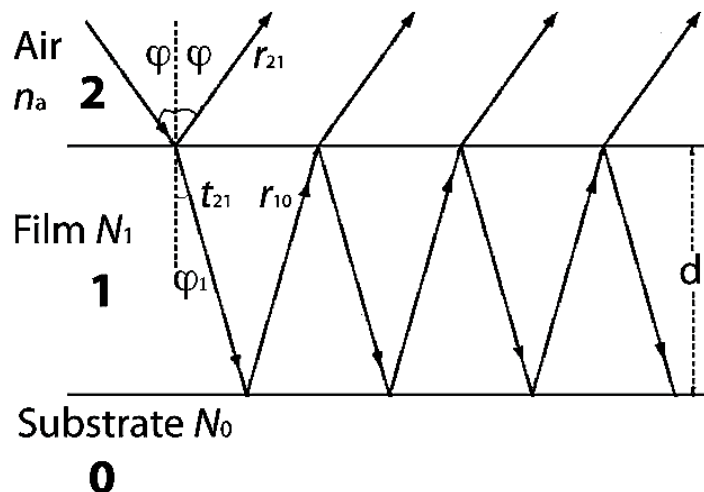In this work a single-wavelength ellipsometer (PLASMOS, SD2300) with a rotating analyzer was used for multilayer film thickness measurements and for monitoring the film growth (Figure 26).

While a wave generated by HeNe laser (light source) passes through polarizer (fixed at 45° with respect to the surface normal), it becomes linearly polarized. The linearly polarized light then passes through the wave compensator (quarter wave plate) where it is converted to the circularly polarized wave which falls onto the sample at a defined angle of 73° with respect to the surface normal. After the reflection from the sample surface, the elliptically polarized light reaches the rotating analyzer, which modulates the intensity of reflected light as a sinusoid function of time.

The intensity of the wave is registered by a photodetector mounted after the analyzer, and the signal is transmitted to the system computer for determination of the parameters Δ and ψ. Based on these values, the film thickness is finally calculated.

Since the evaluation of the refractive index of the film thinner than ~ 150 nm during the film deposition presents difficulties, it was assumed to be equal to that of silicon oxide (1.465). Although this assumption leads to slightly incorrect values with respect to the absolute film thickness, it allows the quick and precise determination of relative film thickness.
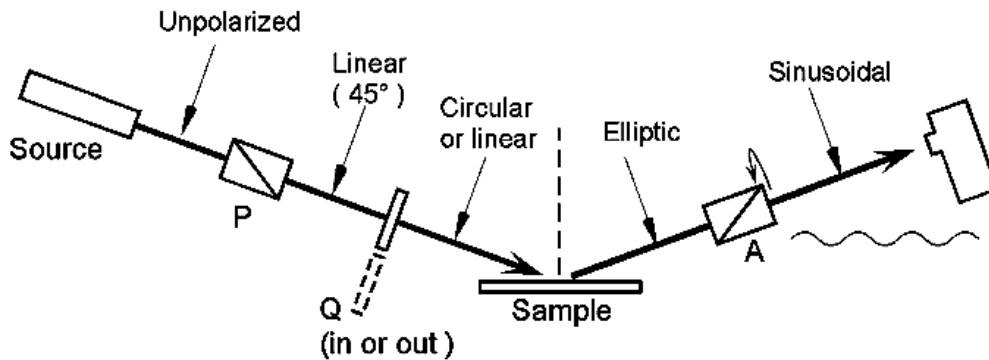
Figure 26. *Principal setup of single wave ellipsometer with rotating analyzer. The polarizer, the quarter wave plate and the rotating analyzer are assigned as P, Q and A, respectively.*

2.2.4. Quartz Crystal Microbalance with enhanced dissipation (QCM-D)

2.2.4.1. Piezoelectricity and piezoelectric materials

The quartz crystal microbalance technique relies on the phenomenon of piezoelectricity, first reported by Curie brothers in 1880 and representing the coupling of the electrical and mechanical properties of the material.

The phenomenon of piezoelectricity is based on the non-symmetric rearrangement of the charges in the lattice of the material without symmetric center upon mechanical deformation. The direct piezoelectric effect is observed when such charge redistribution generates a net charge on the face of the unit cell. The piezoelectric effect is called reverse if the voltage applied over the faces of the unit cell results in mechanical deformation of the lattice (*95*).

Due to its piezoelectric properties, quartz is one of the most frequently used materials for resonator applications. In the QCM-D experimental setup a polished, AT-cut, quartz crystals are used. These crystals operate in thickness-

shear mode and are stable to the temperature changes. Quartz crystal microbalances (QCM) consist of a thin quartz disc sandwiched between a pair of electrodes made of gold. The oscillation of quartz crystal is defined by *active area* – the area where the electrodes overlaps (*96*).

2.2.4.2. Oscillation of quartz crystal at the resonance frequency

While the alternating voltage is applied, the piezoelectric crystal oscillates in the direction of applied potential. When the standing wave forms between the two faces, the oscillation at resonance frequency is given by:

$$f = \frac{n v_q}{2 t_q} = \frac{n v_q}{\lambda}$$

where t_q is the thickness of the crystal, λ is the wavelength of the standing wave and v_q is the speed of sound in the quartz crystal (3340 m/s), n is the overtone number.

According to the equation above, the deposition of molecules on the quartz crystal will decrease the frequency of oscillation. Assuming that the film possesses a solid-like rigidity, strongly attached to and evenly distributed on the crystal surface, the relation between the change in the frequency and the mass of the adsorbed layer per unit area is then defined by Sauerbrey equation (*97*):

$$\Delta m = -C \bullet \Delta f$$

where C is the mass sensitivity and is given as:

$$C = \frac{t_q \rho_q}{f}$$

where ρ_q is the quartz density. For the quartz crystals with fundamental frequency of 5 MHz used in this work $C=17.7$ ng/(cm^2*Hz).

Although the Sauerbrey equation is employed for monitoring layer deposition in the gas phase and vacuum environment if the mass of adhered film do not exceed 2% of the crystal mass, it was also shown to be valid at the solid-liquid interface (*98*).

2.2.4.3. Energy dissipation kinetics

When the formation of the film takes place in the liquid environment, the oscillation frequency of the crystal is different from that in the vacuum and depends on the liquid properties such as density ρ and viscosity η as (*98*):

$$\Delta f = f_0 \sqrt[3/2]{\frac{\eta \rho}{\pi \mu_q \rho_q}}$$

where μ_q the elastic shear modulus of the quartz crystal.

In this case the mass of the film cannot be precisely defined by Sauerbrey equation, since the adsorbed layer contains liquid. Moreover, it is not rigidly attached to the sensor surface and can slip on the oscillating surface of electrode.

Information about viscoelastic properties of the layer and the mass uptake can be obtained by monitoring the dissipative energy losses in the oscillating system during the layer formation.

The energy dissipation (D) is inversely proportional to the decay time τ after an excitation of the crystal as follows (*99*):

$$D = \frac{1}{\pi f \tau}$$

The decay time of the oscillator is defined as the time required for initial oscillation to decay by the factor of 1/e.

When the crystal is excited to the resonance frequency and the driven power is switched off, the current *I(t)* carried through the crystal is measured. The changes in the current *I(t)* are related to the decay time as follow (*100*):

$$I = I_0 e^{-t/\tau} \sin(2\pi f + \Phi)$$

where I_0 is the current intensity when the drive voltage is switched off and *Φ* is the phase.

D-shifts caused by layer deposition onto the sensor surface depend on the viscoelastic properties of the layer. For thick layers, when $t_{film}/\delta \gg 1$, the energy dissipation is a function of film density, film elastic shear modulus and film viscosity (*100*). The penetration depth *δ* of the shear wave induced by the crystal oscillating in liquid is defined by the liquid viscosity and density (*98*):

$$\delta = \sqrt{\frac{2\eta}{\omega\rho}}$$

and depends on the oscillation frequency as:

$$\delta = 1 \Big/ \sqrt{n}$$

where n is the overtone number.

For the viscous limit (μ→0) the frequency shift is defined as:

$$\Delta f \approx \frac{1}{2\pi \rho_q t_q} \sqrt{\frac{\rho_{film} \eta_{film} \omega}{2}}$$

And the drift in the energy dissipation in the liquid is given by:

$$\Delta D \approx \frac{1}{2\rho_q t_q} \sqrt{\frac{2\rho_{film} \eta_{film}}{\omega}}$$

The energy dissipation can be registered in the real time simultaneously with frequency changes providing the information about the mass loading and structural changes of the molecules on the surface.

2.2.4.4. E4 QCM-D experimental setup

In the present studies a Q-sense E4 system (QE401 Qsense AB, Göteborg, Sweden) equipped with four flow modules was used for monitoring LbL deposition process and cytoskeleton changes upon the exposure of cell culture

to polyplex solution. Each flow module is designed to carry polished AT-cut sensor crystal (diameter 14 mm) with fundamental frequency 5 MHz. The volume of the flow module above the sensor is 40 µL.

The best mass sensitivity of the instrument in the liquid is 0.5 ng/cm^2 in the single frequency mode.

All measurements were performed at several odd multiples of the fundamental frequency (up to 13th overtone) and frequency shifts were normalized to the overtone number.

2.2.5. Flow cytometry (*101, 102*)

Flow cytometry is an analytical technique used to measure physical and chemical characteristics of an individual cells as they pass through the light beam. Based on these measurements the particles of interest or living cells can be retrieved by flow sorting from a heterogeneous population.

2.2.5.1. General principle

To resolve certain cell population by flow cytometry, the sample should contain monodisperse suspension of cells.
A flow cytometer consists of three main parts: a fluidics system, which transports the sample to the laser beam; an optical system consisting of lasers, optical filters and detectors, and an electronics unit (Figure 27).
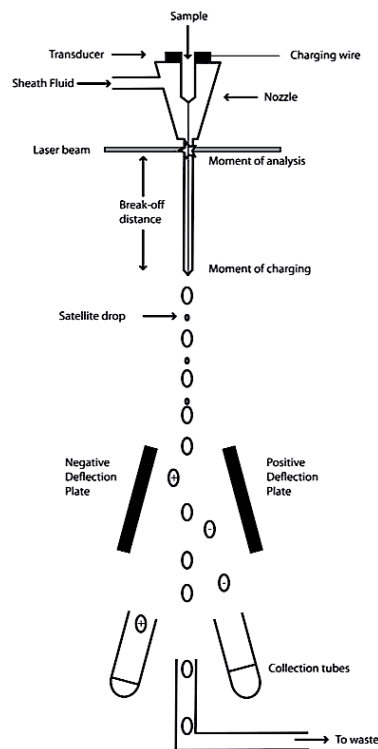
Figure 27. *Schematic of cell sorting by flow cytometer.*

In the cytometer, the sample flows close to the transducer – a piezoelectric crystal, which oscillates at certain frequency and breaks up the fluid stream into the droplets of defined size. When the droplets passed through the flow cell or the nozzle, they are transported by the stream of sheath liquid to the laser beam. For optimal data acquisition the stream should be hydrodynamically focused in the center of the laser beam.

While going one by one through the laser beam, cells scatter the laser light. The characteristics of scattered light depend on the cell shape and size, surface topology and internal cell complexity.

When fluorescently labeled cells pass through the beam of light of appropriate wavelength the fluorescent molecules are excited. Upon the relaxation to their ground state the molecules emit photons (fluoresce).

The scattered and fluorescent light is collected by lenses and is directed to the detectors by the system of optical filters and splitters. The retrieved signal is transported to the electronic unit and then to the computer.

Once the target cell population is identified it can be retrieved from the sample by individually charging the drops containing the cells of interest. Then the charged drops pass between two high-voltage charged plates, they are deflected according to their charge to the collection tubes as shown in the Figure 27.

In this work, the transfection efficiency and the viability of the cells were analyzed with FACSCalibur instrument (BD Biosciences, USA) equipped with a blue laser operating at 488 nm and of an air cooled argon-ion laser of 635 nm.

2.2.6. Contact angle measurements (*103*)

2.2.6.1. Young's equation

The deposition of a small non-volatile drop onto a homogeneous flat solid surface leads to the formation of three phases: liquid (L), solid (S) and equilibrium vapor (V). Each interface is characterized by the free energy per unit area: γ_{SV}, γ_{SL}, γ_{LV} (Figure 28).

The shape of the droplet is defined by the balance between adhesive forces acting on the molecules in the different phases and the cohesive forces influencing molecules of the same phase.
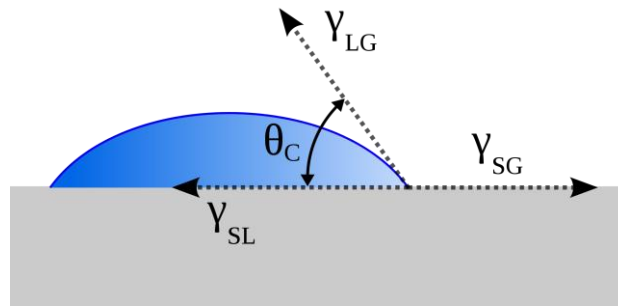
Figure 28. *Schematic of a drop deposited on the flat solid surface (104).*

In equilibrium the net force per unit length acting along the boundary line between the three phases is defined by Young's equation:

$$\cos\theta = \frac{\gamma_{SV} - \gamma_{SL}}{\gamma_{LV}}$$

Since the value of the contact angle is entirely defined by interfacial energies, it therefore characterizes the wetting properties of the surface. For the contact angle less than 90° (thus $\gamma_{SV} > \gamma_{SL}$), the drop of the liquid will spread on the surface. By the contrast if the contact angle is bigger than 90°, the wetting of the surface is unfavorable and the fluid will form a compact liquid droplets.

2.7. Experimental procedures

2.7.1. Preparation of polyelectrolyte solutions

All reagents were used as received without any additional purification steps. The solutions of poly(allylamine hydrochloride) (PAH), poly(diallyldimethylammonium chloride) (PDDA), dextran sulfate sodium salt (DexS), alginic acid sodium salt (Alg) and poly(sodium 4-styrenesulfonate) (PSS), poly(*L*-lysine), poly(*L*-ornithine), poly(*L*-glutamic acid) and hexametaphosphate were prepared in 0.15 M sodium chloride solution at the concentration of 1 mg/ml.

The solution of branched poly(ethylenimine) (PEI) was prepared at concentration 2.5 mg/ml in 0.15 M NaCl solution.

Chitosan was dissolved in the solution of 2% (v/v) of acetic acid in 0.15M NaCl to obtain a final concentration of 1 mg/ml (pH=4). Prior to the experiments the solution of chitosan was filtered with filter paper (retention capacity 4 – 12 µm) to remove the insoluble gel particles.

The solutions of linear poly(ethylenimine) (lPEI) and DNA were prepared at different concentrations in 0.15 M of NaCl filtered with 0.22-µm filter before use.

2.7.2. Cleaning procedures for the substrates

The silicon wafers and the quartz slides were rinsed with ethanol and Milli-Q water, dried with compressed air and treated with oxygen plasma in the plasma cleaner (PDC-002, Harrick Plasma, NY) for 3 min.

The QCM-D sensors were rinsed with Milli-Q water, dried with compressed air and treated with UV-ozone in Uv-ozone cleaner (UV/Ozone ProCleaner™, BioForce Nanosciences, Inc., Iowa) for 20 min.

The glass slides were cleaned with 2% Hellmanex® III (Hellma GmbH & Co, France) in an ultrasound bath for 15 min followed by rinsing by distilled water for 10 min in ultrasound bath. Finally, each glass slide was extensively rinsed with Milli-Q water, dried with compressed air and treated with oxygen plasma in the plasma cleaner (PDC-002, Harrick Plasma, NY) for 3 min.

2.7.3. Polyplex preparation

2.7.3.1. Transfection experiments

IPEI/DNA complexes were prepared by mixing of IPEI and DNA solutions in 0.15M NaCl prepared at corresponding concentrations (Table 1). 50 µL of IPEI solution in 0.15 M NaCl was added to 50 µL of DNA solution in 0.15 M NaCl, and the resulting mixture was gently vortexed. After 20 min of incubation time at room temperature the polyplexes were added to the CPRE2 cells (see 2.7.6).

C(DNA), mM	C(IPEI), mM	N/P
0.06	0.3	5
0.04	0.3	7.5
0.02	0.3	15
0.01	0.3	30

Table 1. *The concentrations of linear PEI and DNA in 0.15 M NaCl used for polyplex preparation in transfection experiments.*

2.7.3.2. Dynamic Light Scattering measurements

The estimated diameter of the polyplexes was determined at 25°C. For DLS size measurements, 200 µL of corresponding IPEI solution in 0.15 M NaCl were

added to 200 μL of DNA solution (Table 2). The mixture was vortexed. After 20 min the sample was placed in quartz cuvette and diluted with 600 μL of 0.15 M NaCl.

N/P ratio	C(DNA), mM	C(lPEI), mM
2.5	0.01	0.025
5	0.01	0.05
7.5	0.01	0.075
15	0.01	0.15
30	0.01	0.3
2.5	0.03	0.075
5	0.03	0.15
7.5	0.03	0.225
15	0.03	0.45
30	0.03	0.9
2.5	0.04	0.1
5	0.04	0.2
7.5	0.04	0.3
15	0.04	0.6
30	0.04	1.2
2.5	0.06	0.15
5	0.06	0.3
7.5	0.06	0.45
15	0.06	0.9
30	0.06	1.8

Table 2. *The concentrations of linear PEI and DNA in 0.15 M NaCl used for polyplex preparation.*

2.7.3.3. ζ-potential measurements

The ζ-potential of polyplexes was measured at 25°C. The polyplexes were prepared according to the protocol used for transfection. After 20 min of incubation at room temperature the sample was diluted with Milli-Q water up to 1 ml and transferred into the measuring cell. The concentrations of DNA and lPEI used for polyplex preparation are presented in Table 2.

2.7.4. Nanobags preparation

2.7.4.1. Transfection experiments

10 µL of a solution sodium citrate at various concentrations (Table 3) in 0.15 M NaCl solution prepared were added to 50 µL of DNA solution (0.06 mM or 0.03 mM in 0.15 M NaCl). After the mixture was gently vortexed, lPEI at concentration 0.3 mM was added to the citrate/DNA mixture. The resulting three-component system was gently vortexed and after 20 min of incubation time the formed nanobags were added to the CPRE2 cells (see 2.7.7.).

2.7.4.2. Dynamic Light Scattering measurements

40 µL of a solution sodium citrate in 0.15M NaCl solution prepared at different concentrations were added to 200 µL of DNA solution (0.06 mM or 0.03 mM in 0.15M NaCl). After the mixture was gently vortexed, lPEI at the concentration 0.3 mM was added to the citrate/DNA mixture. The resulting three-component system was gently vortexed and after 20 min of incubation time the sample was placed in a quartz cuvette and diluted with 600 µL of 0.15M NaCl.

Concentration of initial trisodium citrate solution, mM	Concentration of carboxylic groups in the reaction mixture, mM	v(-COOH) in the reaction mixture, nmol
0	0	0
3.3	1.1	100
17	5	500
33	10	1000
50	15	1500
67	20	2000
83	25	2500
100	30	3000
116	35	3500
133	40	4000

Table 3. *Concentration of trisodium citrate solutions used for nanobag preparation and final concentration of carboxylic groups in the reaction mixture.*

2.7.4.2. Dynamic Light Scattering measurements

40 µL of a solution sodium citrate in 0.15M NaCl solution prepared at different concentrations were added to 200 µL of DNA solution (0.06 mM or 0.03 mM in 0.15M NaCl). After the mixture was gently vortexed, lPEI at the concentration 0.3 mM was added to the citrate/DNA mixture. The resulting three-component system was gently vortexed and after 20 min of incubation time the sample was placed in a quartz cuvette and diluted with 600 µL of 0.15M NaCl.

2.7.4.3. ζ-potential measurements

The ζ-potential of nanobags was measured at 25°C. The nanobags were prepared according to the protocol used for transfection (section 2.7.4.1). After

20 min of incubation the sample was diluted with Milli-Q water up to 1 ml and transferred into measuring cell.

2.7.5. Transmission electron microscopy (TEM) studies

The samples were analyzed with TEM operating at 120 kV (Philips CM12) equipped with a Megaview III Soft Imaging System camera.

lPEI/DNA complexes or nanobags were prepared according to the protocol used for transfection (see section 2.7.3.1.). For TEM grid preparation, 5 µL of polyplex solution were placed on 400 mesh carbon-coated copper grids. After 2 min of deposition, the solution was removed with filter paper and the sample was treated with staining solution of an uranyl acetate solution (2 wt % in water) for 1 min and then dried with filter paper.

2.7.6. Cell culture

CPRE2 cell line, primary adult human dermal fibroblasts, was established from an abdominoplasty of a 38-year-old woman suffering from obesity. Briefly, the tissue was treated mechanically to remove hypoderm (especially adipose tissue) and then treated with enzymes to remove the epidermal part. Then, dermal fibroblasts were selected upon cultivation.

The cells were maintained at 37°C under 5% CO_2 atmosphere in Dulbecco's modified Eagle's medium supplemented with 10% (v/v) fetal bovine serum (FBS).

2.7.7. Transfection experiments

Cells were seeded in 12-well cell culture plate (Costar, Corning, NY) at a density 10 000 cells/well. After 24 hours the culture medium was changed and

100 µL of polyplexes were added to each well containing cells. The expression of green fluorescent protein (GFP) was analyzed 48h after transfection by flow cytometry. Data were collected from 10 000-30 000 events for each sample. All experiments were performed in triplicate.

2.7.8. Layer-by-Layer deposition

Multilayer films were constructed by spray-assisted LbL assembly using AIRBOY bottles against vertically mounted substrates. Time for polyelectrolyte deposition and rinsing steps was 5 sec. With exception of films made of poly(L-lysine) or poly(L-ornithine) and poly(L-glutamic acid), LbL deposition was always started with spraying PEI solution onto a cleaned substrate pretreated with oxygen plasma. When the substrate was rinsed twice by the solution of 0.15 M NaCl to remove weakly adsorbed polyelectrolyte, the solution of the corresponding polyanion was sprayed onto it. After the rinsing steps the layer of polycation was deposited on the substrate surface. The rinsing procedure was used to complete the construction of the first layer pair.

This process was repeated until the desirable number of layers was assembled. Different types of films were prepared for their further investigations. For ellipsometry and contact angle measurements the rinsing procedure was carried out with Milli-Q water. The estimate of the ellipsometric layer thickness was always the average of 10 measurements performed over an area of 1 cm^2. The mean layer thickness was obtained after the measurements of three different samples. The error bars correspond to the standard deviation of the film mean thickness.

2.7.9. Cell seeding onto LbL films and viability studies

For cell adhesion experiments, LbL films were assembled on the glass cover slips according to the procedure described in 2.7.8. For evaluation of the effects

of the films properties on the cell survival and proliferation, the coated substrates were transferred into cell culture plate and CPRE2 cells were seeded on the top of multilayers at density of 10 000 cells/well in the cell growth medium as shown in the Figure 29. The images of cell density, morphology and spreading were captured with Leica inverted microscope over 96h. were detached by the treatment with trypsin and the cell viability was analyzed by flow cytometry using TOPRO$^{®}$ - 3 staining assay. Data were collected from 30 000 - 50 000 events for each sample.The cells grown on the uncoated glass slides and on the gelatin-covered wells were used as references.
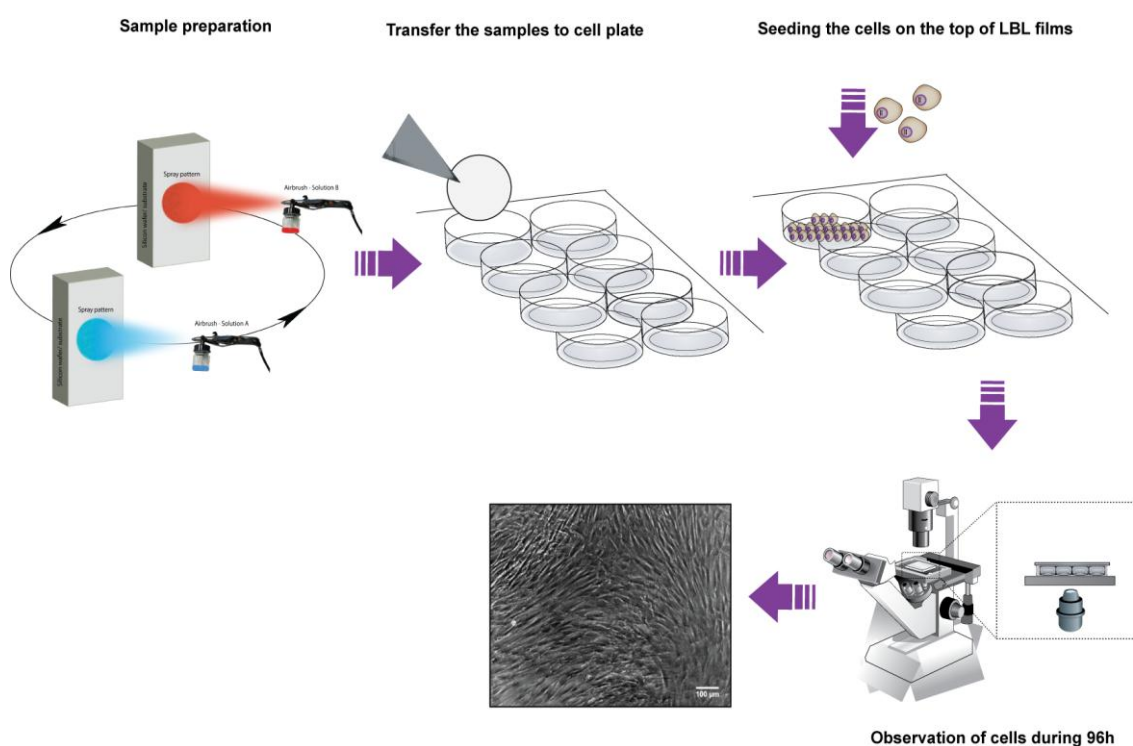

Figure 29. *Schematic representation of the experiment on the cytocompatibility and cell adhesion properties of LbL-functionalized substrates.*

2.7.10. Layer-by-Layer deposition on QCM-D crystals

The films were deposited *in situ* in QCM-D chamber. Prior to the measurements the crystals were rinsed with Milli-Q water, and then exposed to UV-ozone for 15 min.

The experiments were performed at room temperature in the flow mode (300 µL/min). After the crystal sensor was equilibrated in 0.15 M NaCl, a solution of PEI was injected into the chamber to form the first layer. When the frequency and dissipation curves were stabilized, the surface of the crystal was rinsed with 0.15 M NaCl to remove weakly adsorbed polyelectrolyte macromolecules. Each subsequent layer was deposited according to the procedure described above until the desired number of layers was obtained.

After layer assembly was completed, the QCM-D chamber was equilibrated to 37°C. The cell medium supplemented with 10% of fetal bovine serum was injected in the chamber. The stability of the LbL film at the conditions used for cell culture was evaluated during 96h after medium injection.

2.7.11. QCM-D transfection studies

The QCM-D crystals were rinsed with Milli-Q water and exposed to UV-ozone for 15 min and then covered with PEI(PSS/PAH)$_5$ multilayers according to the procedure described above (2.7.7.).

24h after the cells were seeded onto the surface of the sensor *ex situ*, the sensor was mounted in the QCM-D modules equilibrated to 37°C. The cell medium was injected to the QCM-D chamber. When the baselines were stabilized, the polyplexes prepared according to the procedure described in the section 2.7.3.1 in the cell medium (50/50% v/v) were introduced into the chamber at 50 µL/min.

3. Results and Discussion

3.1. Interactions of primary cells with LbL-coated substrates

The biocompatibility of a material is governed by cell-material interactions which depend on chemical composition of the surface, surface topology, wettability and elasticity of the surface (*105*).

Layer-by-Layer assembly is one of the rare tools allowing to control these parameters independently and without changing mechanical properties of the initial materials (*14*).

Due to the complexity and the diversity of extracellular matrix (ECM) (*76*) there is a demand for the development model chemically well defined substrates for studying cell-ECM interactions (*106, 107*). Currently, the ongoing research refers to in reveal the role of different macromolecules in cell adhesion, survival, development and proliferation processes (*108*) and therefore to improve the methodology for the development of advanced implantable and compatible materials for biotechnology and tissue engineering (*109*).

Due to its simplicity, robustness, versatility and ability for immobilization of various biological molecules without sacrificing their biological activity, LbL assembly offers an excellent platform for development of advanced nanostructured materials for biocatalysis, tissue engineering, drug delivery etc (*16, 17, 110*).

In this thesis work we focused on the influence of the properties of LbL-films such as chemical composition, wettability and roughness on the survival, attachment and proliferation of CPRE2 cells.

3.1.1. Construction of LbL films on the model surfaces

Multilayer films were constructed by spray-assisted method using AIRBOY bottles according to the procedure described in 2.7.7. The time for polyelectrolytes deposition and rinsing step was maintained 5 sec.

In all experiments the branched PEI was deposited as a first layer to ensure the subsequent uniform growth of the film.

The multilayer films were assembled via electrostatic interactions between oppositely charged polyelectrolytes: poly(allylamine chloride) (PAH), poly(diallyldimethylammonium chloride) (PDDA), chitosan (CH), dextran sulfate (DexS), sodium alginate (Alg), and poly(4-styrenesulfonate) (PSS).

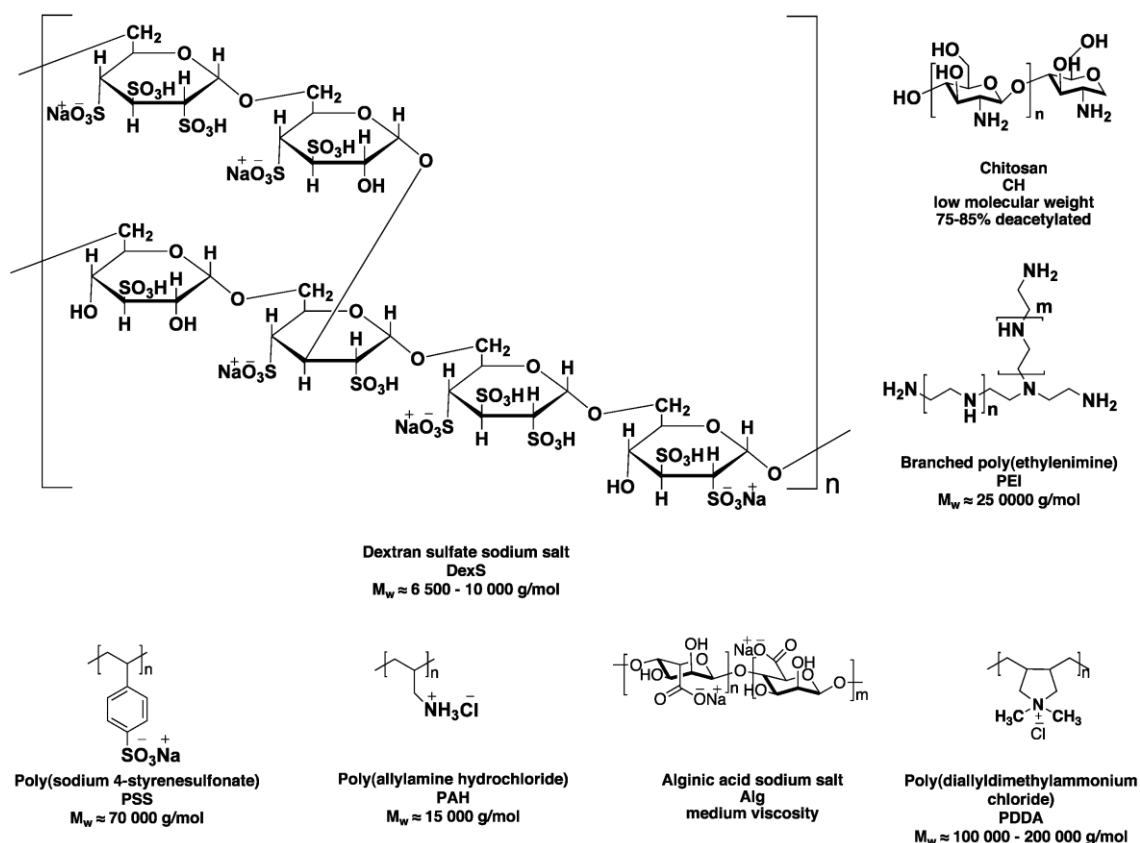The structures of these polymers are shown in Figure 30.

Figure 30. *Structures of polyelectrolytes used for LBL assembly.*

Layer-by-Layer build up was controlled by ellipsometry. The increase of the film thickness was plotted as a function of the number of layer pairs.

The growth profiles for the films are shown in Figure 31. The measurements were performed after drying the substrate with the compressed air.
The thickness of the films increased gradually with the layer number and can be altered by varying the number of deposition cycles.
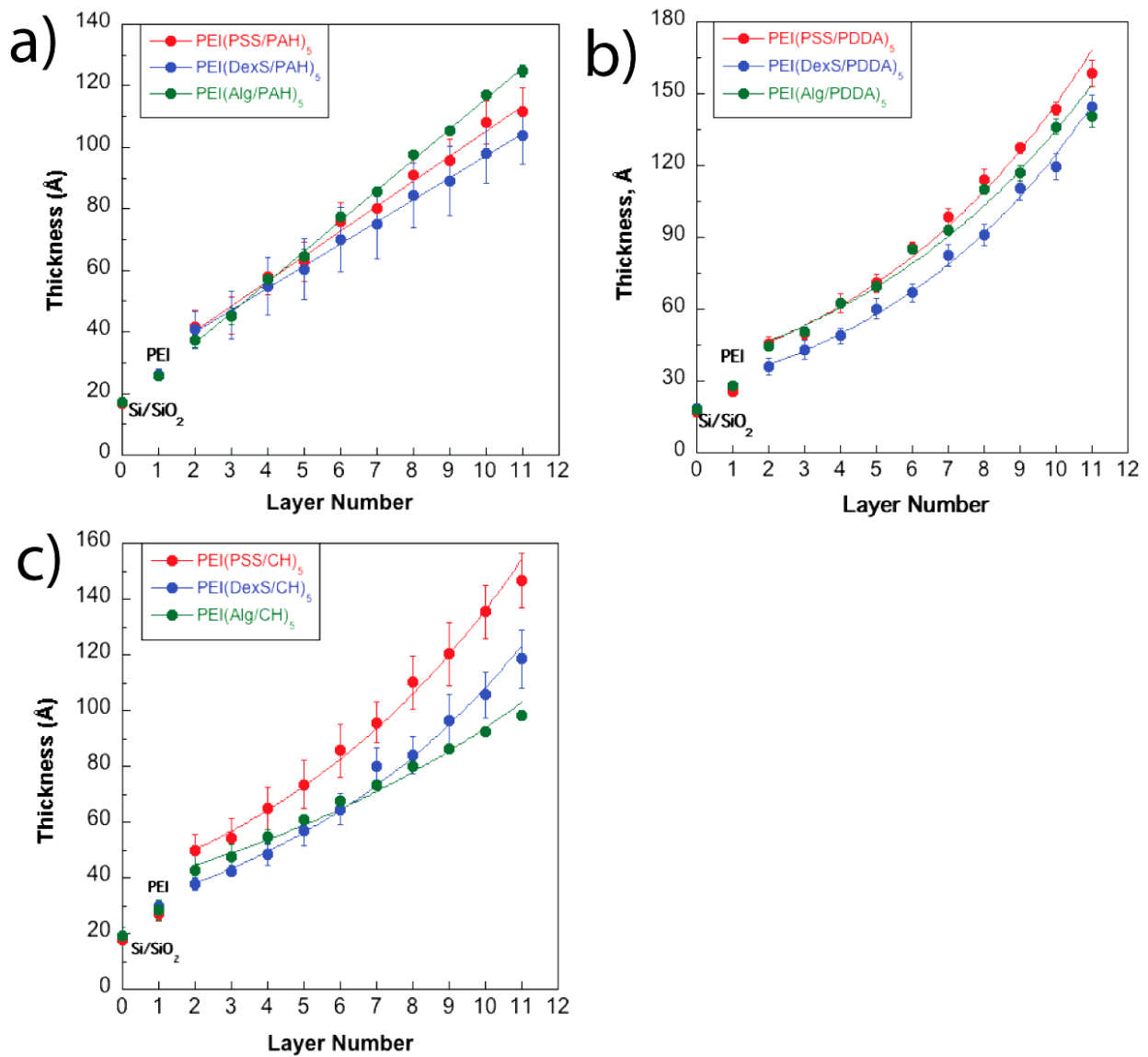

Figure 31. *The ellipsometric thickness of the LbL films as a function of deposited layers.*

The LbL systems containing PAH, that is PEI(PSS/PAH)$_5$, PEI(DexS/PAH)$_5$, PEI(Alg/PAH)$_5$, as well as PEI(Alg/CH)$_5$ showed linear growth with relative thickness 134 ± 4 Å, 115 ± 9 Å, 130 ± 5 Å and 98 ± 3 Å, respectively. The growth regime of the multilayer films based on PDDA and PEI(PSS/CH)$_5$, PEI(DexS/CH)$_5$ was found to be exponential at least for the first five layer pairs. The thickness of the films is presented in Table 4.

LbL system	Initial film thickness, Å
PEI(PSS/PAH)$_5$	112 ± 8
PEI(DexS/PAH)$_5$	104± 9
PEI(Alg/PAH)$_5$	125 ± 5
PEI(PSS/CH)$_5$	147 ± 10
PEI(DexS/CH)$_5$	119 ± 10
PEI(Alg/CH)$_5$	98 ± 3
PEI(PSS/PDDA)$_5$	158 ± 6
PEI(DexS/PDDA)$_5$	145 ± 5
PEI(Alg/PDDA)$_5$	141 ± 4

Table 4. *The ellipsometric thickness of LbL films.*

3.1.2. QCM-D monitoring

The built-up of the films was confirmed by QCM-D technique. The deposition of the multilayers was carried out on the gold surface of the QCM-D sensor. The raw data from the experiment are presented in Annex (Figures 1-9).

Figures 32-34 show the frequency shifts and energy dissipation during the film construction on the surface of QCM-D sensor for different polycation-polyanion combinations.

The decrease in the frequency signals (increase of -ΔF) during the assembly of the films made from PAH confirmed the linear character of multilayer growth (Figure 32a). However, the deposition of PEI(Alg/PAH)$_5$ film results in a much higher increase in the frequency signal per layer compared to PEI(PSS/PAH)$_5$ and PEI(DexS/PAH)$_5$.
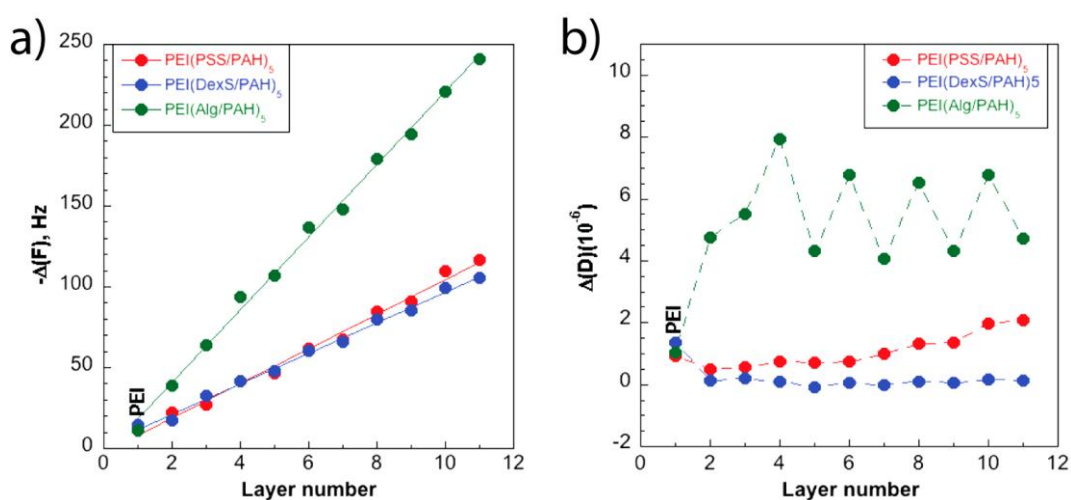

Figure 32. *The frequency and dissipation changes as the functions of layer number during the deposition of the films containing PAH. For the energy dissipation shifts during PEI(Alg/PAH)$_5$ buildup: odd integers correspond to the deposition of PAH, whereas even integers correspond to the polyanion deposition. Data are taken at the 7th overtone of the resonance frequency (5 MHz).*

The ΔD-curves as a function of layer number are shown in Figure 32b. During the assembly of PEI(DexS/PAH)$_5$ and PEI(PSS/PAH)$_5$ films, the energy dissipation undergoes only slight changes suggesting that the both types of systems form stiff layers. By the contrast, the dissipation of the PEI(Alg/PAH)$_5$

exhibits zigzag-like shifts, systematically increasing upon the adsorption of alginate and decreases to a lower extent upon the deposition of a PAH layer. Thus, typically the formation of each alginate layer results in a decrease in the frequency and an increase in the dissipation signal, while the deposition of PAH layers generates the decrease in the frequency and in the energy dissipation.

The final film contains water molecules that also contribute to the frequency shift values. The chemistry of the polyelectrolyte defines the water content in the film, which influences the viscoelastic properties of the layer and the dissipation response during the deposition process.

The ellipsometry studies of the $(PSS/PAH)_n$ film growth at low (3%) and high (99%) relative humidity revealed an "odd-even effect" in the swelling behavior of the multilayers during the LbL buildup ([111]). While in dry state the thickness of the film increases continuously with the number of layer, at high humidity an "odd-even effect" in the swelling behavior was observed with respect to the chemistry of outmost layer. The PSS-terminating layer swells in a more pronounced way (even layer number) than the film with PAH (odd layer number) as a top layer. Later, it was shown that the "odd-even effect" shifts to the "even-odd" effect at elevated temperatures ([112]).

Taking these data in account, the zigzag-like shape of QCM-D signals upon the formation of $PEI(Alg/PAH)_5$ layers could be attributed to the structural changes of the film, such as a compaction after PAH deposition and a re-swelling during the assembly of the next alginate layer.

As the film grows, only several outmost layers are affected by the formation of the next layer, while the core structure of the assembly remains stable, resulting in the decay of "odd-even effect".

Similar QCM-D responses were obtained for the layers containing PDDA (Figure 33). Besides the "odd-even effect" that was pronounced for all these LbL systems, the growth character of the films was different from that obtained by ellipsometry.
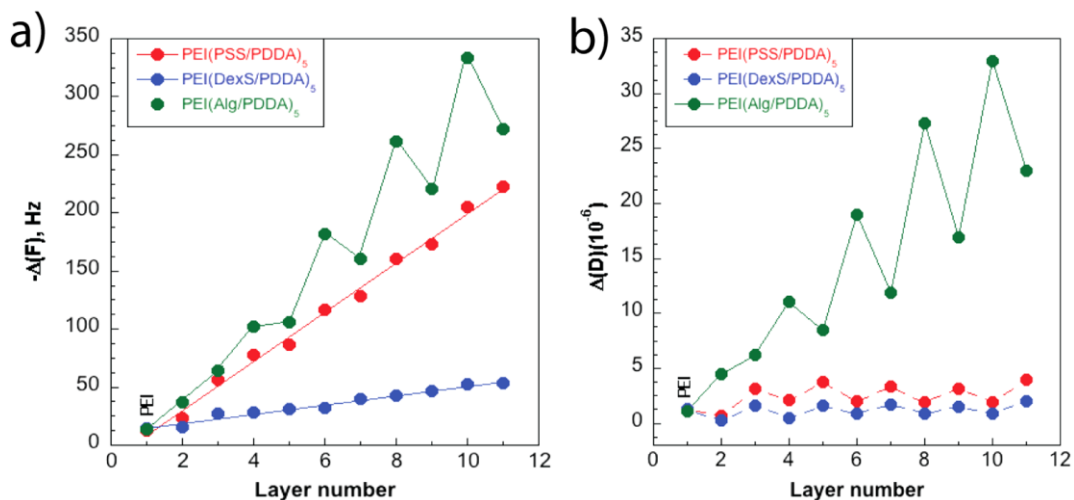
Figure 33. *The frequency and dissipation changes as the functions of layer number during the deposition of the films containing PDDA. Odd integers correspond to the deposition of polycation, whereas even integers correspond to the polyanion deposition. Data are taken at the 7th overtone of the resonance frequency (5 MHz).*

The studies on the properties of $(PSS/PDDA)_n$ layers by Guzman and colleagues suggested that due to the higher flexibility of PDDA chains compared to that of PSS, the increase in the dissipation factor upon the deposition of PDDA layer relates to the higher content of loops and tails protruding in the solution (*113*). After subsequent adsorption of PSS, a complexation between the chains of PSS and PDDA leads to the water release, subsequent film compaction and therefore to the decrease in the energy dissipation.

As shown in Figure 34, the PEI(Alg/CH)$_5$ film exhibits linear growth regime. For PEI(PSS/CH)$_5$ and PEI(DexS/CH)$_5$ the exponential growth become linear after three layer pairs.

For chitosan-based films, the rinsing with 0.15 M NaCl solution after the chitosan adsorption is typically accompanied by the slight increase in the frequency and decrease in the dissipation suggesting the partial desorption of the previously formed film (Figure 35).
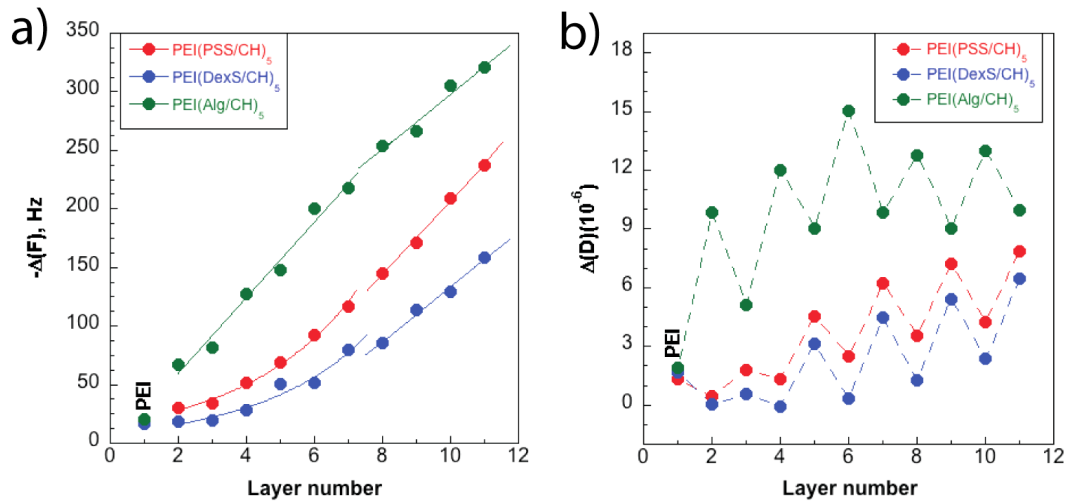

Figure 34. *The frequency and dissipation changes as the functions of layer number during the deposition of the films containing chitosan. odd integers correspond to the deposition of polycation, whereas even integers correspond to the polyanion deposition Data are taken at the 7th overtone of the resonance frequency (5 MHz).*
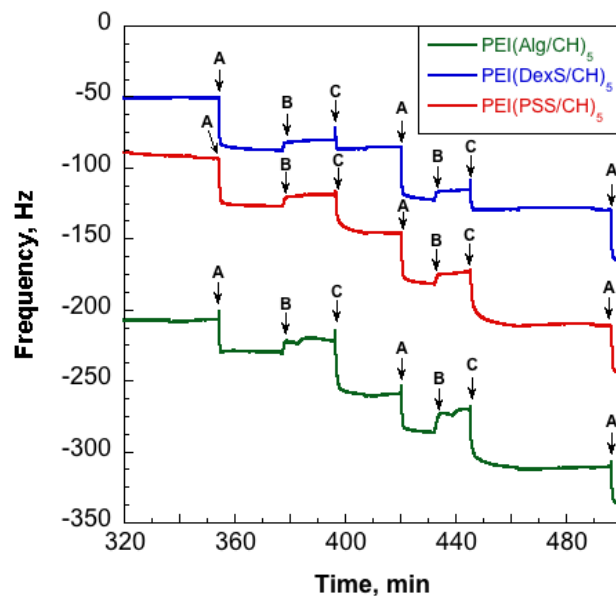
Figure 35. *The QCM-D frequency shifts during the deposition of chitosan layer (A), rinsing with 0.15 M NaCl (B) and the deposition of corresponding polyanion layer (PSS, DexS or Alg) (C).*

Based on the mechanism of $(CH/HA)_n$ film growth suggested be Richert and co-workers (*114*), the evolution of QCM-D signal can be explained in the following way.

Upon the formation of the polyanion layer (PSS, DexS or Alg) the corresponding polyelectrolyte interact with the outmost chitosan layer and then forms the complexes with chitosan chains that diffuse out of the film.

After the injection of chitosan solution, the chitosan interacts with polyanion layer and diffuses into the film. This interaction is accompanied by the re-dissolution phenomena of previously formed (CH/polyanion) complexes and only a part of them participate in the formation of the next layer. Therefore, the partial re-dissolution of the film upon the interaction with chitosan contributes to the "odd-even effect" in the frequency and dissipation signals.

Similar redissolution phenomena of LbL films was observed by Abdelkebir and co-workers during the assembly of biomimetic LbL films based on chondroitin

sulfate A (ChS) and PLL. The LbL buildup of was studied by different techniques including QCM-D, optical waveguide lightmode spectroscopy (OWLS), Fourier transform infrared spectroscopy (FTIR) and atomic force microscopy (AFM). While OWLS data revealed that the film grows linearly, the QCM-D and FTIR data suggested the exponential growth. Based on the data, the authors concluded that the film structure consists of two zones: the inner dense zone that grows linearly and outer diffuse zone with supralinear growth. The linear growth regime originates from the partial redissolution of initially formed polyelectrolyte complexes upon the formation of next polyelectrolyte layer. The transfer of such complexes in the diffusive zone contributes to its supralinear growth (*115*).

3.1.3. Cell adhesion

Unlike classic approach of gelatin-assisted cell adhesion, LbL assembly allows to engineer the film with specific properties in order to control the protein adhesion process (*116*), cell attachment, phenotype and cytoskeletal rearrangements on the surface (*27, 28, 117-119*).

The results obtained here revealed the drastic difference in the cell adhesion and proliferation properties of the multilayer coatings.
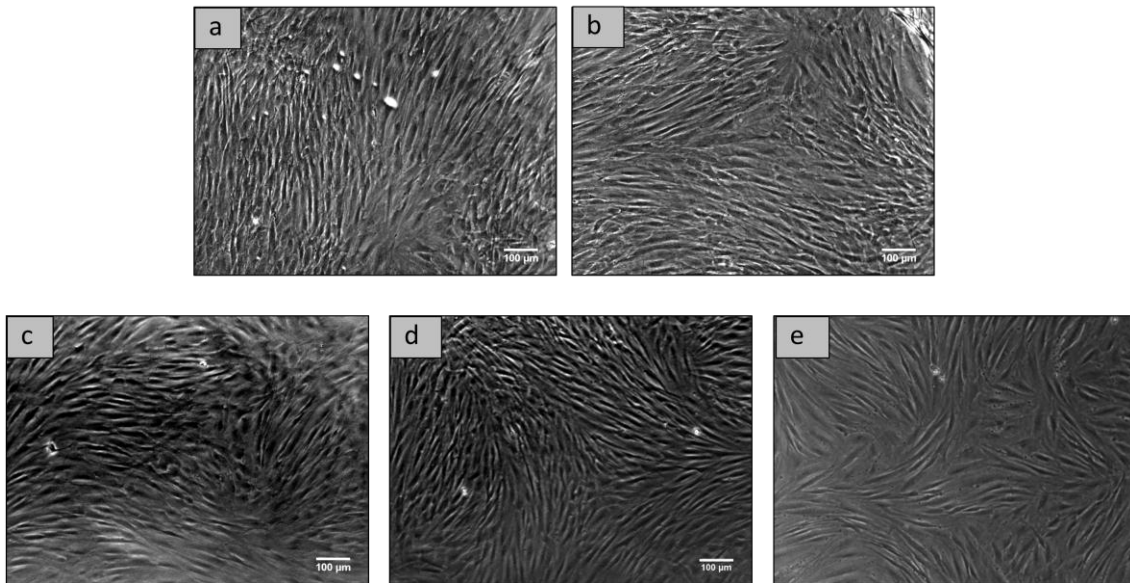
Figure 36. *The micrographs of CPRE2 cells seeded onto gelatin-coated plate well (a), glass slide (b), and glass slides coated with PEI(PSS/PAH)$_5$ (c), PEI(DexS/PAH)$_5$ (d) and PEI(Alg/PAH)$_5$ (e) films.*

Our data showed that the cells readily adhere onto the layers containing poly(allylamine). As shown on Figure 36, the best results were obtained with the PEI(PSS/PAH)$_5$ film. On this substrate the cell population was similar to that obtained with cells seeded onto the gelatin-coated surface. The multilayers containing PEI(DexS/PAH)$_5$ and PEI(Alg/PAH)$_5$ yielded lower cell densities compared to the reference coating. The cell viability data are presented in Table 5.

These results are in agreement with previous studies demonstrating that (PSS/PAH)$_n$-coated substrates favor cellular adhesion and proliferation.

Tryoen-Toth et al. studied the adhesion, viability and the phenotype stability for osteoblast-like cells and human periodontal ligament cells on PEI(PSS/PAH)$_2$ onto which different polyelectrolytes layers were deposited (*120*). The authors

proved that the PSS-ending layers support cell adhesion and were able to maintain osteoblasts viability and phenotype.

Recently, it was demonstrated that $(PSS/PAH)_n$ multilayers can be used for growing stem cell sheets while maintaining their phenotypic profile and differentiation potency (*121*).

The functionalization of titanium with $(PSS/PAH)_n$ and crosslinked $(HA/PLL)_n$ films to support human fibroblasts over seven days was studied by Brunot and co-workers (*122*). Although both film types demonstrated cell adhesive properties, $(PSS/PAH)_n$ films allowed better cell proliferation over seven days.

As it was mentioned in section 1.3.1, this type of films is applied for the engineering of vascular grafts since it improves the mechanical properties of the cryopreserved vessels and enhances the adhesion and spreading of endothelial cells on the vessels (*36*).

LbL film	Cell viability, %
Gelatin	90 ± 7
PEI(PSS/PAH)$_5$	87 ± 13
PEI(DexS/PAH)$_5$	80 ± 14
PEI(Alg/PAH)$_5$	68 ± 25

Table 5. *The viability of CPRE2 cell line 96h after seeding onto LbL films.*

By contrast, the incorporation of polysaccharides tends to decrease the cell adhesion and proliferation. Elbert and co-workers used $(Alg/PLL)_n$ film to create a barrier for the cell adhesion onto gelatin-coated polystyrene substrates (*22*). The human fibroblasts attachment decreased with the number of layer pairs, and the cell spreading was completely inhibited on $(Alg/PLL)_{15}$ coating. However, the re-seeding of the cells that were in contact with $(Alg/PLL)_{15}$ film

onto untreated tissue culture well led to the normal cell spreading suggesting that multilayers form bioinert coatings.

In another study, the interactions of the mouse fibroblasts cells with $(DexS/CH)_n$ films were analyzed by the expression of the heat-shock protein B70 that characterizes cell stress due to the contact with the material (*123*). It was shown that the percentage of round-shaped cells increases with the layer pair number and the greatest number of round-shaped cells was found on the multilayers terminating with DexS. The greater production of B70 protein was found in the cells attached to the film with DexS as outmost layer.

It was demonstrated that chitosan embedded into the film also reduces cell-surface interactions. Richert and colleagues studied the adhesion and spreading of primary chondrocytes onto $(CH/HA)_n$ multilayers (*124*). Although these cells possess the specific receptor to hyaluronan, the cell adhesion decreases with the number of layers. Similar results were obtained by Croll and co-workers on the adhesion and spreading of NIH-3T3 fibroblasts onto this type of layers (*125*).

Our results showed that the cells cultivated onto the layers with chitosan exhibit round morphology (Figure 37, a-c). Moreover, the observations of the cells during 24h revealed the absence of cell-substrate interactions. It should be mentioned that all the multilayers were carefully rinsed to assure final neutral pH of the films.

As shown in Figure 37 d-f, the exposure of the cells to the multilayers containing PDDA led to poor cellular adhesion and spreading, as it was observed by the changes in cell morphology, followed by complete cell detachment 48h after cell seeding.
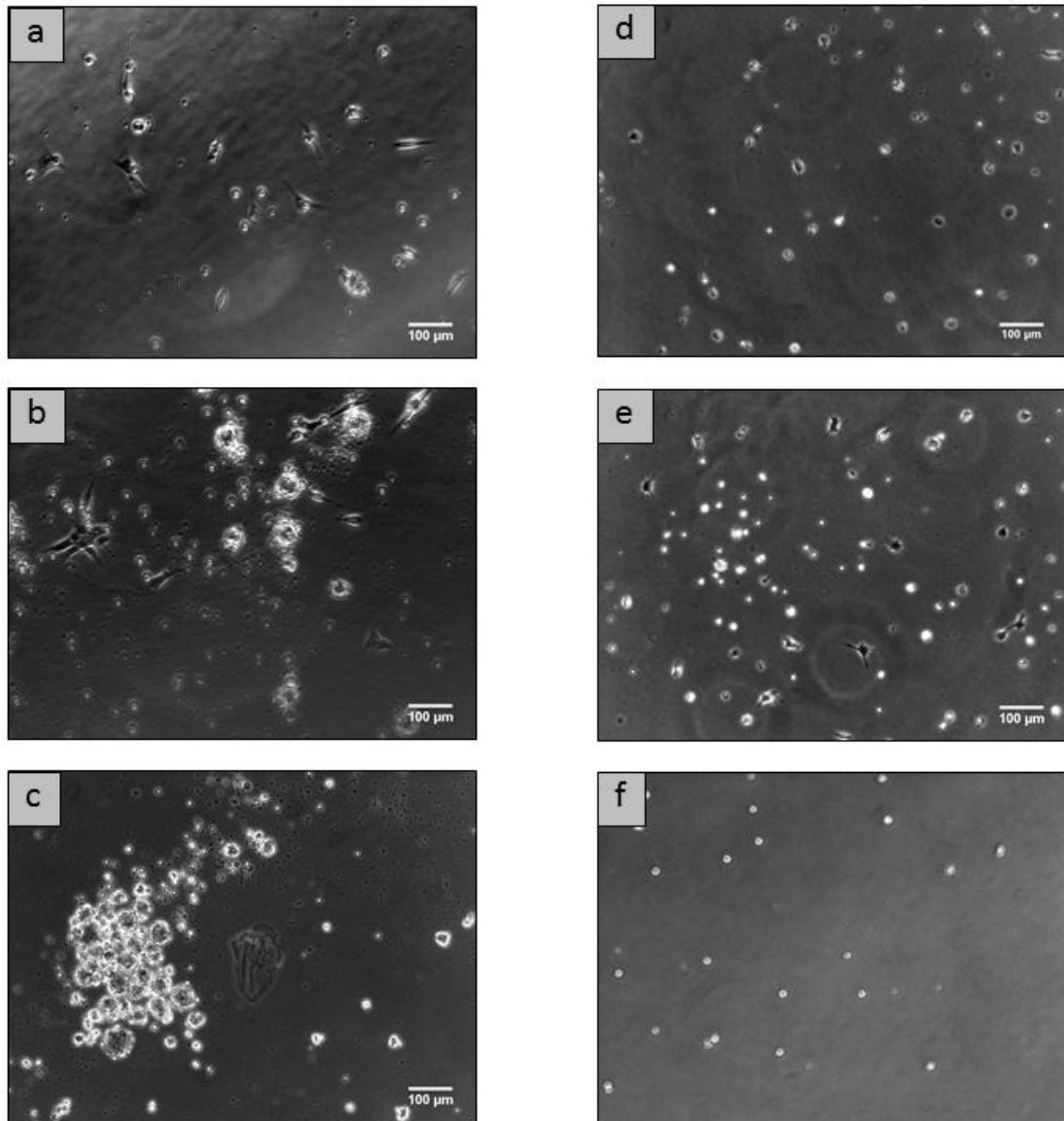
Figure 37. *The micrographs of CPRE2 cells seeded onto PEI(PSS/CH)₅ (a), PEI(DexS/CH)₅ (b), PEI(Alg/CH)₅ (c), PEI(PSS/PDDA)₅ (d), PEI(DexS/PDDA)₅ (e), PEI(Alg/PDDA)₅ (f) films.*

CPRE2 cells belong to the anchorage-dependent cell line and therefore for their growth *in vitro* they need to be attached to suitable solid surface. Thus, the detachment of this cell line from the substrate or its inability to attach to it normally leads to the cell death via apoptotic or necrotic pathways (*76*).

To evaluate the toxicity of the layers, the cells detached from LbL films were collected and reseeded onto gelatin-coated surface. It was expected that the viable cells would be still able to attach to the substrate supporting cell adhesion.

LbL film	Cell viability, %
Gelatin	90 ± 7
PEI(PSS/CH)$_5$	72 ± 28
PEI(Alg/CH)$_5$	87 ± 14
PEI(DexS/CH)$_5$	90 ± 7
PEI(Alg/PDDA)$_5$	84 ± 14

Table 6. *The viability of CPRE2 cells reseeded onto gelatin-coated surface after incubation with LbL films.*

The results showed that the cells, which previously were in the contact with PEI(PSS/CH)$_5$, PEI(DexS/CH)$_5$, PEI(Alg/CH)$_5$ and PEI(Alg/PDDA)$_5$ films, adhered and spread to gelatin-coated substrate. The cell viability data acquired 48h after cell transfer is presented in Table 6. By contrast, multilayers PEI(PSS/PDDA)$_5$ and PEI(DexS/PDDA)$_5$ were cytotoxic and the transferred cells were not able to attach to the gelatin substrate. It was somewhat unexpected result as it was demonstrated that other cells, human erythrocytes, readily interact with PDDA layers and maintain their viability (*126*).

Remarkably, the adhesion properties of the multilayers were found to be independent of the charge of the outmost layer. An exception represents the coating based on PEI(PSS/PDDA)$_5$/PSS, which facilitated cell attachment and spreading compared to the film bearing PDDA as the outmost layer (Figure 38).

Kidambi et al. obtained similar results for the primary rat hepatocytes in the serum-free medium. This cell line adheres preferentially on the substrate with PSS as a last layer in (PDDA/PSS)$_n$ film. The same cell response was observed for the films assembled with different poly(anetholesulfonic acids) or poly(vinylsulfonic acid) and PDDA. Authors suggested that the cells are attracted by the free sulfonic groups presented on the surface of the film (*127*).
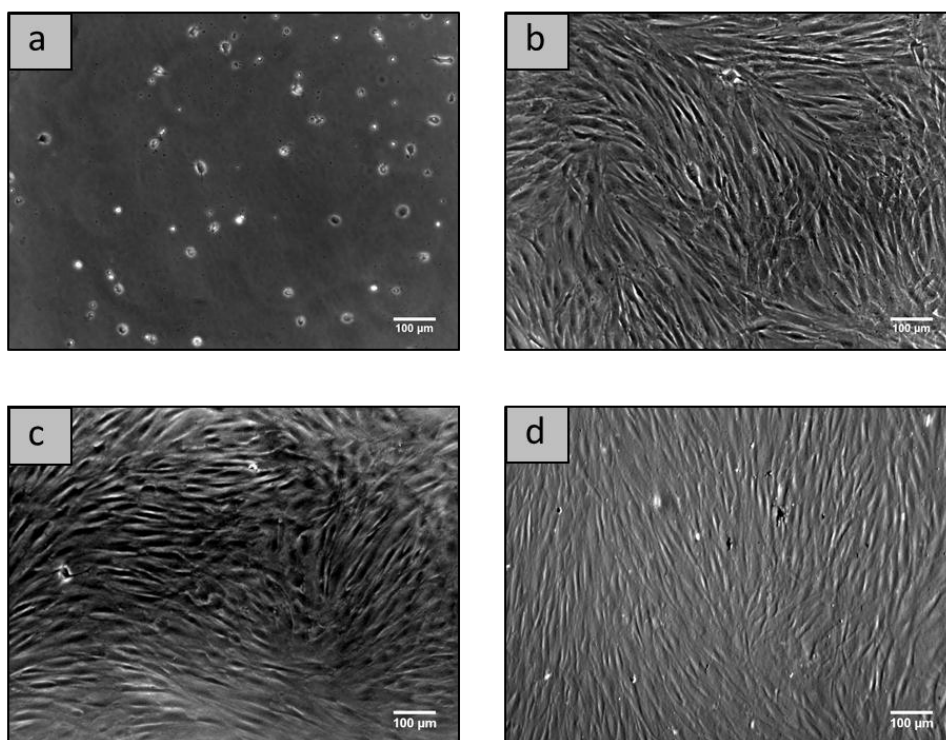

Figure 38. *The micrographs of CPRE2 cells seeded onto PEI(PSS/PDDA)$_5$ (a), PEI(PSS/PDDA)$_5$/PSS (b), PEI(PSS/PAH)$_5$ (c), PEI(PSS/PAH)$_5$/PSS films.*

Although, we did not observed this effect for the CPRE2 cells cultured on the PEI(DexS/PDDA)$_5$ and PEI(DexS/PDDA)$_5$/DexS films, the effect of top layer was found for the films made of PLGA and PLL or poly(ornithine) (PLO) (Figure 39).

As shown on the Figure 40a, the cell density on (PLL/PLGA)$_5$ layers was lower than on the gelatin-coated plate wells. These results agree with previous

studies of Picart and co-workers on the adhesion and proliferation of human osteoblasts on the (PLL/PLGA)$_6$ films (*119*).
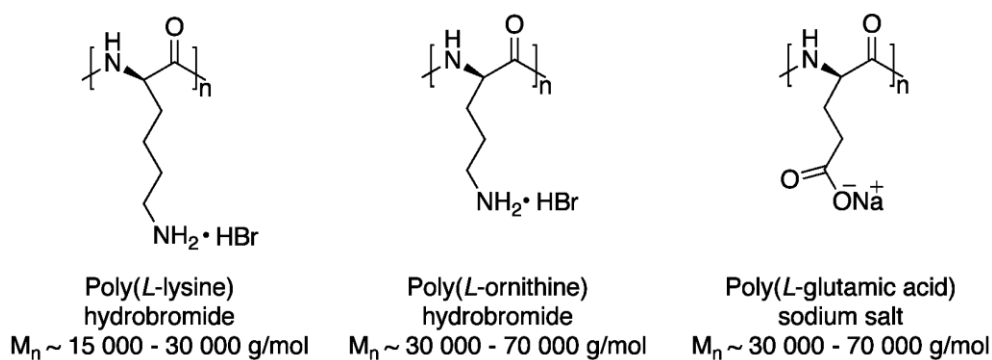

Figure 39. *The structures and characteristics of poly(L-lysine), poly(L-ornithine) and poly(L-glutamic acid) used for LbL assembly.*
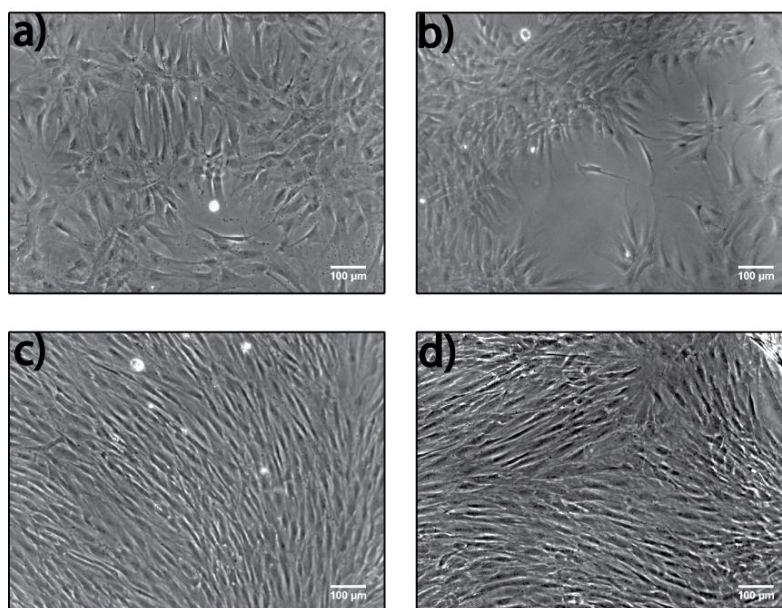

Figure 40. *CPRE2 cells seeded onto (PLL/PLGA)$_5$ (a), (PLL/PLGA)5/PLL (b), crosslinked (PLL/PLGA)$_5$/PLL (c) and on the gelatin coated well (d). The medium supplemented with 10% of FBS was used for cell culture.*

In this study, the cell adhesion and proliferation were inhibited onto native films, while the crosslinking with water soluble *N*-ethyl-*N'*-(3-dimethylaminopropyl)carbodiimide (EDC) in combination with *N*-hydroxysulfosuccinimide (sulfo-NHS) (Figure 41) led to dramatic improvement of cell attachment and enhanced cell proliferation. The authors suggested that such changes in the film cytocompatibility might be related to the enhanced film stiffness after crosslinking reaction.

Our results revealed that PLGA-terminating architecture was more attractive for the cell adhesion and proliferation compared to PLL-ended film (Figure 40, a and b). On the other hand, the (PLL/PLGA)$_5$/PLL layers crosslinked in the presence EDC/sulfo-NHS according to the procedure described in ref. (*119*) promote cell attachment and spreading as shown in Figure 40c.

1. Esterification reaction of polycarboxylic acid
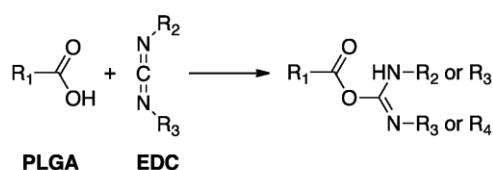
2. Transesterification reaction with sulfo-NHS
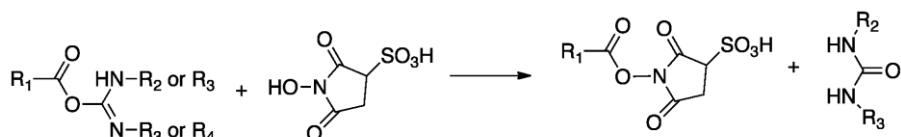
3. Nucleophilic Acyl Substitution
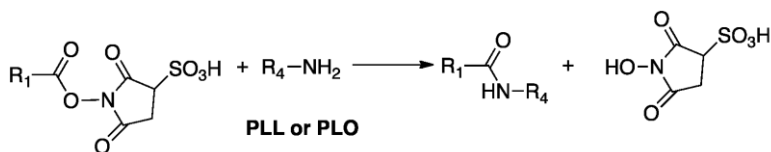
4. Regeneration of the carboxylic groups in PLGA
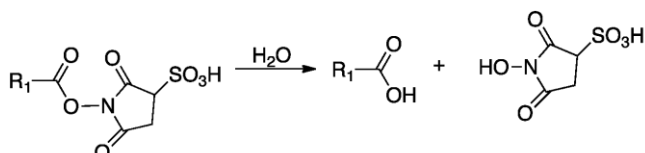
Figure 41. *Crosslinking reaction of carboxylic groups in PLGA with primary amino groups in PLL or PLO .*

Similar effect was observed for the substrate coated by the film made of PLGA and PLO. As shown in Figure 42, although the effect of the top layer was less pronounced, after the crosslinking of (PLO/PLGA)$_5$/PLO film, the cell proliferation increased and was comparable to that on the gelatin-coated plate wells.
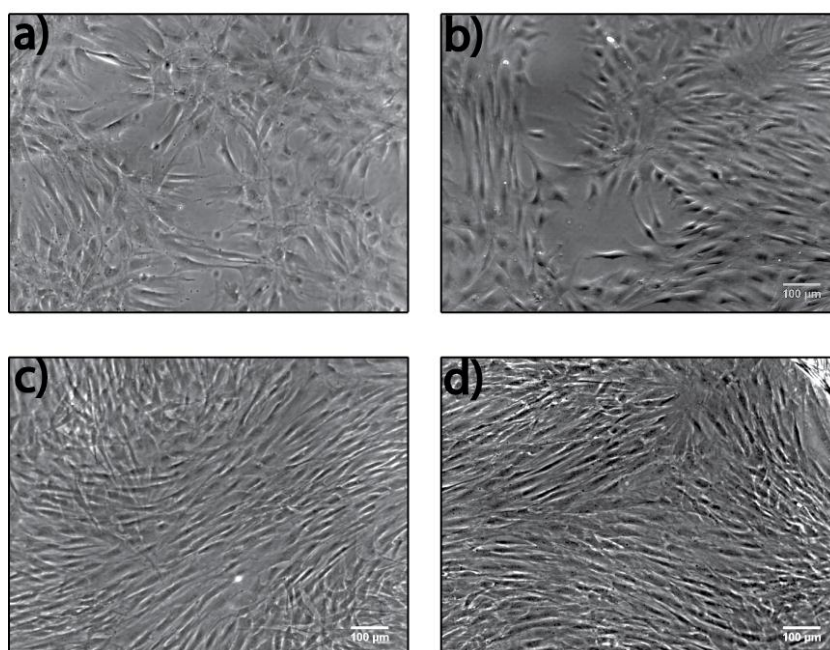
Figure 42. *CPRE2 cells seeded on (PLO/PLGA)$_5$ (a), (PLO/PLGA)5/PLO (b), crosslinked (PLO/PLGA)$_5$/PLO (c) and on the gelatin coated well (d). The medium supplemented with 10% of FBS was used for cell culture.*

3.1.4. Adsorption of proteins

It is generally thought that the cell-material interactions are mediated by a protein layer adsorbed from a complex protein mixture, e.g. serum, on the surface of the material (*108, 128-130*).

The protein-polyelectrolyte interactions are directed by van der Waals forces, hydrophobic and electrostatic interactions and the formation of hydrogen bonds between the specific moieties (*131*). Schwinté and co-workers studied the structural changes of bovine serum albumin and heg egg lyzozime upon their interactions with (PSS/PAH)$_n$ film. While the charge of terminating film layer was opposite to that of the protein, a large decrease of the α-helix and consequent increase in the intramolecular β-sheets content was observed. By contrast, the interaction of proteins with charge-like layer led to the lower protein adsorption. In this case the structure of the proteins remained similar to that in dilute solutions (*132*).

Upon the interactions with multilayers, the proteins molecules either form a top layer or diffuse into the film. The studies on the diffusion process of human serum albumin upon the interaction with (PSS/PAH)$_n$ film by using fluorescent recovery after photobleaching revealed that typically 50-70% of adsorbed protein molecules were able to diffuse laterally along the surface or in the film (*133*).

Salloum et al. found that the adsorption of proteins onto LbL substrate is driven mostly by the electrostatic interactions between the protein molecules and oppositely charged outmost polyelectrolyte layer. Moreover, the adsorption of the proteins occurs on the likewise-charged LbL surface and is relatively independent of the multilayer thickness (*134*).

The stability of the protein coatings is limited due to the exchange process between the adsorbed biomolecules and larger protein molecules into solution (Vroman effect). It was observed that the BSA layer reduces the adsorption of fibrinogen. In another study, Huetz and colleagues studied the release for adsorbed polyclonal human immunoglobulins (IgG) in the presence of fibrinogen molecules in the solution (*135*). The process proceeds via rapid exchange during first few hours followed by slow desorption which was independent of the molecules in the solution. Later studies on the exchange process of adsorbed IgG revealed that the release is enhanced by the presence of IgG molecules in the solution (*136*). It was found that the adsorbed IgG

molecules form two populations. While the first type of the IgG molecules was irreversibly attached to the surface, the second population of the protein was able to release from the substrate in the presence of the IgG molecules in solution.

To evaluate the changes in the thickness upon the interactions of the films with medium components, the multilayers were brought in the contact with cell growth medium supplemented with 10% (v/v) of fetal bovine serum (FBS). The composition of fetal bovine serum is presented in Table 6.

Compound	Concentration in fetal bovine serum, mg/ml	Final concentration in cell medium, mg/ml
Albumin	23.2	2.32
Alpha Globulin	13.2	1.32
Beta Globulin	4.7	0.47
Gamma Globulin	0.121	0.0121
Haemoglobin	157.3	15.7

Table 6. *The main components of fetal bovine serum and their concentrations in the cell medium supplemented with 10% of FBS (137).*

The films were assembled on silicon wafers and the experiment was performed at the conditions used for cell culture (37°C, 5% of CO_2). The time of the adsorption was 1h as it was obtained from the QCM-D experiment (see 3.2.6.). Prior to the ellipsometry measurement, the substrates were quickly rinsed with Milli-Q water and dried with compressed air.

An evaluation of the ellipsometric thicknesses of the layers after the incubation with serum rich medium is summarized in Table 7.

Based on the ellipsometry data the multilayers can be divided into three groups.

The first group includes the layers with the high increase of the film thickness that may be associated with the adsorption of the protein layer on the top of the films. It consists of the films based on $PEI(PSS/PAH)_5$, $PEI(DexS/PAH)_5$, $PEI(Alg/PAH)_5$, $PEI(PSS/CH)_5$, $PEI(PSS/PDDA)_5$, $PEI(DexS/PDDA)_5$.

LbL system	Original film thickness, Å	Film thickness after the contact with medium, Å	Δ Film thickness, Å
$PEI(PSS/PAH)_5$	112 ± 8	164 ± 3	52
$PEI(DexS/PAH)_5$	104 ± 9	137 ± 9	33
$PEI(Alg/PAH)_5$	125 ± 5	151 ± 12	26
$PEI(PSS/CH)_5$	147 ± 10	179 ± 5	32
$PEI(DexS/CH)_5$	119 ± 10	134 ± 12	15
$PEI(Alg/CH)_5$	98 ± 3	67 ± 7	-31
$PEI(PSS/PDDA)_5$	158 ± 6	196 ± 14	38
$PEI(DexS/PDDA)_5$	145 ± 5	177 ± 4	32
$PEI(Alg/PDDA)_5$	141 ± 4	149 ±11	8

Table 7. *Comparison of ellipsometric thickness of LbL films before and after interaction with cell culture medium components.*

Ladam and co-workers investigated the interaction of human albumin with the $(PSS/PAH)_n$ multilayers (*138*). On the PSS-ending film the protein molecules formed a monolayer, while the thickness of the protein layer on the PAH-terminating film exceeded four times the largest dimension of native albumin

molecule. It was demonstrated that the protein-film interactions are driven by electrostatic interactions. The authors suggested two mechanism of the formation of thick protein layer onto PAH-terminating films. First mechanism includes the formation of highly organized dense protein layer with net positive surface charge that attracts new HSA molecules, while the second explanation is based on the PAH macromolecules of outer layer extend into the proteins film being therefore accessible for the interaction with the biomolecules in the solutions. The adsorption on PSS-ending layers is based onto the interaction with positive charges of albumin or due to the emerging of PAH molecules out of the PSS layer that could interact with albumin molecules.

The studies on the interactions of the $(PSS/CH)_n$ films with BSA, fibrinogen, γ-globulin and lysozyme revealed that the proteins form a dense layer even upon the interaction with similarly charged layers (*139*). It was observed that the higher adsorption was found for the proteins with smaller size suggesting that the protein-film interactions occur via protein diffusion within the multilayer structure.

The second group contains multilayers with a lower increase in their thickness after incubation with the cell growth medium and includes the assemblies based on $PEI(DexS/CH)_5$ and $PEI(Alg/PDDA)_5$.

Serizawa and colleagues studied that the $(DexS/CH)_n$ films for their blood anti- versus procoagulation activity (*140*). The alternating activity of the films was observed after the deposition of two layer pairs in the presence NaCl at concentration above 0.5 M. The layers terminating with DexS possessed strong anticoagulant properties while the films ending with chitosan demonstrated procoagulant activity. The assembly of the layers at lower NaCl concentration yielded the films with procoagulant properties. The $(DexS/CH)_n$ layers were compared with the $(HEP/CH)_n$ films, which showed strong anticoagulant activity independently of the chemistry of top layer and salt concentration used for LbL buildup. The authors concluded that the conformation of the polymer is responsible for alternating bioactivity. The strong anticoagulation properties of

(HEP/CH)$_n$ films are generated by the heparin that might interpenetrate the outmost chitosan layer present on the surface.

Müller et al. studied the interaction of (CH/Alg) layers with human serum albumin as a model protein (*141*). It was shown that the LbL layers terminating with polycation were highly attractive for HSA forming the layer on the surface of the film, while the architectures with alginate as top layer possessed protein-resistance properties.

Our results suggested that the PEI(Alg/CH)$_5$ architecture that exhibited decrease in the thickness after the interactions with cell growth medium associated with an exchange or a dissolution phenomenon.

For more detailed studies, the behavior of the films at cell culture conditions was evaluated by QCM-D measurements (see 3.2.6.)

3.1.5. Contact angle measurements

The wetting properties of the materials influence the process of protein adsorption and therefore influence the composition of the protein layer (*142, 143*).

Tristán and colleagues showed PEI(PAA/PAH)$_n$ layers assembled at acidic pH resisted the adhesion of negatively charged glucose oxidase and positively charged lysozyme, whereas the PEI(PAA/PAH) assembled at pH=7.4 favored the protein adsorption (*144*). The protein-resistance property of layers formed at acidic pH was explained by internal ionization state of the PAA molecules and hydration state of the film. At acidic pH, the excess of non-ionized carboxylic groups on the surface of the film results in the partial compensation of the positive charge of the last PAH layer. Since the electrostatic interaction is reduced compared to the film assembled at neutral pH, it was suggested that proteins-film interactions depend on the hydration state of the layers. As it was discussed in section 1.3.4, this type of layers was studied upon the interactions

with the murine fibroblasts. Due to the conformation changes and difference in the PAA ionization state, the (PAA/PAH)$_n$ layers assembled at acidic pH formed highly hydrated surfaces and resisted cell attachment, whereas the layers formed at pH = 6.5 promote cell adhesion.

The LbL approach allows to engineer the film with specific properties in order to control the protein adhesion process (*116*), cell attachment and cytoskeletal rearrangements on the surface (*27, 28, 117-119*).

The advancing contact angles for the water droplets are shown in Table 8.

As expected, the layers consisting of polysaccharides possess hydrophilic surfaces. The highest contact angle was observed for PEI(PSS/PAH)$_5$ layers. The replacement of PSS on DexS or Alg led to the formation of more hydrophilic coatings indicating that the underlying layer contributes to the wetting properties of LbL film. The same tendency was observed for the coatings containing PDDA. The highest contact angle (31±1°) was observed for the architecture based on PEI(PSS/PDDA)$_5$ and the lowest one for PEI(DexS/PDDA)$_5$ was 6±1°. The contact angle for the film based on PEI(Alg/PDDA)$_5$ was equal to 27±1°. These results suggested that the inner structure of the layers presents a complex system of interpenetrating polyelectrolytes (*145*). Therefore, the moieties of the underlying layers can be found at the surface and are accessible for the reactions with proteins, which may influence cellular behavior.

Since the properties of multilayers could dramatically change after the adsorption of the proteins, the wettability was checked after the interactions with the culture medium as in previous experiment.

In general, the values of the contact angle values of the films increased after the incubation with the cell medium. The observed changes could be induced by the possible structural rearrangements in the films upon the interaction with medium components and/or the formation of the proteins top layer.

LbL system	Contat angle, degrees	Contact angle after the incubation with cell growth medium, degrees
PEI(PSS/PAH)$_5$	42±2	47±1
PEI(PSS/PDDA)$_5$	31±1	45±1
PEI(DexS/PAH)$_5$	30±2	61±1
PEI(PSS/CH)$_5$	29±1	52±1
PEI(Alg/PAH)$_5$	27±1	61±2
PEI(Alg/PDDA)$_5$	16±2	56±5
PEI(Alg/CH)$_5$	9±1	28±5
PEI(DexS/PDDA)$_5$	8±1	18±5
PEI(DexS/CH)$_5$	6±1	69±5

Table 8. *The values of advancing contact angles for the LbL films.*

3.1.6. The Stability of LbL films

Since the release of the components of LbL films can affect cell viability and even induces undesirable cytotoxic effects via interactions with cell membrane (*146-148*), it is therefore important to explore the stability of LbL-systems in the cell culture medium at physiological conditions.

The stability of the multilayer films was evaluated by QCM-D measurements, since this method allows to follow on-line structural and mass changes simultaneously.

The goal of these experiments was to evaluate the interactions of LbL systems with the cell culture medium in the conditions close to those used for cell adhesion experiment and to correlate the results with the data on cell attachment and viability.

The experiment was performed in the QCM-D chamber equilibrated at 37°C by bringing in the contact the cell growth medium equilibrated to 37°C with LbL films deposited on the surface of the sensor.

The observed rapid decrease in the normalized frequency and the increase in the dissipation signals suggest that the films readily interacted with the cell medium. The saturation of ΔF and ΔD values was observed 60 min after the contact of the medium components with the layers (Annex, Figure 1-9).

The QCM-D measurement can be used for evaluation of swelling (*149*), rearrangements (*150*) and the changing in the conformation of the molecules (*151, 152*) near the surface of QCM-D sensor.

Our results suggested that the interaction of the medium with the layers can be divided into three phases. The first phase corresponds to the fast adsorption of the proteins on the surface of the layers. The deceleration of this process was observed 20 min after the medium injection followed by structural rearrangements of adsorbed proteins. The last phase, where the frequency and dissipation undergo only slight changes, probably corresponds to the exchange between the adsorbed proteins and the components of the medium.

The changes in the frequency signal for the LbL films upon the protein adsorption are summarized in Table 9. The increases in the mass were calculated using Sauerbrey equation (see section 2.4.1.). Although the application of this equation for the viscoelastic protein layer leads to the slightly incorrect values, it is used as an approximation to compare relative amounts of protein adsorbed by the films.

LbL system	ΔF, Hz	Δm, ng/cm^2
PEI(PSS/PAH)$_5$	-43	761
PEI(DexS/PAH)$_5$	-56	991
PEI(Alg/PAH)$_5$	17	-301
PEI(PSS/CH)$_5$	-174	3080
PEI(DexS/CH)$_5$	-102	1805
PEI(Alg/CH)$_5$	-50	885
PEI(PSS/PDDA)$_5$	-38	673
PEI(DexS/PDDA)$_5$	-58	1027
PEI(Alg/PDDA)$_5$	-50	885

Table 9. *Summary of QCM-D frequency shifts upon the interaction of the films with cell medium supplemented with 10% of FBS. The adsorbed mass was estimated using the Sauerbrey equation.*

While most of the films extensively interact with the cell medium resulting in the increase of the sensed mass, the multilayers PEI(Alg/PAH)$_5$ exhibited slight positive frequency shift (Table 9) suggesting the decrease in the adsorbed mass on the surface of QCM-D sensor. By contrast, almost no changes in the dissipation were observed. Moreover, as it was discussed in 3.3.3., the ellipsometric thickness of PEI(Alg/PAH)$_5$ layers increases after the interaction with serum growth medium. This suggests that the observed changes in the frequency signal (increase in the ΔF) could be due to a process other than partial dissolution of the film such as change in the film structure due to the presence of divalent ions in the culture medium that are able to complex alginate (*153*).

As it was discussed in the section 3.2.4, the ellipsometric thickness of the PEI(Alg/CH)$_n$ decreases after interaction with the cell medium. However, the QCM-D data revealed the increase in the sensed mass suggesting that the structure of the layers could be affected during the rinsing with mQH$_2$O or dure to the strong film dehydration during the film drying with compressed air before the ellipsometry measurements.

Further incubation of layers during 96 h did not lead to the dramatic changes in both frequency and dissipation curves suggesting that the studied LbL films maintain their composition stable at physiological conditions.

3.1.7. Surface topology

Surface topology and roughness significantly contribute to the cell-material interactions, cell functions and protein adhesion (*105, 154, 155*). To develop the relations between the colony formation and the material properties, the surface topography and roughness of LbL films were studied by atomic force microscopy. The LbL coated silicon wafers were incubated in the medium supplemented with 10% FBS at 37°C, 5% of CO$_2$. After 1h, the samples were allowed to dry at room temperature and then analyzed by AFM microscopy with Nanoscope III MultiMode Scanning Probe microscope (Veeco Instruments, California, USA).

For the cases discussed here we selected polymers that give comparable topologies (Figure 43). Other types of LbL-films showed rather rough surfaces (*156*).
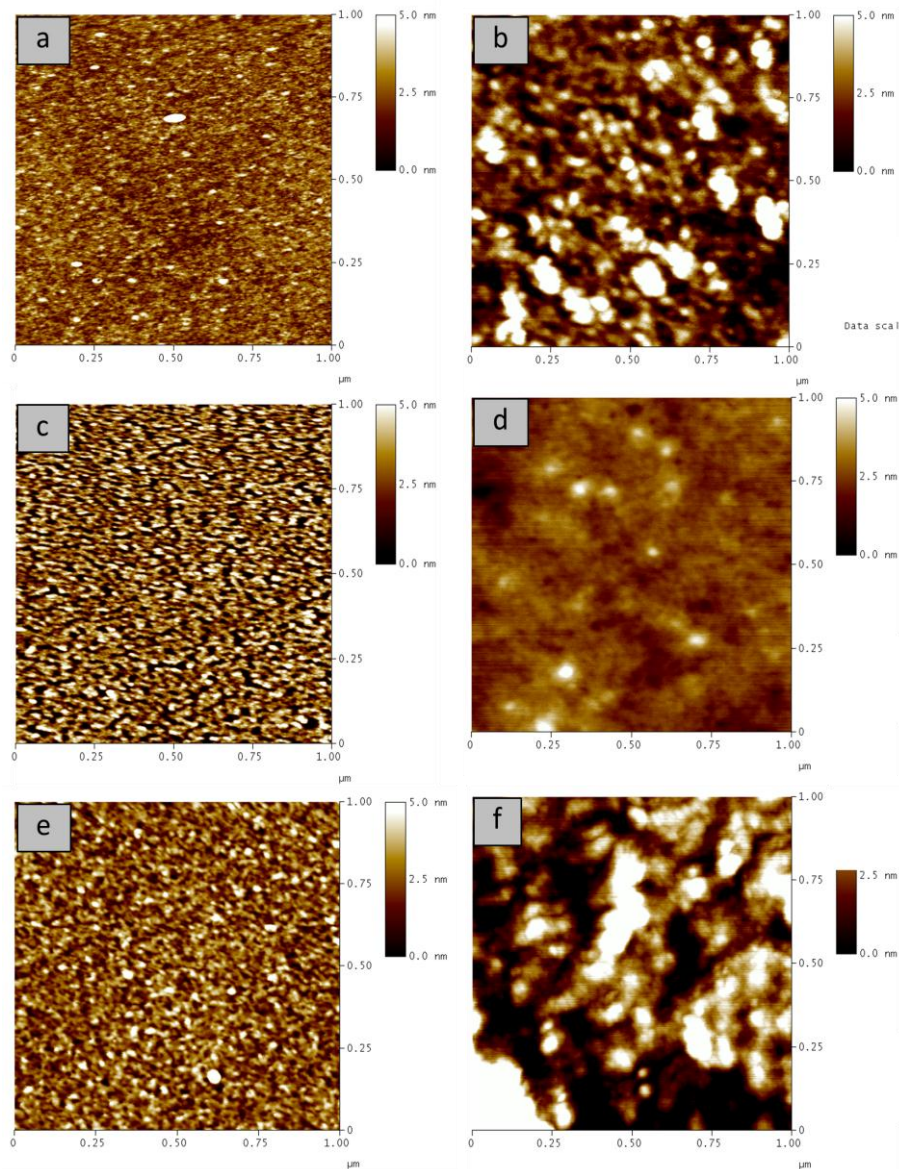
Figure 43. *Atomic force microscopy images of LbL initial films: PEI(PSS/PAH)$_5$ (RMS roughness ∼ 0.4 nm) (a), PEI(DexS/PAH)$_5$ (RMS roughness ∼ 0.9 nm) (c), PEI(PSS/CH)$_5$ (RMS roughness ∼ 0.9 nm) (e) and after the adsorption of FBS: PEI(PSS/PAH)$_5$ (RMS roughness ∼ 2.9 nm) (b), PEI(DexS/PAH)$_5$ (RMS roughness ∼ 1.3 nm) (d), PEI(PSS/CH)$_5$ (RMS roughness ∼ 3.0 nm) (f).*

3.1.8. Conclusions

A variety of films were assembled via layer-by-layer approach from the common polyelectrolytes and then examined to evaluate their biocompatibility to primary human dermal fibroblasts.

Although the multilayers rapidly interact with medium components, the cell viability and attachment data suggested that the cell functions are governed not only by the composition of the protein layer, but also by native chemical properties of the film.

On the basis of the results obtained here the films studied were divided into three different groups with respect to their interactions with the cells.

First group includes the coatings assembled with chitosan such as PEI(PSS/CH)$_5$, PEI(Alg/CH)$_5$, PEI(DexS/CH)$_5$. Although these LbL films resisted cell adhesion, the cells were still able to attach to the gelatin-coated surface and stayed viable after the incubation with the multilayers for 24h.

It was previously reported by Faucheux et al. that self-assembled monolayers (SAMs) carrying the hydroxyl groups, the chemical functionalities found in the chitosan, are employed to engineer cell-resistant substrates for the human fibroblasts (*143*). Consequently, the bioinert properties of the chitosan-based multilayers and highly adhesive properties of layers containing PAH, may certainly be explained by the presence of the corresponding chemical functionalities on the surface of the film.

The difference in the cell population on the layers PEI(PSS/PAH)$_5$, PEI(DexS/PAH)$_5$ and PEI(Alg/PAH)$_5$ reveals the influence of the properties of underlying polyanion. The lower density of cell grown on PEI(Alg/PAH)$_5$ compared to PEI(DexS/PAH)$_5$ may be likely related to the difference in their hydration state.

Stenger et al. demonstrated that the density of the hippocampal neurons is sensitive to the density and accessibility of charged amine and amide groups. It

was demonstrated that the density of adhered cells increased along with the concentration of charged amine groups (*157*).

Our results showed that the increasing charge density of amine groups gained by the introduction PDDA in the film composition leads to the cytotoxicity of corresponding layers. In this case the increased cell viability for the system PEI(Alg/PDDA)$_5$ and PEI(PSS/PAH)$_5$/PSS is related to the decreasing concentration of respective functional groups on the film surface, either due to the high hydration of the layers or deposition of additional PSS layer. Similar effect was observed for the native and crosslinked (PLL/PLGA)$_5$/PLL and (PLO/PLGA)$_5$/PLO architectures. The crosslinking of the layers increase the film stiffness of the films but also decrease the concentration of amine surface groups (Figure 41) that led to the enhanced cell spreading and proliferation.

The effect of the chemistry of the groups and their accessibility was further confirmed in the experiment with the film consisting of PAH and sodium hexamethaphosphate (PSP) (Figure 44).
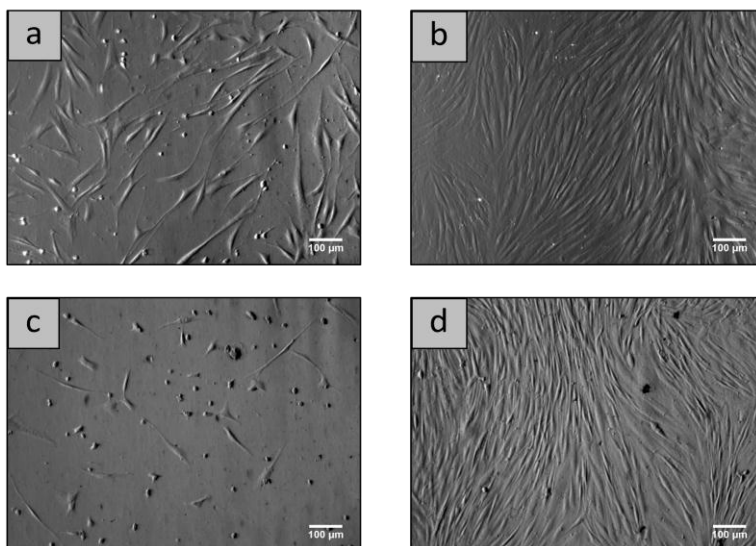

Figure 44. *CPRE2 cells onto PEI(PSP/PAH)$_3$ (a), PEI(PSP/PAH)$_3$/PSP (b), PEI(PSP/PAH)$_5$ (c) and PEI(PSP/PAH)$_5$/PSP (d). Images were taken 96h after cell seeding. The medium supplemented with 10% of FBS was used for cell culture.*

Although in the previous experiment the layers containing PAH possessed cell-adhesive properties, the cellular attachment was observed exclusively on the films with PSP as a topmost layer. As shown in Figure 44, the layers terminated with PAH exhibit cell-resistance properties. These effects tend to increase along with the number of layer pairs, which is related to the concentration of PAH macromolecules embedded into the film.

Although the protein top layer undoubtedly influences the cell adhesion, the effect of the top layer was found to be independent from the protein content in the medium. This fact confirms that the interactions of cells with the materials are mostly defined by the chemistry of surface groups (Figure 45).
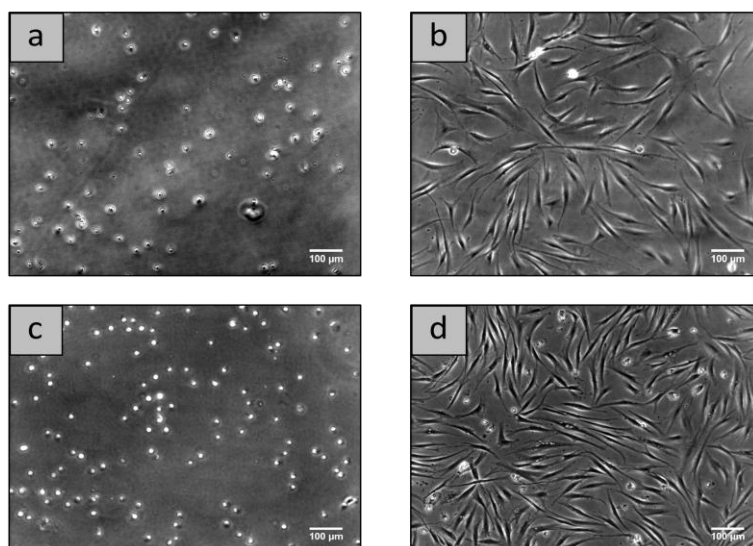

Figure 45. *CPRE2 cells seeded in the serum-free medium onto PEI(PSP/PAH)$_3$ (a), PEI(PSP/PAH)$_3$/PSP (b), PEI(PSP/PAH)$_5$ (c) and PEI(PSP/PAH)$_5$/PSP (d). Images were taken 48h after cell seeding. The serum-free medium was used for cell culture.*

3.2. Non-viral transfection of primary adult human dermal fibroblasts

Gene therapy offers a new concept for the treatment of severe human diseases by systematic or local delivery of nucleic acids to the patient cells (*38, 40, 41*).

The development of non-viral approach for successful introduction of exogenous nucleic acids into the host cells presents an alternative possibility to viruses as carries of nucleic acids for gene delivery process. The strategy of this approach involves the formation of soluble interpolyelectrolyte complexes of nucleic acid and positively charged macromolecules such as polymers, dendrimers, lipids and peptides via cooperative interactions between electrostatically complementary chains and further interaction of these complexes with the cells (*39, 47-50*).

The properties of the vector as a composite material depends on the concentration and molecular weights of reagents, their stoichiometric balance (N/P ratio) and pH, ionic strength and the temperature of the reaction mixture (*46*).

Among the existing polymers, linear poly(ethylenimine) (lPEI) is one of the most efficient carriers known at the present time (*47, 49, 50, 158*). Due to the high positive charge density this macromolecule effectively condenses DNA in small particles and thereby protects it from the degradation in endosomes (*159, 160*). The buffering capacity of amine groups or "proton sponge" effect results in the osmotic swelling of endosomes leading to endosomal escape of the particles into the cytosol (*54*). Despite high transfection efficiency of lPEI-based complexes, the possible toxic side effects can limit their application in long term and systematic transfection experiments (*56, 161*).

One of the goals of this thesis was the development of a robust, low toxic and efficient protocol for long term and systematic transfection of primary human adult dermal fibroblasts for its further application for non-viral production of pluripotent stem cells.

Due to the unique properties such as self-renewal and the ability to differentiate to any cell type of adult human body, stem cells are the most promising source for tissue regeneration and the development of the patient specific cells of therapeutic interest (*162*). However, due to ethical reasons, the investigation of this cell type for scientific research and clinical medicine is restricted. Currently, the most promising way to have an access to human stem cells is the genetic reprogramming of somatic fibroblasts into so-called induced pluripotent stem cells by introducing genes encoding four transcription factors *oct-4*, *sox2, klf4*, and *c-myc* (*163*). On one hand, this cell line has the properties of embryonic stem cells such as self-renewal and differentiation ability; in the other hand, its development helps to overcome the ethical issues attributed to the use of embryonic stem cells and adult stem cells.

Unfortunately the methods to reprogram human fibroblasts possess low efficiency and high cytotoxicity, and the development of a new alternative reprogramming approach is of crucial importance for future clinical applications (*164, 165*).

During this thesis different film compositions were tested systematically for transfection efficiency. From the multitude of experiments carried out, it was concluded that it is possible to control the quantity of the transfection agents and plasmid DNA in polyelectrolyte multilayer films by adjusting the number of layers. However, the transfection efficiencies of the LbL films with different cell lines remained weak, even when degradable polyelectrolytes were used for the film construction, and we decided to focus our efforts on the establishing the efficient transfection protocol for primary cells in bulk.

3.2.1. Nanobags containing DNA

In this work, we investigated the parameters of the systems being similar to the nanobags and consisting of linear poly(ethylenimine), pDNA molecules and trisodium citrate.

The vectors were prepared with plasmid DNA of 5757 bp coding green fluorescent protein (GFP). The spectral characteristics of this protein such as maximum absorbance at 395 nm and the emission at 509 nm allow to readily detect its expression by flow cytometry and fluorescent microscopy methods.

The transfection experiments were carried out with the CPRE2 cell line, primary human adult dermal fibroblasts, and transfection rate was determined as a percentage of fluorescent cells over total cell population 48h after the transfection. The transfection yield was evaluated using fluorescent microscopy and flow cytometry.

The cell viability after transfection was evaluated using TOPRO®-3 staining assay. The TOPRO®-3 iodide is a carbocyanine dye with the absorbance peak at 642 nm and emission at 661 nm which is able to bind to the dsDNA of cells. Since TOPRO®-3 iodide molecules can be excited by the helium-neon laser (633 nm), the population of the dead cells can be easily distinguished from that of viable cells by flow cytometry.

In the present experimental sequence, the concentrations of IPEI and DNA were kept constant, while the concentration of citrate was varied.

While the transfection experiment with the nanobags required 100 µL of the particle solution, in order to reliably measure the size of the flocs by DLS the sample volume must be at least 1 ml. For this reason the procedure for sample preparation was changed (see section 2.7.4.2.). The sample was prepared using four-fold greater volume of the reagent solutions and the resulted suspension was diluted with 0.15M NaCl up to 1 ml in order to arrive at a desired sample volume and the particle concentration. According to DLS data, a significant decrease in the nanobag size was observed at 2 mM of carboxylic groups in sodium citrate (Figure 46a). However, at higher concentrations of carboxylic groups the size of aggregates remained constant.

Similar behavior was observed for nanobags prepared at lower DNA concentration. A rapid decrease in the particle size was observed at the carboxylic groups concentration of 2 mM followed by a plateau at the

concentrations of carboxylic groups higher than 6 mM. As shown in Figure 45b, the ζ-potential of flocs gradually decreased along with the increase of the carboxylic groups concentration and was found to be independent of applied DNA concentration.
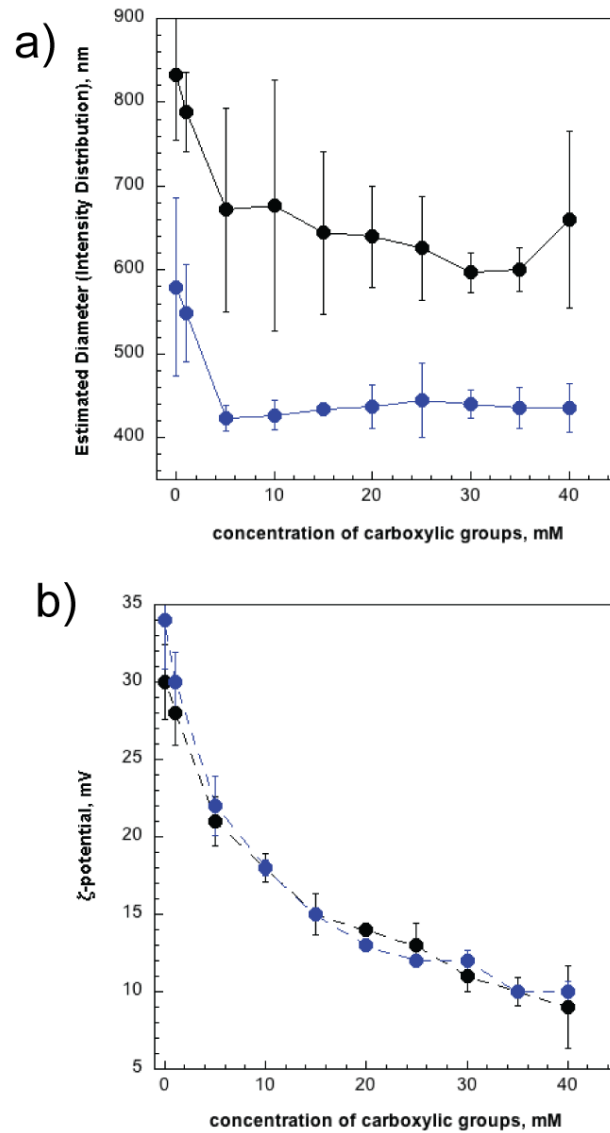

Figure 46. The estimated diameter (a) and *ζ-potential (b) of the nanobags with respect to the concentration of carboxylic groups of sodium citrate in the reaction mixture. The concentrations of DNA solutions were 0.06 mM (black) or 0.03 mM (blue). The concentration of lPEI was kept equal to 0.3 mM.*

Transmission electron micrographs of the polyplexes were obtained from solutions containing polyplexes, where the polyplexes were adsorbed from a 5 µL drop during 2 min on 400 mesh carbon-coated copper grids. After 2 min, the drops were removed with a filter paper and immediately replaced by a 5 µL of a solution containing 2 wt % of uranyl acetate. The staining solution was allowed to stay in contact with the sample for 1 min and was then removed by touching with a filter paper. The data confirmed that the diameter of nanobags decreases with increasing the citrate concentration. However, the aggregates prepared at high citrate concentration exhibit high polydispersity and oval morphology compared to original spherical two-component complexes (Figure 47). It is considered that the morphology of aggregates changes due to the electrostatic screening by citrate ions and reduced electrostatic repulsion between such soft particles. This results in the fusion of particles and formation of bigger irregularly shaped flocs.
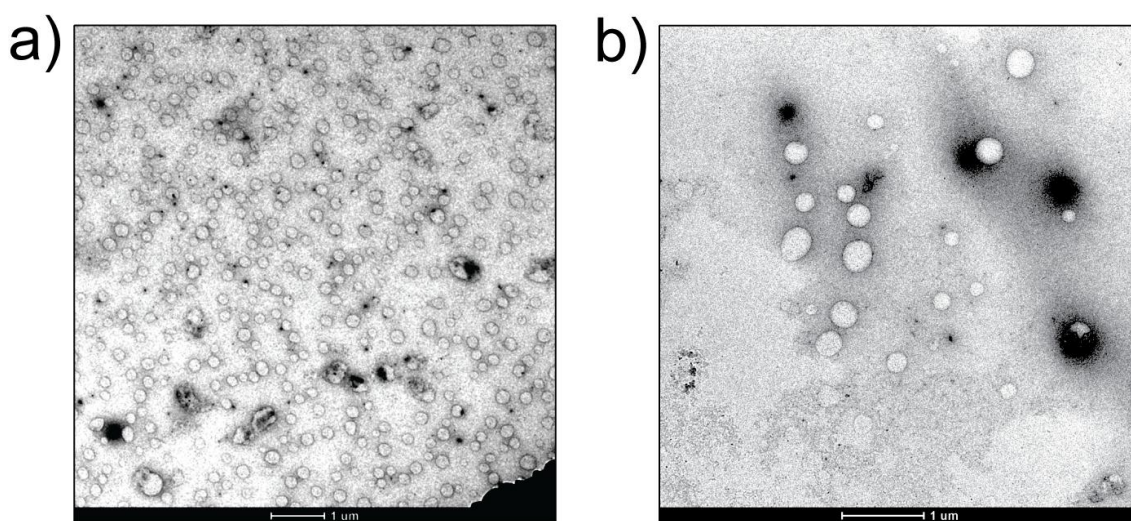

Figure 47. *TEM micrographs of polyplexes prepared at N/P=5 (left) and nanobags formed at N/P=5 using trisodium citrate at concentration 33 mM (40 mM of carboxylic groups in the reaction mixture).*

Irrespective of the citrate concentration, the transfection activity of the nanobags was found to be higher compared to that of the reference two-component sytem - the polyplexes prepared according to the standard protocol (N/P = 5) provided by Polyplus Transfection™ (*166*). This suggested that there was a room to optimize the trasfection protocol for CPRE2 with lPEI/DNA polyplexes.

3.2.2. lPEI/DNA complexes

The studied complexes were prepared by mixing of the solutions of pDNA and linear PEI at corresponding concentrations in the solution of 0.15M NaCl.

Since the parameters and the transfection activity of the polyplexes are defined by the stoichiometric balance N/P, the transfection yield and cytotoxicity of the vectors can be optimized by changing the concentration of PEI monomer units or nucleotide bases.

In the present approach the polyplexes were prepared at different N/P ratios by varying the concentration of DNA in the reaction mixture.

3.2.2.1. Transfection efficiency of lPEI/DNA polyplexes

The highest transfection efficiency (83%) was observed for the polyplexes prepared at N/P 7.5 (at P = 2 nmol) with 49% of cell viability. The transfection rates for the complexes formed at N/P 5 (P = 3 nmol) and N/P 15 (P = 1 nmol) were 72 % and 73 % respectively, while smaller amount of DNA used for polyplex formation resulted in increased cell viability (Figure 48). However, according to the light microscopy data (Figure 49), the viability of the cells transfected with the PLXs prepared at N/Ps 5 and 7.5 was higher than that obtained by FACS. This suggests that the cell viability might have been affected during the procedure of the sample preparation used for the FACS analysis (e.g. trypsinization).

The lowest transfection rate 15% and highest cell viability 87% were obtained with the cells transfected with polyplexes prepared at N/P=30 (P = 0.5 nmol).
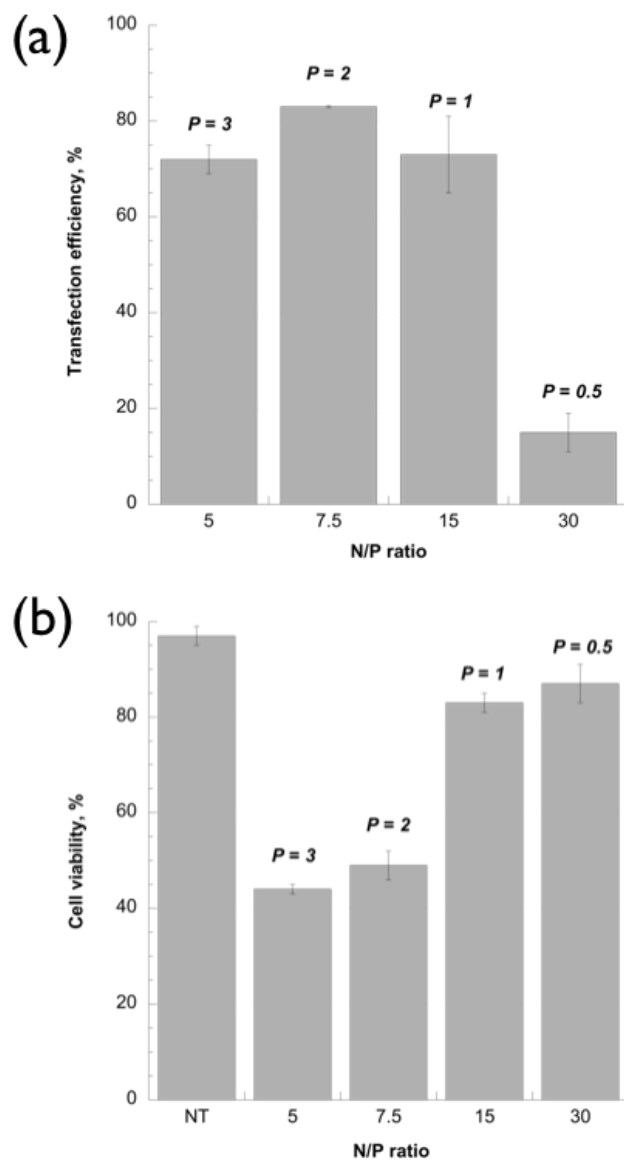

Figure 48. *FACS data on transfection efficiency (a) and cell viability (b) for the polyplexes prepared at different stoichiometric balances and the constant concentration of positive charges N (15 nmol). Abbreviation NT corresponds to the non-transfected cells.*
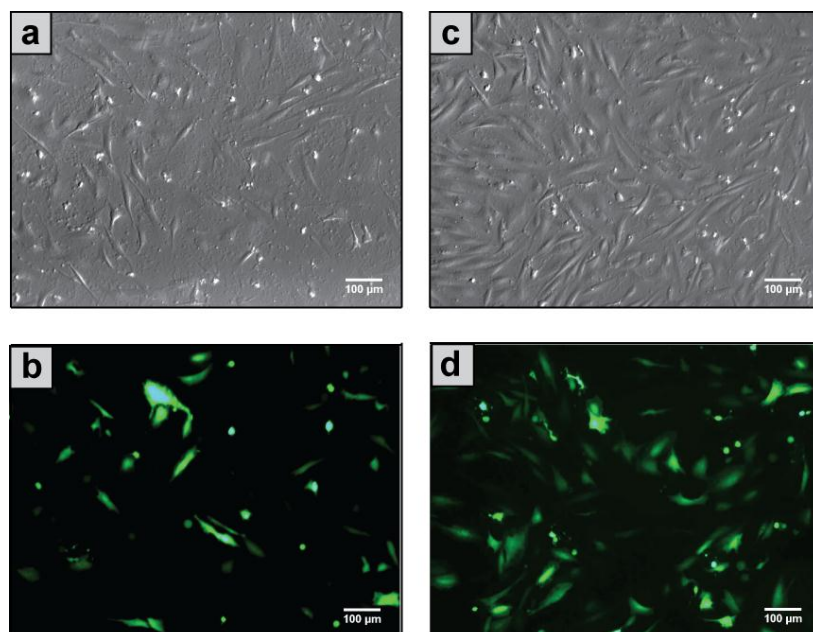
Figure 49. *The micrographs of CPRE2 cells treated with polyplexes prepared at N/P=5 (a and b) and N/P=7.5 (c and d) 48h after trasnsfection. The experiments were carried out in the medium supplemented with 10% of FBS.*

3.2.2.2. Characterization of IPEI/DNA polyplexes

To identify the parameters influencing the transfection rates, the size of polyplexes was analyzed by DLS. As for the DLS measurement of nanobag size, the sample was prepared using four-fold greater volume of the reagent solutions and the resulted suspension was diluted with 0.15M NaCl up to 1 ml (see section 2.7.3.2.). The data were obtained with freshly prepared samples in 0.15M NaCl at 25°C. The results showed that the decreasing DNA concentration leads to the formation of smaller particles. The estimated diameter of polyplexes at N/P=5 was 777±45 nm and 575±61 nm, 220±12 for particles formed at N/P 7.5 and 30 respectively.

The size of the polyplexes was analyzed by TEM according to the procedure described previously for the nanobags. The TEM data revealed that the

polyplexes exhibit spherical and homogeneous structure. The size of particles was considerably lower than that measured by DLS. The diameter of polyplexes at N/P 5 was found to be 200-300 nm whereas polyplexes formed at N/Ps 7.5 present around 100-200 nm (Figure 50). The disagreement in the data can be to the fact that in TEM the particles are studied in the "dry" state, while DLS measures the particle size in the suspension. In addition, the differences in the properties of the particles can be explained by the differences in the sample preparation procedures or the particle agglomeration in the solution.
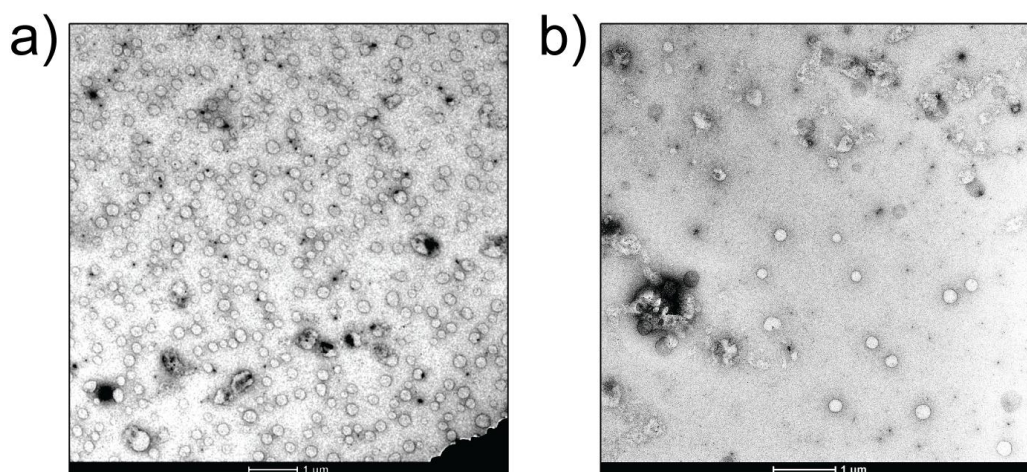

Figure 50. *Transmission electron micrographs of polyplexes prepared at N/P 5 while P is equal to 3 nmol (a) and at N/P 7.5, where P is equal to 2 nmol (b).*

For more detailed studies we then performed the analysis of polyplexes prepared at different N/P ratios for fixed DNA concentrations (Table 2) used in the previous experiment.

The DLS data revealed that the decrease of DNA concentration results in the formation of smaller complexes (Figure 51a). As expected, the size of the particles decreases along with the increase of N/P ratio. The increase of lPEI concentration for the polyplexes prepared with $P = 1.5$ nmol, 2 nmol and 3 nmol

led to the formation of smaller particles with higher positive charge density whereas increased N/P ratios for the polyplexes formed at $P = 0.5$ nmol results in a decrease in their positive charge (Figure 51b).
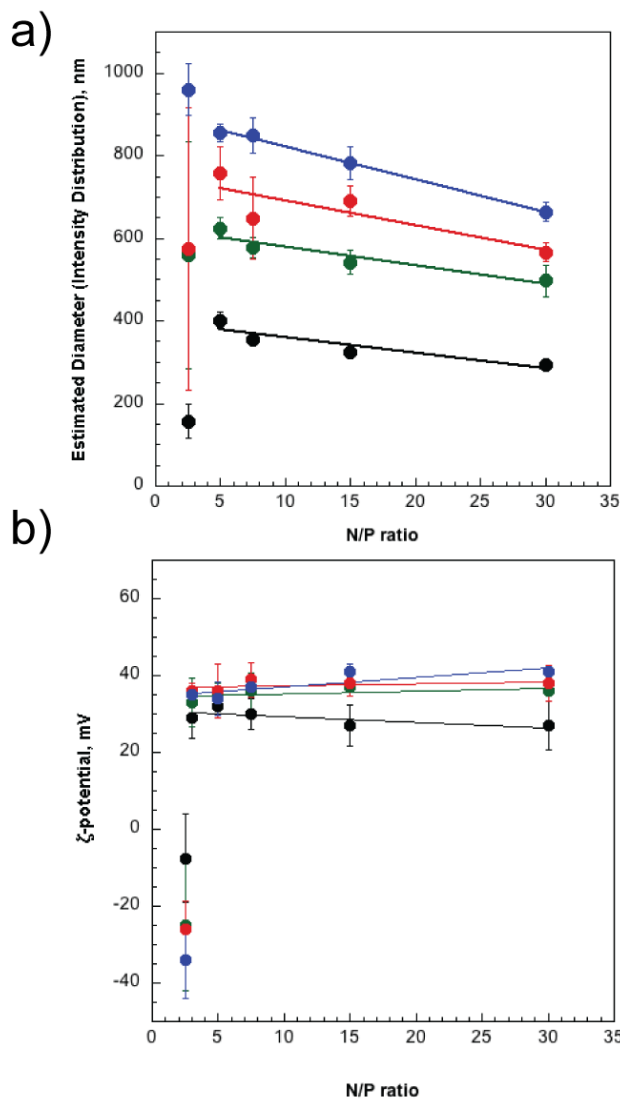

Figure 51. *DLS data: estimated diameter (a) and ζ-potential (b) obtained for PEI/DNA polyplexes prepared at different N/P ratio for P equal to 0.5 nmol (black), 1.5 nmol (green), 2 nmol (red) and 3 nmol (blue).*

As shown in Figure 51b, the polyplexes formed at N/P 2.5 possess negative charge suggesting that the concentration of lPEI is insufficient for the complete

DNA condensation, whereas for N/P ratio 3, the formation of the polyplexes with positive ζ-potential was observed.

On the basis of these observations, it was assumed that the difference in the complex parameters and therefore in their transfection ability might occur due to the difference in the viscosity of the initial DNA solutions.

Usually the efficient condensation of DNA for gene transfer is achieved in the polyplexes formed at an excess of polycation. However, the high density of amino groups induces undesirable cytotoxic effects, which limit their applications *in vitro* and *in vivo*.

In the present work, the lPEI-based complexes for the transfection of primary It was found that the size of the nanobags made of DNA, lPEI and sodium citrate can be varied by changing the citrate concentration. Although the incorporation of the citrate molecules led to the decrease of the complexes ζ-potential and to the particle fusion, the transfection efficiency of the nanobags was higher compared to the polyplexes prepared at N/P 5.

The DLS and TEM data revealed that the decrease in DNA concentration applied for polyplex preparation led to the decrease in the particle size, while their ζ-potential underwent only slight changes. While the best transfection activity was observed for the complexes prepared at N/P 7.5 (for *P* was equal to 2 nmol), the subsequent decrease in the DNA concentration led to the decrease in both polyplex size and transfection efficiency.

The ability of the dsDNA molecules for self-assembly and for formation of liquid crystalline phase was extensively studied during past years (*167-169*). However even in the diluted solutions the interactions between DNA molecules lead to their spontaneous segregation (*170-172*). The presence of such aggregates in the reaction mixture can influence the process of complex formation and can therefore affect the parameters of the resultant particles.

The present results demonstrate that the DNA concentration has a strong effect on the properties of resulted complexes and remains to be considered as one of the main control parameters for transfection process.

3.3. QCM-D/Transfection studies

The development of methods for following the transfection *in situ* and for detecting the onset of cytotoxicity could lead to new insights in the field of gene delivery, which is today mostly explored by trial-and-error approach.

QCM-D is an ultrasensitive, label-free and non-invasive technique providing *in situ* the information of the cell dynamics via the changes in the frequency and energy dissipation of QCM-D sensor.

In the QCM-D/cells studies, the cells adhered to the sensor can be considered as a thick dense layer of the "bulk" material on the sensor surface. The decay length for the shear wave in water at 5 MHz is considerably shorter (~0.25 μm) than the typical cell size and therefore only the changes of a fraction of the cell close to the sensor surface are detected. Thus, the QCM-D response will mostly be influence by the cell bulk material and not by the medium above the cell layer (*78*).

For the first time, we started to use quartz crystal microbalances with dissipation (QCM-D) for *in situ* monitoring transfection via cytoskeleton movements.

In this thesis work, the cells were seeded onto the surface of QCM-D sensor coated with PEI(PSS/PAH)$_5$ film or gelatin and allowed to grow in the medium supplemented with 10% of FBS at 37°C and 5% of CO_2 for 24h. The sensors with cells were rinsed with phosphate buffered saline and mounted in the QCM-D chamber equilibrated to 37°C. The cell medium equilibrated to 37°C was injected in the chamber and stable baseline was achieved prior to the addition of polyplexes.

The induced cytoskeleton changes after the polyplex injection were analyzed as the changes in viscoelastic properties of cell layer. Although the experiments were carried out at several overtones of resonance frequency, the data presented here were acquired at third overtone as the QCM-D signals at higher overtones were less pronounced.

Before discussing the QCM-D responses of transfected cells, it is constructive to consider more simple case: cells growing in the serum-containing medium. Figure 51 depicts the dissipation and frequency curves of CPRE2 cells growing on QCM-D sensor in a serum-containing medium. The injection of the medium induced an initial sharp decrease (Figure 52 a and b, peak A) in the dissipation and frequency signals probably due to the mechanical perturbation of the protein layer on the cell surface and possible exchange processes between the components of cellular protein layer and the medium.

The dissipation signal (Figure 52b) gradually increases and shows only one broad peak (B) with maximum at 1100 min (~18 h) whereas the frequency curve exhibits continuous growth until a relatively constant value at approximately 1500 min (25 h). This indicates an increase of sensed mass accompanied by changes in viscoelastic properties of the system and may be attributed to the mitotic cell rounding. During mitosis, the cells undergo reversible cytoskeleton changes through de-adhesion process accompanied by a gradient of intercellular osmotic pressure (*173, 174*). The changes in the cell shape from essentially flat to round induce the increase of the viscoelastic properties of the cell layer and the dissipation signal. After the mitosis is completed the cells re-spread on the sensor surface causing the decrease in the viscoelastic properties of the cell layer and decrease in the dissipation.
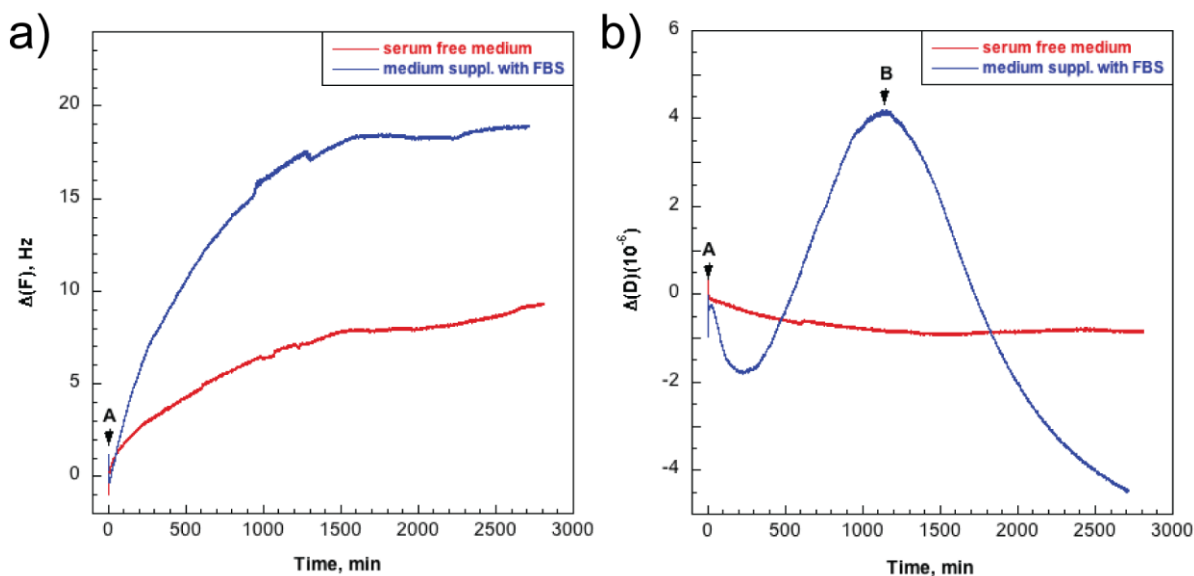
Figure 52. *Frequency (a) and dissipation (b) responses of CPRE2 cells seeded onto QCM-D sensors covered with PEI(PSS/PAH)$_5$. Peak A corresponds to the mechanical perturbation of the protein layer on the cell surface due to the medium injection, peak B might be attributed to the mitotic cell rounding. The experiments were performed in medium supplemented with 10% of FBS (blue) and serum free medium (red).*

To verify this assumption, the results were compared to the QCM-D response of the cells cultivated in a serum-free medium where the cell division is typically less pronounced. As in the previous experiment, the frequency shows continuous growth whereas the corresponding signal for the dissipation slightly decreases until a plateau and does not possess any well-defined peaks. Thus, it is reasonable to associate the dissipation response of the cells growing in the serum-containing medium (Figure 52) to the changes of cytoskeleton with the cell mitosis.

For the transfected cells (Figure 53), the dissipation and frequency curves exhibited new components as shown in Figure 54 that correspond to the transfection process.

The injection of polyplexes results in clear rapid changes in the dissipation and frequency that achieved their saturations around 200 (peak C) and 100 min (peak Cf), respectively. The second maximum of the dissipation (peak D) is found at approximately 500 min post transfection while frequency curve exhibits two minima at 400 min (Df) and at 2000 min (Ef). The dissipation peak assigned earlier to mitosis in the reference system (non-transfected cells treated with serum-containing medium, Figure 52b) can be seen as a shoulder at 1100-1300 min.

The intensity and the shape of the QCM-D signals depend on the concentration of proteins and on the viscoelastic properties of the layers between the cells and the sensor surface (Figure 55).

While the frequency response for the cells transfected in cell growth medium possess similar shape but slightly differ in its intensity, the response of the cells transfected in the serum free medium exhibit rapid growth followed by leveling off to a constant value.
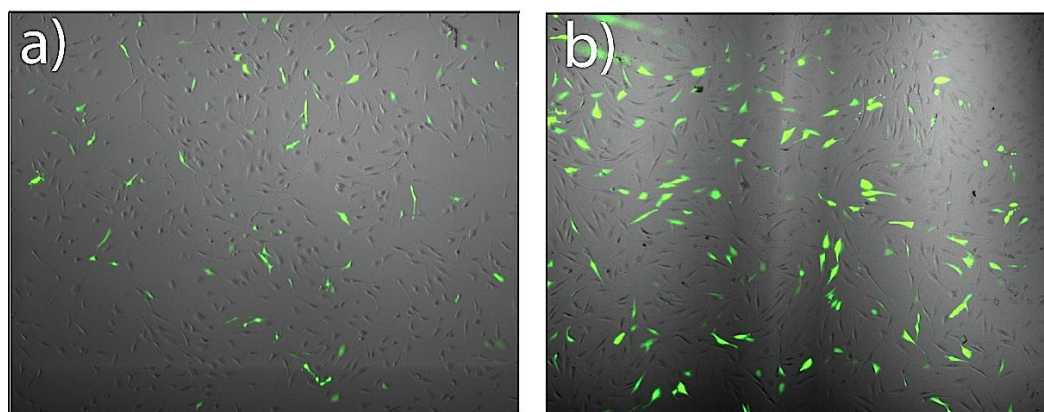

Figure 53. *The micrographs of CPRE2 cells transfected with lPEI/DNA polyplexes at N/P=7.5 in the QCM-D chamber 24h (a) and 48h (b) post-transfection (magnification 20×).*
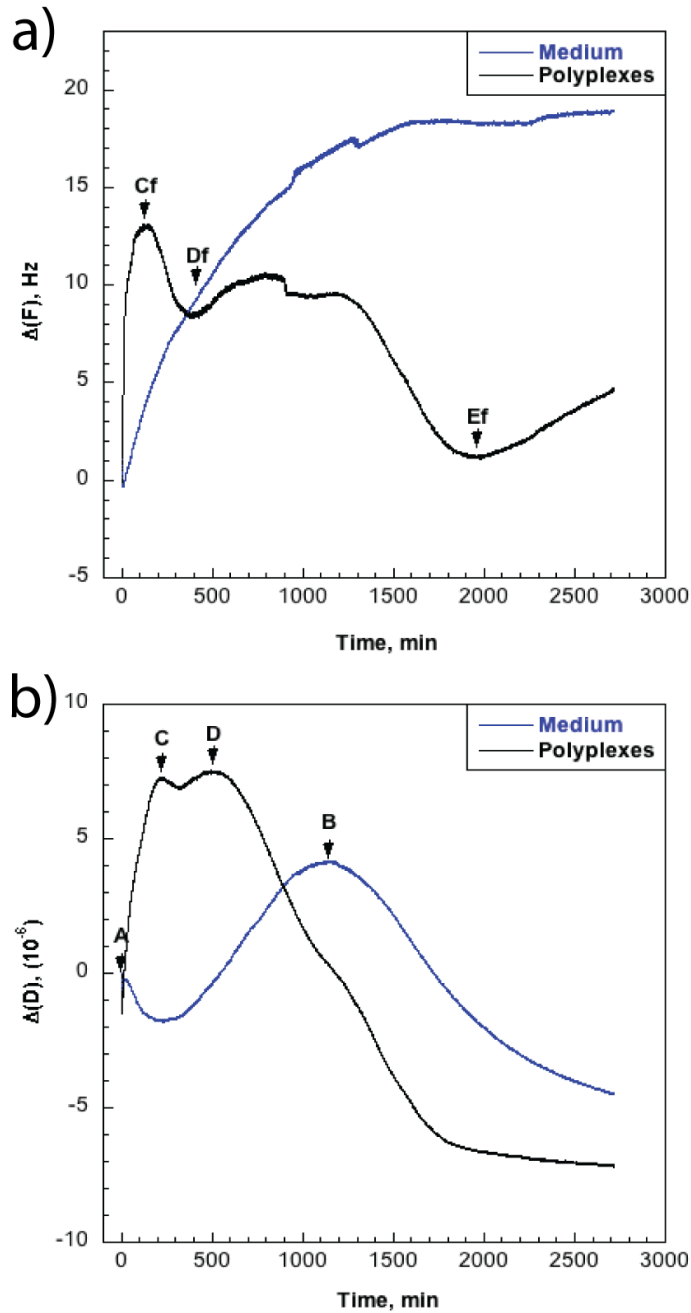
Figure 54. *QCM-D frequency (a) and dissipation (b) signals versus time for CPRE2 cells transfected with IPEI/DNA polyplexes (N/P 7.5) (black) or treated with medium without polyplexes (blue). Peak A corresponds to the mechanical perturbation of the protein layer on the cell surface due to the medium injection, peak B might be attributed to the mitotic cell rounding. The experiment was performed in the medium supplemented with 10 % of FBS; QCM-D sensor was coated with PEI(PSS/PAH)$_5$ – film.*
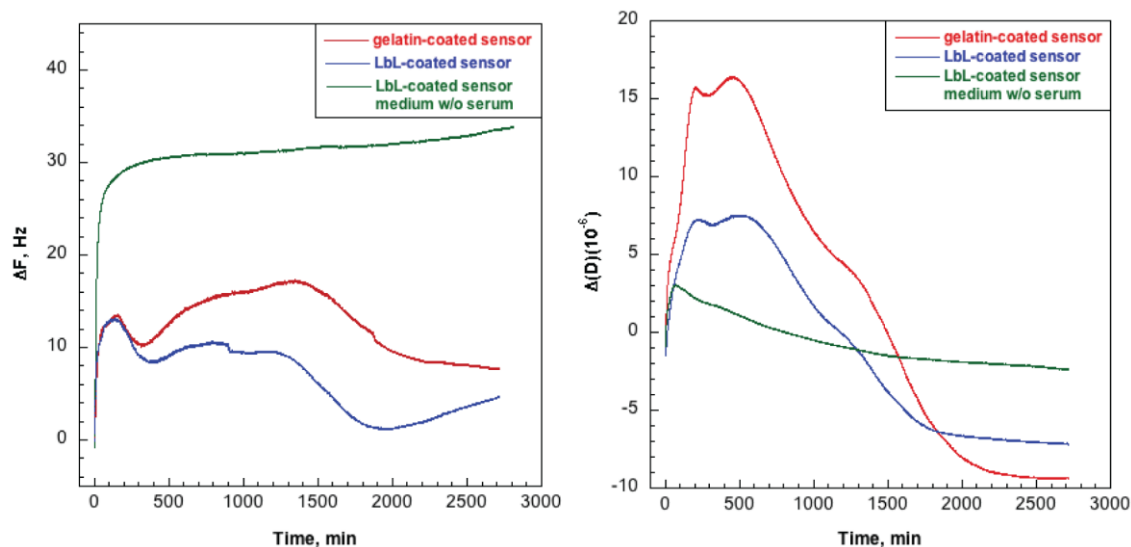
Figure 55. *Comparison of the frequency (left) and dissipation (right) signals of cells seeded onto the sensor coated with PEI(PSS/PAH)$_5$ film and transfected with lPEI/DNA polyplexes (N/P 7.5) in cell growth medium contained 10% of FBS (blue) or serum free medium (green). The red curve corresponds to the frequency and dissipation response of the transfected cells seeded onto gelatin-coated sensor in cell growth medium contained 10% of FBS.*

The dissipation signal obtained for the cells transfected in the medium containing 10% of FBS showed more intense and pronounced profile compared to those in serum free medium. Likewise, the comparison of the QCM-D experiments performed with the sensors covered either with PEI(PSS/PAH)$_5$ or gelatin suggests that the presence of softer film between cells and sensor surface yields an increased dissipation signal (Figure 54).

Numerous studies demonstrated that the interactions between lPEI/DNA complexes and the cells typically occur within few minutes after their addition to the cell culture, while the internalization of the vectors and their active intercellular transfer is found to occur in the few hours after the polyplex attachment to the surface of cellular membrane (*59, 60, 175-178*).

Cans and colleagues employed QCM-D for monitoring the mass change and the cell rigidity during the exocytosis and the subsequent retrieval of the vesicles (*179*). Stimulation of NG 108-15 and PC 12 cells to exocytosis was achieved by their exposure to the medium with increased potassium concentration. This resulted in the rapid frequency increase corresponding to the mass loss followed by a decrease in the signal suggesting the mass uptake upon the retrieval of the vesicles. The changes in the dissipation response were attributed to the changes in the rigidity of the cell layer. The increase and subsequent increase in the dissipation signal were related to the decrease and increase in cell membrane area upon exo- and endocytosis, respectively.

For proper assignment of the peaks C and D of dissipation curves (Figure 54b) in the transfection experiment, the QCM-D response on the interactions of CPRE2 cells with IPEI at concentration used for cell transfection (0.3 mM) was studied and compared with that for the polyplexes (Figure 56).

The results showed rapid adsorption of the polymer on the surface of the cell layer leading to an initial stepwise increase in the dissipation and corresponding decrease in the frequency. Further decrease in the frequency signal was accompanied by an increase in the dissipation that reached the maximum at 100 min (peak P1) after IPEI injection. Although the peak is slightly shifted, the dissipation response is similar to that obtained for transfected cells. It was observed that the position of the peak and its intensity depend on the IPEI concentration. Exposure of the cells to a higher IPEI concentration (1.5 mM) yielded a narrow dissipation peak at 50 min (peak P2) with higher intensity, as shown in Figure 56. The absence of the peak corresponding to the cell division (peak B) for the cells treated with IPEI may correspond to the cytotoxic effect of the polymer.
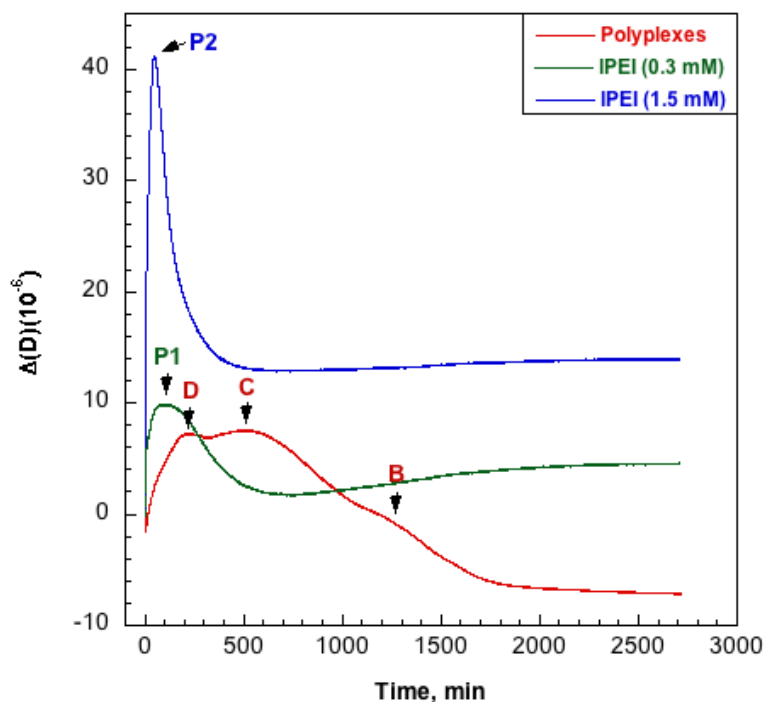
Figure 56. *The dissipation response of CPRE2 cells upon interaction with polyplexes (red), IPEI at concentration 0.3 mM (green) and 1.5 nmol (blue). The experiment was carried out in the medium supplemented with 10 % of FBS; QCM-D sensors were coated with PEI(PSS/PAH)$_5$ – film.*

Taking in account the results presented above, it is reasonable to assume that the first section of the dissipation and frequency curves for transfected cells including peak D may be attributed to the early stage of the transfection process including binding of polyplexes to the cell surface and following cellular uptake while the second part of the graphs with the peak C in the dissipation may be associated with the intercellular transport and transcription processes.

In conclusion, it was shown that the QCM-D technique allows *in situ* monitoring of the transfection process and survival upon the treatment. The transfection yielded a unique reproducible signature of frequency and dissipation curves due to the real time responses of cytoskeleton changes upon the interaction with transfection vectors. It was demonstrated that the intensity and profile of the QCM-D responses are strongly dependent on the concentration of the reagents,

protein content and the viscoelastic properties of the film between the cells and sensor surface.

4. Conclusions and perspectives

1. The influence of chemical composition on the properties of PEI/DNA complexes was studied. Size, charge and morphology of such vectors were determined by dynamic light scattering, zeta potential and transmission electron microscopy. The incorporation of a small trivalent ion, trisodium citrate, during vector preparation allows to control size, charge and morphology of the vector. It was shown that the increase of citrate concentration leads to the decrease of size and charge of the particles.

2. A protocol for efficient transfection of adult human dermal fibroblasts was established. It was demonstrated that the decrease in DNA concentration results in the formation of small particles with high transfection ability and low cytotoxicity. The established protocol can be further applied for systematic transfection experiments and evaluation of advanced vectors to safe and robust direction of a primary cell line to induced pluripotent stem cells.

3. The influence of chemical composition, stability, wettability of LbL films on viability and adhesion of adult human dermal fibroblasts was investigated. It was shown that the adhesion properties depend strongly on the chemistry of outer layer pair. The studied films allowed to control the adhesion of primary cells in the presence of serum proteins and could be further exploited in the development of advanced implantable materials and vectors for long-term transfection *in vivo* and *in vitro*.

4. It was demonstrated that the interactions of cells with polyplexes and the transfection process can be *in situ* monitored by quartz crystal microbalances with enhanced dissipation (QCM-D) via cytoskeleton movements. Further transfection studies by QCM-D in combination with other techniques, such as light microscopy, will contribute in revealing

the mechanism of transfection and will allow to develop a new approach for screening of individual drug dosage.
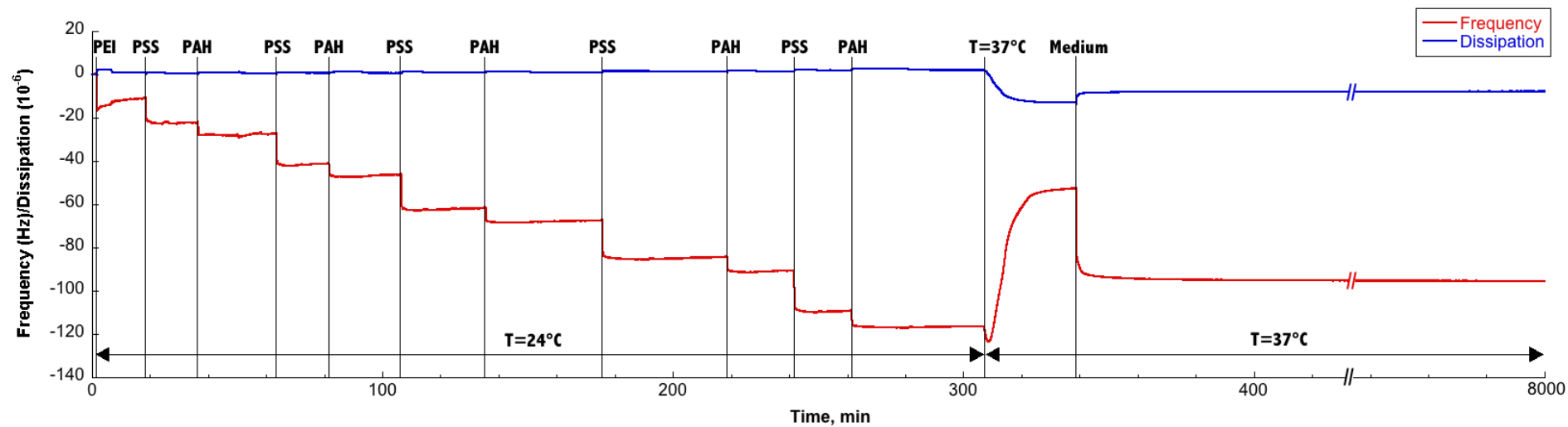
Annex

Figure 1. *QCM-D Data: the LbL built-up (at 24°C) and the stability of the of PEI(PSS/PAH)$_5$ film. After LbL assembly was completed, QCM-D chamber was equilibrated to 37 °C and the cell growth medium was injected into the chamber. The stability of the LbL film at the conditions used for cell culture was evaluated during 96h after medium injection.*

Figure 2. *QCM-D Data: the LbL built-up (at 24°C) and the stability of the of PEI(DexS/PAH)$_5$ film. After LbL assembly was completed, QCM-D chamber was equilibrated to 37 °C and the cell growth medium was injected into the chamber. The stability of the LbL film at the conditions used for cell culture was evaluated during 96h after medium injection.*
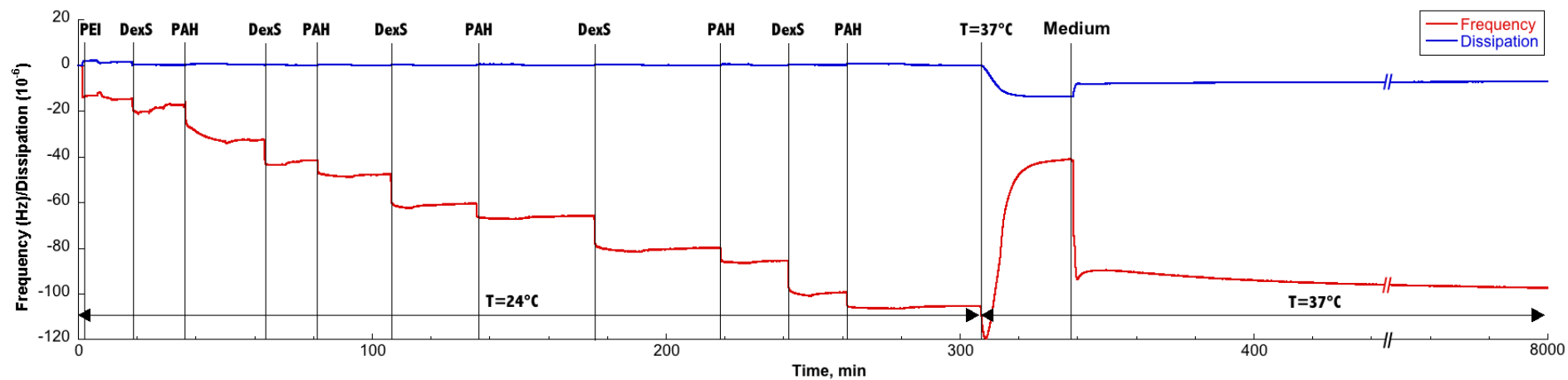
Figure 3. *QCM-D Data: the LbL built-up and the stability of the of PEI(Alg/PAH)₅ film. After LbL assembly was completed, QCM-D chamber was equilibrated to 37 °C and the cell growth medium was injected into the chamber. The stability of the LbL film at the conditions used for cell culture was evaluated during 96h after medium injection.*

Figure 4. *QCM-D Data: the LbL built-up (at 25°C) and the stability of the of PEI(PSS/CH)$_5$ film. After LbL assembly was completed, QCM-D chamber was equilibrated to 37 °C and the cell growth medium was injected into the chamber. The stability of the LbL film at the conditions used for cell culture was evaluated during 96h after medium injection.*
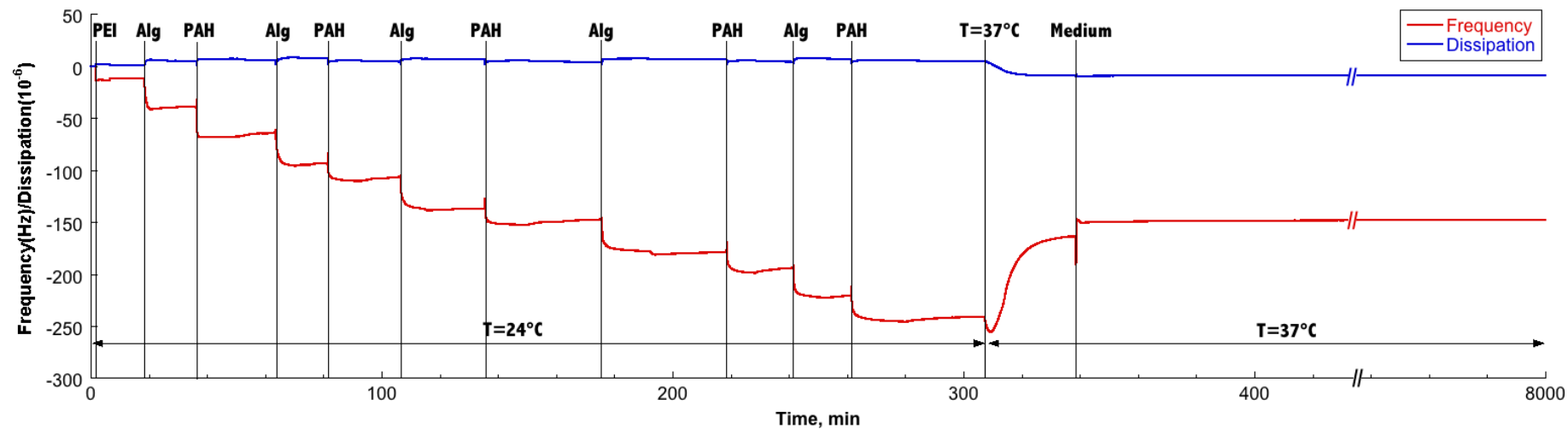
Figure 5. *QCM-D Data: the LbL built-up (at 25°C) and the stability of the of PEI(DexS/CH)₅ film. After LbL assembly was completed, QCM-D chamber was equilibrated to 37 °C, and the cell growth medium was injected into the chamber. The stability of the LbL film at the conditions used for cell culture was evaluated during 96h after medium injection.*
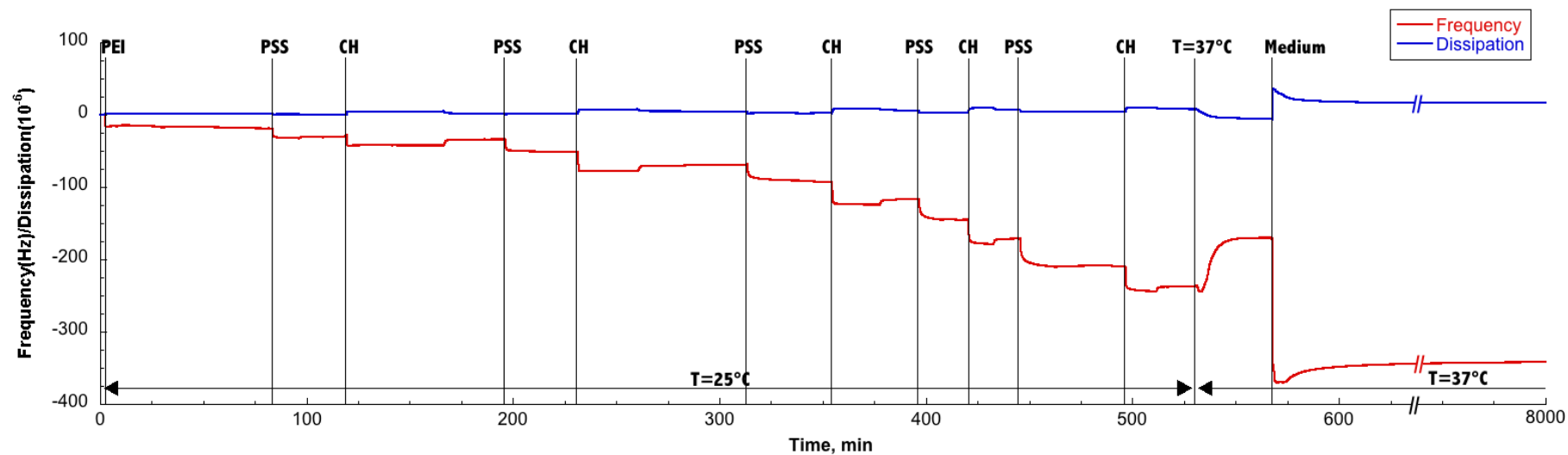
Figure 6. *The LbL built-up (at 25°C) and the stability of the of PEI(Alg/CH)$_5$ film. After LbL assembly was completed, QCM-D chamber was equilibrated to 37 °C, and the cell growth medium was injected into the chamber. The stability of the LbL film at the conditions used for cell culture was evaluated during 96h after medium injection.*
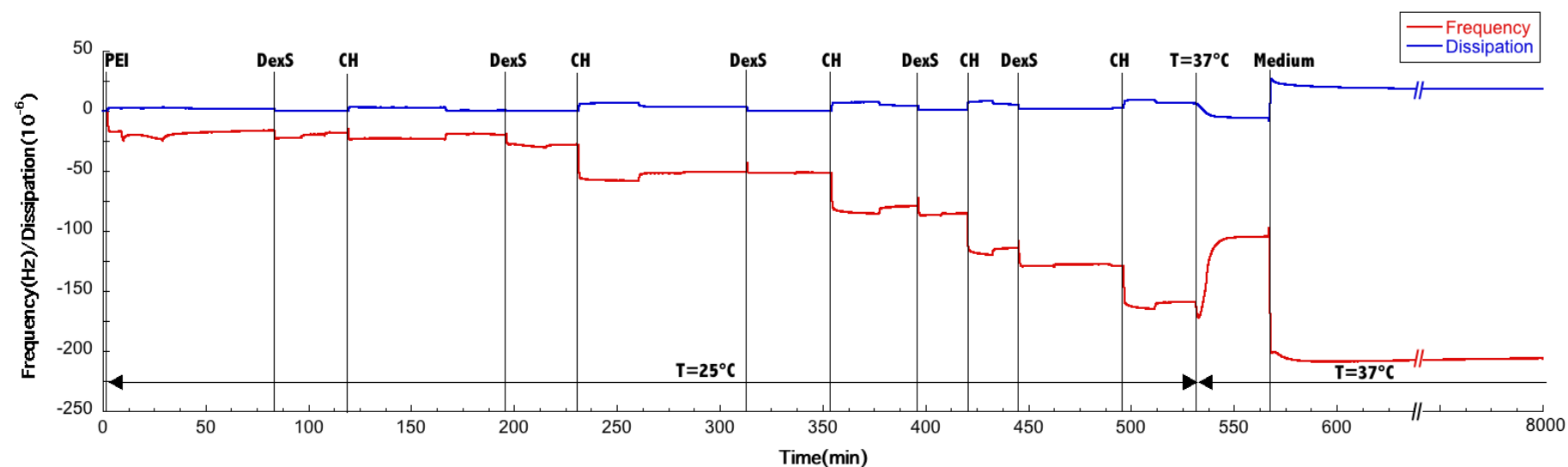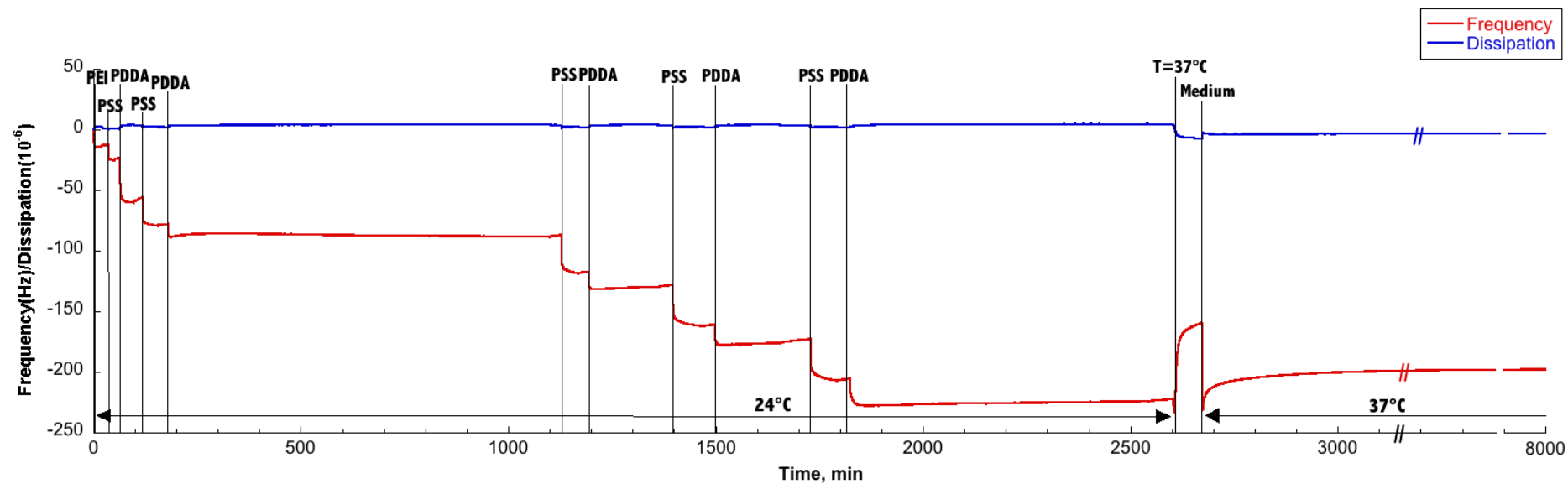
Figure 7. *The LbL built-up (at 25°C) and the stability of the of PEI(PSS/PDDA)₅ film. After LbL assembly was completed, QCM-D chamber was equilibrated to 37 °C, and the cell growth medium was injected into the chamber. The stability of the LbL film at the conditions used for cell culture was evaluated during 96h after medium injection.*
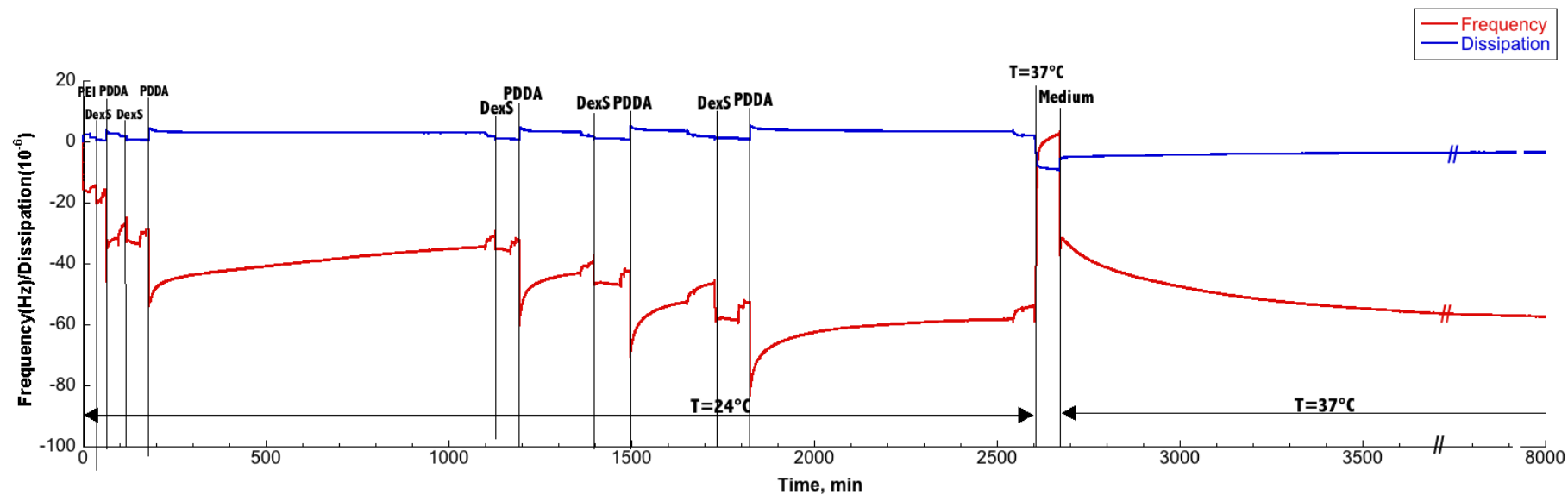
Figure 8. *QCM-D Data: the LbL built-up (at 24°C) and the stability of the of PEI(DexS/PDDA)$_5$ film. After LbL assembly was completed, QCM-D chamber was equilibrated to 37 °C, and the cell growth medium was injected into the chamber. The stability of the LbL film at the conditions used for cell culture was evaluated during 96h after medium injection.*
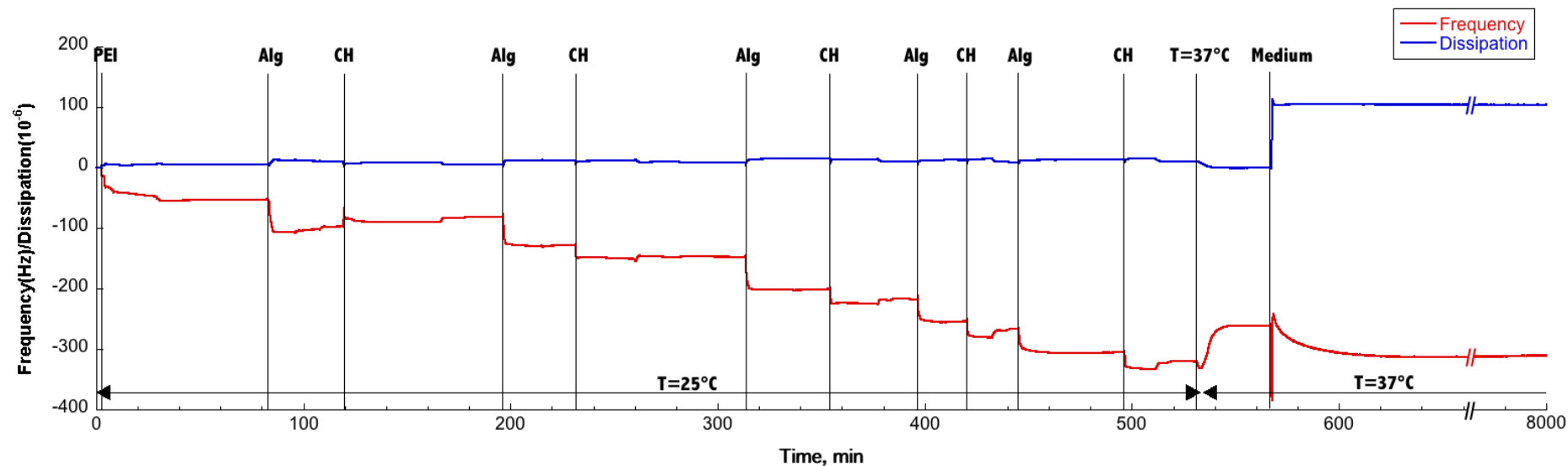
Figure 9. *QCM-D Data: the LbL built-up (at 24°C) and the stability of the of PEI(Alg/PDDA)₅ film. After LbL assembly was completed, QCM-D chamber was equilibrated to 37 °C, and the cell growth medium was injected into the chamber. The stability of the LbL film at the conditions used for cell culture was evaluated during 96h after medium injection.*
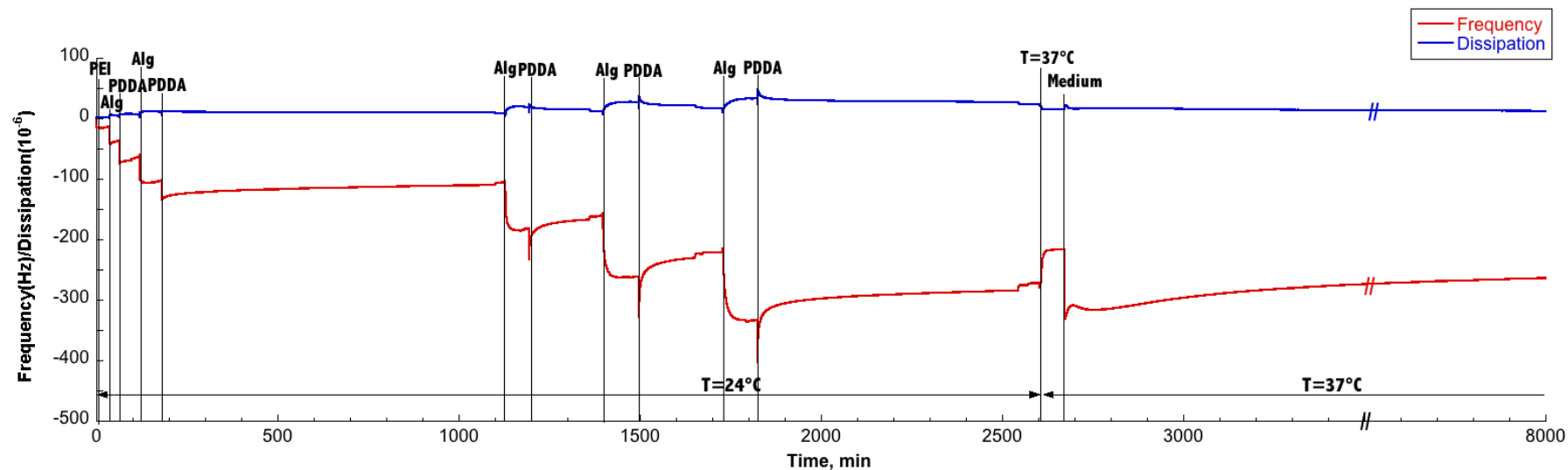
References

1. van der Gucht, J., Spruijt, E., Lemmers, M., Cohen Stuart, M. A., *Journal of Colloid and Interface Science* **361**, 407-422 (2011).
2. Kabanov, V. A., *Polymer Science* **36**, 143-156 (1994).
3. Tsuchida, E., Abe, K., *Interactions Between Macromolecules in Solution and Intermacromolecular Complexes. Advances in Polymer Science* (Springer Berlin Heidelberg, 1982), vol. 45.
4. Nakajima, A., *Journal of Macromolecular Science, Part B: Physics* **17**, 715-721 (1980).
5. Kötz, J., Hahn, M., Philipp, B., Bekturov, E. A., Kudaibergenov, S. E., *Die Makromolekulare Chemie* **194**, 397-410 (1993).
6. Kabanov, V. A., *Yspehi himii* **74**, 5-23 (2005).
7. Krotova, M. K., Vasilevskaya, V. V., Khokhlov, V. R. , *Polymer Science Series A* **51**, 1075-1082 (2009).
8. Tsuchida, E., Osada, Y., Abe, K., *Die Makromolekulare Chemie* **175**, 583-592 (1974).
9. Michaels, A. S., Miekka, R. G., *Journal of Physical Chemistry* **65**, 1765-1773 (1961).
10. Tsuchida, E., Osada, Y., Sanada, K., *Journal of Polymer Science Part A-1: Polymer Chemistry* **10**, 3397–3404 (1972).
11. Nakajima, A., Shinoda, K., *Journal of Colloid and Interface Science* **55**, 126-132 (1976).
12. Shinoda, K., Sakai, K., Hayashi, T., Nakajima, A. , *Polymer Journal* **8**, 208-215 (1976).
13. Schneider, G. F., Decher, G., *Nano Letters* **8**, 3598-3604 (2008).
14. Decher, G., *Science* **277**, 1232-1237 (1997).
15. *Multilayer Thin Films: Sequential Assembly of Nanocomposite Materials.* Decher, G., Schlenoff, J. B., Ed., (Wiley-VCH Verlag GmbH & Co. KGaA, Weinheim, ed. 2, 2012).
16. Tang, Z., Wang, Y., Podsiadlo, P., Kotov, N. A. , *Advanced Materials* **18**, 3203-3224 (2006).
17. El-Khouri, R. J., Szamocki, R., Sergeeva, Y. N., Felix O., Decher G. , in *Functional Polymeric Ultrathin Films*, Advincula, R. K., W., Ed. (Wiley-VCH, Weinheim, 2011), vol. 1.
18. Hammond, P. T., *Materials Today* **15**, 196-206 (2012).
19. Decher, G., Hong, J. D., Schmitt, J., *Thin Solid Films* **211**, 831-835 (1992).
20. Ladam, G., Schaad, P. Voegel, J.-C., Schaaf, P., Decher, G., Cuisinier, F., *Langmuir* **16**, 1249-1255 (2000).
21. Izquierdo, A., Ono, S. S., Voegel, J.-C., Schaaf, P., Decher, G., *Langmuir* **21**, 7558-7567 (2005).
22. Elbert, D. L., Herbert, C. B., Hubbell, J. A., *Langmuir* **15**, 5355-5362 (1999).
23. Picart, C., Lavalle, Ph., Hubert, P., Cuisinier, F. J. G., Decher, G., Schaaf, P., Voegel, J.-C., *Langmuir* **17**, (2001).

24. Picart, C., Mutterer, J., Richert, L., Luo, Y., Prestwich, G. D., Schaaf, P., Voegel, J.-C., Lavalle, P., *Proceedings of the National Academy of Sciences* **99**, 12531-12535 (2002).

25. Lavalle, P., Gergely, C., Cuisinier, F. J. G., Decher, G., Schaaf, P., Voegel, J.-C., Picart , C., *Macromolecules* **35**, 4458-4465 (2002).

26. Richert, L., Arntz, Y., Schaaf, P., Voegel, J.-C., Picart, C., *Surface Science* **2004**, 13-29 (2004).

27. Mendelsohn, J. D., Yang, S. Y., Hiller, J, Hochbaum, A. I., Rubner, M. F., *Biomacromolecules* **4**, 96-106 (2003).

28. Yang, S. Y. Y., Mendelsohn, J. D., Rubner, M. F., *Biomacromolecules* **4**, 987-994 (2003).

29. Richert, L., Boulmedais, F., Lavalle, Ph., Mutterer, J., Ferreux, E., Decher, G., Schaaf, P., Voegel, J.-C., Picart, C. , *Biomacromolecules* **5**, 284-294 (2004).

30. Moussallem, M. D., Olenych, S. G., Scott, S. L., Keller, T. C. S., Schlenoff, J. B. , *Biomacromolecules* **10**, (2009).

31. Boudou, T., Claire, N., Ren, K., Picart, C., *Macromolecular Bioscience* **11**, 77-89.

32. Kirchhof, K., Hristova, K., Krasteva, N., Altankov, G., Groth, T., , *Journal of Materials Science: Materials in Medicine* **20**, 897-907 (2009).

33. Kinnane, C. R., Wark, K., Such, G. K., Johnston, A. P. R., Caruso, F., *Small* **5**, 444-448 (2009).

34. Martinez, J. S., Keller, T. C. S., Schlenoff, J. B., *Biomacromolecules* **12**, 4063-4070 (2011).

35. Lichter, J. A., Van Vliet, K. J., Rubner, M. F., *Macromolecules* **42**, 8573-8586 (2009).

36. Kerdjoudj, H., Boura, C., Moby, V., Montagne, K., Schaaf, P., Voegel, J.-C., Stoltz, J.-F., Menu, P., *Advanced Functional Materials* **17**, 2667-2673 (2007).

37. Davila, J., Chassepot, A., Longo, J., Boulmedais, F., Reisch, A., Frisch, B., Meyer, F., Voegel, J.-C., Mésini, Ph. J., †, Senger, B., Metz-Boutigue, M.-H., Hemmerlé, J., Lavalle, Ph., Schaaf, P., Jierry, L., *Journal of American Chemical Society* **134**, 83-86 (2012).

38. Crystal, R. G., *Science* **270**, 404-410 (1995).

39. Gao, X., Kim, K.-S., Liu, D. , *The AAPS Journal* **9**, Article 9 (2009).

40. Sheridan, C., *Nature Biotechnology* **29**, 121-128 (2011).

41. Kay, M. A., *Nature Reviews Genetics* **12**, 316-328 (2011).

42. Boeckle, S., Wagner, E., *AAPS Journal* **8**, E731-742 (2006).

43. Check, E., *Nature* **420**, 116-118 (2002).

44. Li, S., Huang, L., *Gene Therapy* **7**, 31-34 (2007).

45. Kabanov, A. V., Kabanov, V. A., *Polymer Science* **36**, 157-168 (1994).

46. Kabanov, A. V., Kabanov, V. A. , *Bioconjugate Chemistry* **6**, 7-20 (1995).

47. Tiera, M. J., Winnik, F. M., Fernandes, J. C. , *Current Gene Therapy* **6**, 59-71 (2006).

48. Wong, S. Y., Pelet, J, M., Putnam, D. , *Progress in Polymer Science* **2007**, 799-837 (2007).

49. Mintzer, M. A., Simanek, E. E., *Chemical Reviews* **109**, 259-302 (2009).

50.	Jeong, J. H., Kim, S. W. Park, T. G., *Progress in Polymer Science* **32**, 1239-1274 (2007).

51.	Golan, R., Hsieh, W., Hansma, H. G. , *Biochemistry* **38**, 14069-14076 (1999).

52.	Godbey, W. T., Mokos, A. G., *Journal of Controlled Release* **72**, 115-125 (2001).

53.	Neu, M., Fischer, D., Kissel, T., *The Journal of Gene Medicine* **7**, 992-1009 (2005).

54.	Behr, J. P., *Chimia* **51**, 34-36 (1997).

55.	Parhamifar, L., Larsen, A. K., Hunter, A. K., Andresen, T., Moghimi, S. M., *Soft Matter* **6**, 4001-4009 (2010).

56.	Chollet, P., Favrot, M. C., Hurbin, A., Coll, J.-L., *The Journal of Gene Medicine* **4**, 84-91 (2002).

57.	Zou, S.-M., Erbacher, P., Remy, J.-S., Behr, J.-P., *Gene Therapy* **2000**, 128-134 (2009).

58.	Wightman, L., Kircheis, R., Rössler, V., Carotta, S., Ruzicka, R., Kursa, M., Wagner, W., *Gene Therapy* **3**, 362-372 (2001).

59.	Bausinger, R., von Gersdorff, K., Braeckmans, K., Ogris, M., Wagner, E., Bräuchle, C., Zumbusch, A., *Angewandte Chemie International Edition* **45**, 1568-1572 (2006).

60.	Payne, C. K., Jones, S. A., Chen, C., Zhuang, X., *Traffic* **8**, 389-401 (2007).

61.	Conner, S. D., Schmid, S. L. , *Nature* **422**, 37-44 (2003).

62.	Midoux, P., Breuzard, G., Gomez, J. P., Pichon C., *Current Gene Therapy* **8**, 335-352 (2008).

63.	Luo, D., Saltzman, W. M., *Nature Biotechnology* **18**, 33-37 (2000).

64.	Kircheis, R., Wightman, L., Wagner, E., *Advanced Drug Delivery Reviews* **53**, 341-358 (2001).

65.	Kabanov, A. V., Astafieva, I. V., Chikindas, V. L., Rosenblat, G. F., Kiselev, V. I., Severin, E. S., Kabanov, V. A., *Biopolymers* **31**, 1437–1443 (1991).

66.	Mortimer, I., Tam, P., MacLachlan, I., Graham, R. W., Saravolac, E. G., Joshi, P. B., *Gene Therapy* **6**, 403-411 (1999).

67.	Brunner, S., Sauer, T., Carotta, S., Cotten, M., Saltik, M., Wagner, E., *Gene Therapy* **7**, 401-407 (2000).

68.	Lvov, Y., Decher, G., Sukhorukov, G., *Macromolecules* **26**, 5396-5399 (1993).

69.	Jewell, C. M., Zhang, J., Fredin, N. J., Lynn, D. M., *Journal of Controlled Release* **106**, 214-223 (2005).

70.	Bechler, S. L., Lynn, D. M., *Biomacromolecules* **13**, 542-552 (2012).

71.	Saurer, E. M., Flessner, R. M., Sullivan, S. P., Prausnitz, M. R., Lynn, D. M., *Biomacromolecules* **11**, 3136-3143 (2010).

72.	Aytar, B. S., Prausnitz, M. R., Lynn, D.M.,, *ACS Applied Materials and Interfaces* **4**, 2726-2734 (2012).

73.	Chen, J., Huang, S.-W., Lin, W.-H., Zhuo, R.-X., *Small* **3**, 636-643 (2007).

74.	Blacklock, J., You, Y.Z., Zhou, Q. H., Mao, G., Oupický, D., *Biomaterials* **30**, 939-950 (2009).

75. Blacklock, J., Vetter, A., Lankenau, A., Oupický, D., Möhwald, H., *Biomaterials* **31**, 7164-7174 (2010).

76. Johnson, A., Lewis, J., Raff, M., Roberts, K., Walter, P., Wilson, J., Hunt, T., Molecular Biology of the Cell. Anderson, M., Granum, S., Ed., (Garland science, Taylor & Francis Group, LLC, New York, ed. 5, 2008).

77. Dixon, M. C., *journal of Biomolecular Techniques* **19**, 151-158 (2007).

78. Fredriksson, C., Kihlman, S., Rodahl, M., Kasemo, B., *Langmuir* **14**, 248-251 (1998).

79. Nimeri, G., Fredriksson, C., Elwing, H., Liu, L., Rodahl, M., Kasemo, B., *Colloids and Surfaces B: Biointerfaces* **11**, 255-264 (1998).

80. Lord, M. S., Modin, C., Foss, M., Duch, M., Simmons, A., Pedersen, F. S., Milthorpe, B.K., Besenbacher, F., *Biomaterials* **27**, 4529-4537 (2006).

81. Saravia, V., Toca-Herrera, J. L., *Microscopy Research and Technique* **72**, 957-964 (2009).

82. Chen, J. Y., Li, M., Penn, L. S., Xi, J., *Analytical Chemistry* **83**, 3141-3146 (2011).

83. Fatisson, J., Azari, F., Tufenkji, N., *Biosensors and Bioelectronics* **26**, 3207-3212 (2011).

84. Marx, K. A., Zhou, T., Montrone, A., McIntosh, D., Braunhut, S. J., *Analytical Biochemistry* **361**, 77-92 (2007).

85. Wang, H., Zeng, H., Liu, Z., Yang, Y., Deng, T., Shen, G., Yu, R., *Analytical Chemistry* **76**, 2203-2209 (2004).

86. Zeng, H., Wang, H., Chen, F., Xin, H., Wang, G., Xiao, L., Song, K., Wu, D., He, Q., Shen, G., *Analytical Biochemistry* **351**, 69-76 (2006).

87. Wang, H., Zeng, H., Shen, G., Yu, R., *Analytical Chemistry* **78**, 2571-2578 (2006).

88. Tymchenko, N., Nilebäck, E., Voinova, M. V., Gold, J., Kasemo, B., Svedhem, S., *Biointerphases* **7:43**, (2012).

89. Schärtl, W., Light Scattering from Polymer Solutions and Nanoparticle Dispersions. Pasch, H., Ed., Springer Laboratory Manuals in Polymer Science (Springer, Berlin Heidelberg New York, 2007).

90. http://en.wikipedia.org/.

91. www.malvern.com.

92. Kralchevsky, P. A., Danov, K. D., Denkov N. D., in Handbook of Surface and Colloid Chemistry, Birdi, K. S., Ed. (Taylor & Francis Group, LLC, 2009), pp. 197-377.

93. Charrett, T. O. H., James, S. W., Tatam, R. P., *Measurement Science and Technology* **23**, 032001 (032032pp) (2012).

94. Handbook of Ellipsometry. Tompkins, H. G., Irene, E. A. , Ed., (William Andrew, Inc., Norwich, NY, 2005).

95. Cady, W. G., Piezoelectricity. An introduction to the theory and applications of electromechanical phenomena in crystals. DuBnidge, L. A., Ed., International series in pure and applied physics (McGraw-Hill Book Company, Inc., New York London, ed. 1, 1946).

96. Rodahl, M., Kasemo, B., *Review of Scientific Instruments* **66**, 3238-3241 (1996).

97. Sauerbrey, G., *Zeitschrift fiir Physik* **155**, 206-222 (1959).

98. Kanazawa, K. K., Gordon, J. G. II, *Analytical Chemistry* **57**, 1770-1771 (1985).

99. Rodahl, M., Kasemo, B., *Sensors and Actuators B* **37**, 111-116 (1996).

100. Voinova, M. V., Rodahl, M., Jonson, M., Kasemo, B., *Physica Scripta* **59**, 391-396 (1999).

101. Davies, D., in *Flow cytometry: Principles and Applications*, Macey, M. G., Ed. (Humana Press Inc., Totowa, NJ, 2007).

102. Brown, M., Wittwer, C., *Clinical Chemistry* **46**, 1221-1229 (2000).

103. de Gennes, P. G., *Reviews of Modern Physics* **57**, 827-863 (1985).

104. http://en.wikipedia.org/.

105. Anselme, K., Ploux, L., Ponche, A. , *Journal of Adhesion Science and Technology* **24**, 831-852 (2010).

106. Hudalla, G. A., Murphy, W. L. , *Soft Matter* **7**, 9561-9571 (2011).

107. Mei, Y., Saha, K., Bogatyrev, S. R., Yang, J., Hook, A. L., Kalcioglu, Z. I., Cho, S.-W., Mitalipova, M., Pyzocha, N., Rojas, F., Van Vliet, K. J., Davies, M. C., Alexander, M. R., Langer, R., Jaenisch R., Anderson, D. G., *Nature Materials* **9**, 768-778 (2010).

108. Ponche, A., Ploux L., Anselme, K., *Journal of Adhesion Science and Technology* **24**, 2141-2164 (2010).

109. Suzuki, S., Ikada, Y., *Journal of Adhesion Science and Technology* **24**, 2059-2077 (2010).

110. Boudou, T., Crouzier, T., Ren, K., Blin, G., Picart, C., *Advanced Materials* **22**, 441-467 (2010).

111. Wong, J. E., Rehfeldt, F., Hänni, P., Tanaka, M., Klitzing, R. v., *Macromolecules* **37**, 7285-7289 (2004).

112. Nestler, P., Block , S., Helm, C. A., *Journal of Physical Chemistry B* **116**, 1234-1243 (2012).

113. Guzmán, E., Ritacco, H., Rubio, J. E. F., Rubio, R. G., Ortega, F., *Soft Matter* **5**, 2130-2142 (2009).

114. Richert, L., Lavalle, Ph., Payan, E., Shu, X., Z., Prestwich, G. D., Stoltz, J.-F., Schaaf, P., Voegel, J.-C., Picart, C., *Langmuir* **20**, 448-458 (2004).

115. Abdelkebir, K., Gaudière, F., Morin-Grognet, S., Coquerel, G., Labat, B., Atmani, H., Ladam, G., *Soft Matter* **7**, 9197-9205 (2011).

116. Wong, S. Y., Han, L., Timachova, K., Veselinovic, J., Hyder, M. N., Ortiz, C., Klibanov, A. M., Hammond, P. T. , *Biomacromolecules* **13**, 719-726 (2012).

117. Olenych, S. G., Moussallem, M. D., Salloum, D. S., Schlenoff, J. B., Keller, T. C. S., *Biomacromolecules* **2005**, 3252-3258 (2005).

118. Salloum, D. S., Olenych, S. G., Keller, T. C. S., Schlenoff, J. B., *Biomacromolecules* **6**, 161-167 (2005).

119. Picart, C., Elkaim, R., Richert, L., Audoin, F., Arntz, Y., Cardoso, M. D. S., Schaaf, P., Voegel, J.-C., Frisch, B., *Advanced Functional Materials* **15**, 83-94 (2005).

120. Tryoen-Tóth, P., Vautier, D., Haikel, Y., Voegel, J.-F., Schaaf, P., Chluba, J., Ogier, J., *Journal of Biomedical Materials Research* **60**, 657-667 (2002).

121. Guillaume-Gentil, O., Semenov, O. V., Zisch, A. H.,Zimmermann, R., Voros, J., Ehrbar, M., *Biomaterials* **32**, 4376-4384 (2011).

122. Brunot, C., Grosgogeat, B., Picart, C., Lagneaua, C., Jaffrezic-Renault, N., Ponsonnet, L., Dental Materials **24**, 1025-1035 (2008).
123. Serizawa, T., Yamaguchi, M., Kishida, A., Akashi, M., Journal of Biomedical Materials Research Part A **67A**, 1060-1063 (2003).
124. Richert, L., Lavalle, Ph., Payan, E., Zheng Shu, X., Prestwich, G. D., Stoltz, J.-F., Schaaf, P., Voegel, J.-C., Picart, C. , Langmuir **20**, 448-458 (2004).
125. Croll, T. I., O'Connor, A. J., Stevens, G. W., Cooper-White, J. J. , Biomacromolecules **7**, 1610-1622 (2006).
126. Decher, G., Felix, O., Saulnier, B., Izquierdo, A., Voegel, J.-C., Schaaf, P. G., Jessel, N., Ball, V. P., in Organisation Mondiale de la Propriété Intellectuelle Scientifique, C. N. d. l. R., Ed. (France, 2007).
127. Kidambi, S., Lee, I., Chan, C., Journal of American Chemical Society **126**, 16286-16287 (2004).
128. Young, B. R., Pitt, W. G., Cooper, S. L., Journal of Colloid and Interface Science **125**, 246-260 (1988).
129. Ertel, S. I., Ratner, B. D., Horbett, T. A., Journal of Colloid and Interface Science **147**, 433-442 (1991).
130. Tamada, T., Ikada, Y.,, Journal of Colloid and Interface Science **155**, 334-339 (1993).
131. Haynes, C. A., Norde, W., Colloids and Surfaces B: Biointerfaces **2**, 517-566 (1994).
132. Schwinté, P., Ball, V., Szalontai, B., Haikel, Y., Voegel, J.-C., Schaaf, P., Biomacromolecules **3**, 1135-1143 (2002).
133. Szyk, L., Schaaf, P., Gergely, C., Voegel, J.-C., Tinland, B., Langmuir **17**, 6248-6253 (2001).
134. Salloum, D. S., Schlenoff, J. B., Biomacromolecules **5**, 1089-1096 (2004).
135. Huetz, P., Ball, V., Voegel, J.-C., Schaaf, P., Langmuir **11**, 3145-3152 (1995).
136. Ball, V., Bentaleb, A., Hemmerle, J., Voegel, J.-C., Schaaf, P., Langmuir **12**, 1614-1621 (1996).
137. http://www.invitrogen.com.
138. Ladam, G., Gergely, C., Senger, B., Decher, G., Voegel, J.-C., Schaaf, P., Cuisinier, F. J. G., Biomacromolecules **1**, 674-687 (2000).
139. Channasanon, S., Graisuwan, W., Kiatkamjornwong, S., Hoven, V. P., Journal of Colloid and Interface Science **316**, 331-343 (2007).
140. Serizawa, T., Yamaguchi, M., Akashi, M., Biomacromolecules **3**, 724-731 (2002).
141. Müller, M., Torger, B., Keßler, B., Advanced Engineering materials **12**, B676-B683 (2010).
142. Roach, P., Farrar, D., Perry, C. C., Journal of American Chemical Society **127**, 8168-8173 (2005).
143. Faucheux, N., Schweiss, R., Lützow, K., Werner, C., Groth, T., Biomaterials **25**, 2721-2730 (2004).
144. Tristán, F., Palestino, G., Menchaca, J. L., Pérez, E., Atmani, H., Cuisinier, F., Ladam, G., Biomacromolecules **10**, 2275-2283 (2009).

145. Schmitt, J., Gruenewald, T., Decher, G., Pershan, P. S., Kjaer, K., Loesche, M., Macromolecules **26**, 7058-7063 (1993).

146. Choksakulnimitr, S., Masuda, S., Tokuda, H., Takakura, Y., Hashida, M., Journal of Controlled Release **34**, 233-241 (1995).

147. Fischer, D., Lib, Y., Ahlemeyer, B., Krieglstein, J., Kissel, T., Biomaterials **24**, 1121-1131 (2003).

148. Chanana, M., Gliozzi, A., Diaspro, A., Chodnevskaja, I., Huewel, S., Moskalenko, V., Ulrichs, K., Galla, H.-J., Krol, S., Nano Letters **5**, 2605-2612 (2005).

149. Grieshaber, D., Vörös, J., Zambelli, T., Ball, V., Schaaf, P., Voegel, J-C., Boulmedais, F. , Langmuir **24**, 13668-13676 (2008).

150. Liu, G., Zhao, J., Sun, Q., Zhang, G., Journal of Physical Chemistry B **112**, 3333-3338 (2008).

151. Yang, A. Y., Rawle, R. J., Selassie, C. R. D., Johal, M. S., Biomacromolecules **9**, 3416-3421 (2008).

152. Papadakis, G., Tsortos, G., Bender, F., Ferapontova, E., Gizeli, E., Analytical Chemistry **84**, 1854-1861 (2012).

153. Amsden, B., Turner, N., Biotechnology and Bioengineering **65**, 605-610 (1999).

154. Lord, M., Foss, M., Besenbacher, F., Nano Today **5**, 66-78 (2010).

155. Adler, A. F., Speidel, A. T., Christoforou, N., Kolind, K.,, Foss, M., Leong, K. W., Biomaterials **32**, 3611-3619 (2011).

156. Witt, M. A., Valenga,F., Blell, R., Dotto, M. E. R., Bechtold, I. H., Felix, O., Pires, A. T. N., Decher, G., Biointerphases **7**, 64-73 (2012).

157. Stenger, D. A. P., C. J., Hickmanc, J. J. Cotman, C. W., Brain Research **630**, 136-147 (1993).

158. Gioia, S. D., Conese, M., Drug Design, Development and Therapy **2**, 163-188 (2008).

159. Boussif, O., Lezoualc'h, F., Zanta, M. A., Mergny, M. D., Scherman, D., Demeneix, B., Behr, J.-P, Proceedings of the National Academy of Sciences **92**, 7297-7301 (1995).

160. Pollard, H., Remy, J.-S., Loussouarn, G., Demolombe, S., Behr, J.-P., Escande, D., The Journal of Biological Chemistry **273**, 7507-7511 (1998).

161. Kircheis, R., Wightman, L., Schreiber, Robitza, B., Rössler, V., Kursa, M., Wagner, E., Gene Therapy **8**, 28-40 (2001).

162. Colman, A., Cell Stem Cell **3**, 236-237 (2008).

163. Takahashi, K., Yamanaka, S., Cell **126**, 663-676 (2006).

164. Blelloch, R., Venere, M., Yen, J., Ramalho-Santos, M., Cell Stem Cell **1**, 245-247 (2007).

165. Hanna, J. H., Saha, K., Jaenisch, R., Cell **143**, 508-525 (2010).

166. http://www.polyplus-transfection.com/.

167. Cherstvy, A. G., Journal of Physical Chemistry B **112**, 12585-12595 (2008).

168. Lyubchenko, Y. L., Cell Biochemistry and Biophysics **41**, 75-97 (2004).

169. Wynveen, A., Lee, D. J., Kornyshev, A. A., Leikin, S., Nucleic Acids Research **36**, 5540-5551 (2008).

170. Baldwin, G. S., Brooks, N. J., Robson, R. G., Wynveen, A., Goldar, A., Leikin, S., Seddon, J. M., Kornyshev, A. A. , *Journal of Physical Chemistry B* **112**, 1060-1064 (2008).

171. Goodman, A., Tseng, Y., Wirtz, D. , *Journal of Molecular Biology* **323**, 199-215 (2002).

172. Inoue, S., Sugiyama, S., Travers, A. A., Ohyama, T., *Biochemistry* **46**, 164-171 (2007).

173. Stewart, M. P., Helenius, J., Toyoda, Y., Ramanathan, S. P., Muller, D. J., Hyman, A. A., *Nature* **469**, 226-230 (2011).

174. Théry, M., Bornens, M., *Current Opinion in Cell Biology* **18**, 648-657 (2006).

175. Clamme, J.-P., Krishnamoorthy, G., Mély, Y., *Biochimica et Biophysica Acta* **1617**, 52-61 (2003).

176. Rémy-Kristensen, A., Clamme, J.-P., Vuilleumier, C., Kuhry, J.-G., Mély, Y., *Biochimica et Biophysica Acta* **1514**, 21-32 (2001).

177. Ruthardt, N., Bräuchle, C., *Topics in Current Chemistry* **296**, 283-304 (2010).

178. Suh, J., An, Y., Tang, B., Dempsey, C., Huang, F., Hanes, J., *Microscopy Research and Technique* **75**, 691-697 (2012).

179. Cans, A.-S., Höök, F., Shupliakov, O., Ewing, A. G., Eriksson, P. S., Brodin, L., Orwar, O., *Analytical Chemistry* **73**, 5805-5811 (2001).